Experimental Studies of Exotic Transitions in High-Z Few-Electron Ions

Dissertation
zur Erlangung des Doktorgrades
der Naturwissenschaften

vorgelegt beim Fachbereich Physik
der Johann Wolfgang Goethe-Universität
in Frankfurt am Main

von
Sergiy Trotsenko
aus Bogodukhiv

Frankfurt am Main 2008
(D30)

vom Fachbereich Physik der Johann Wolfgang Goethe-Universität
als Dissertation angenommen.

Dekan:	Prof. Dr. D.-H. Rischke
Gutachter:	Prof. Dr. Th. Stöhlker
	Prof. Dr. R. Dörner
Datum der Disputation:	24.06.2009

Contents

1 Introduction **13**

2 The Structure of Few-electron systems **17**

2.1 One-electron ions 17

2.2 Two-electron ions 20

2.3 Transition rates 24

2.3.1 Transition rates for H-like ions 25

2.3.2 Transition rates for He-like ions 25

3 Two-photon transitions **29**

3.1 The simultaneous emission of two photons 29

3.2 Two-photon decay in one-electron ions 32

3.3 Two-photon decay in two-electron ions 34

3.4 Dependence of the two-photon decay properties on the atomic number Z 36

3.5 The $2E1$ decay rate and energy distribution 38

3.6 Two-photon decay of ions with inner-shell vacancy 41

3.7 Earlier Two-Photon Decay Experiments 42

4 Experimental Approach for Studying Exotic Transitions **47**

4.1 Collisions of Highly Charged Ions. 47

4.2 Ionization and Excitation Processes 48

4.3 Selective Generation of Excited States in Few-Electron Ions 50

4.3.1 Ionization and excitation probabilities 52

4.3.2 Simultaneous excitation and ionization in the IPA framework . . . 53
4.3.3 Relaxation of Electron Orbitals . . . 54

5 Experimental Facility 57
5.1 The GSI Accelerator Facility . . . 58
5.2 Experimental Storage Ring . . . 59
5.3 The Gas-jet target at the ESR . . . 62
5.4 X-ray Detectors . . . 63
5.5 Experiments at the ESR . . . 66

6 Feasibility of the Exclusive Production of the K-shell vacancy 69
6.1 Selective ionization of the K-shell electron of Li-like Uranium . . 69
6.2 Selective ionization of the K-shell electron of Be-like Uranium . . 74

7 Measurement of the two-photon decay in He-like tin and the data evaluation 77
7.1 The Experiment . . . 77
7.2 Total x-ray spectrum . . . 80
7.3 Random subtraction . . . 81
7.4 Ionization spectrum . . . 82
7.5 Energy and Efficiency calibration . . . 86
7.6 Spectra simulations . . . 88
7.6.1 Relativistic Doppler shift . . . 89
7.6.2 Doppler broadening of the x-ray lines . . . 90
7.6.3 Detector Response . . . 90

8 Results and Discussions 93

9 Summary 99

10 Outlook 101
10.1 Further Applications: Two-Electron One-Photon transition in Li-like Uranium . . . 102

10.2 Two-Photon Decay in High-Z ions:
Further Development and New Challenges 103

11 Zusammenfassung 107

References 113

List of Figures

1.1 Level scheme of the first excited levels of a He-like ion. 14

2.1 The mean value of the electric field strength $< |E| >$ as a function of nuclear charge (Z) for the most strongly bound states in H-like ions. 18

2.2 The level scheme according to the Dirac's theory for the lowest atomic levels in one-electron ions. The dashed lines represent the QED corrections to the energy levels. 19

2.3 Level scheme for a) a light(LS-coupling) and b) a heavy (jj-coupling) He-like ion. Besides the decay mode of every ground state transition, the respective Z-scaling of the transition rates are also presented. 21

2.4 The different contributions to the absolute ionization potential in He-like systems [7]. The data refer to the $1s^2\ {}^1S_0$ ground state. The corrections that lead to a reduction of the ionization potential are marked with a minus sign. 23

2.5 The absolute decay rates and lifetimes of the L → K transitions in He-like ions as a function of the nuclear charge (for an explanation of $2E1$-shape see the next chapter). 25

2.6 Branching ratio for the radiative decay of the $1s2p\ {}^3P_2$-level to the $1s2p\ {}^3S_1$-state as a function of nuclear charge for He-like ions [17]. 26

3.1 Schematic of forbidden and allowed transitions with respect to the angular momentum conservation law. 29

3.2 Calculated typical energy distribution of the two-photon decay of the $2\ {}^1S_0$-state of a He-like ion. The intensity is normalized to the middle of the distribution. The photon energy is normalized to the energy difference (E_0) between the initial and the final state (see equation 3.1). 30

3.3 Calculated theoretical angular distribution of two-photon emission from $ns - 1s$ transition ($1 + \cos^2\theta$); θ is the angle between the two photons [79], [130], [59], [131]. 31

3.4 Level scheme of the first excited states of hydrogen. The scaling of the corresponding transition rates with the atomic number Z is also given. 33

3.5 Level scheme of the first excited states of a He-like ion. The scaling of the corresponding transition rates with the atomic number (Z) is also shown. . . 35

3.6 Theoretical energy distributions of the two-photon ($2E1$) decays in hydrogen and helium [63]. 37

3.7 (Top panel) Comparison of relativistic and non-relativistic estimations of the decay rates for the $2\ ^1S_0$ state [61]. (Lower panel) Full width at half maximum (FWHM) of the two-photon energy distribution of the $2\ ^1S_0$ state ploted as a function of Z [62]. 39

3.8 Energy distribution of the $2\ ^1S_0$ - $1\ ^1S_0$ two-photon transition, calculated using a relativistic approach [63]. 41

4.1 Impact parameter (b) in collision of ion (projectile) with atom (target). . . . 49

4.2 Production of the excited $1s2s$ state by selective K-shell ionization. One K-shell electron is ionized without disturbing the remaining two electrons. . . . 50

4.3 Impact parameter dependent description of the ionization/excitation processes. 52

4.4 The $1s_{1/2}$ ionization and/or $2s_{1/2}$ excitation probabilities for relativistic 398 MeV/u $U^{89+} \rightarrow N_2$ collisions as a function of the impact parameter b(λ); with λ - Compton wavelength [104], [105]. 54

5.1 Layout of the accelerator facility at GSI, showing the linear accelerator UNILAC, the heavy-ion synchrotron SIS18, and the experimental storage ring ESR. 57

5.2 Calculated charge-state evolution as a function of target thickness for 300 MeV/u uranium ions impinging on Cu (top panel), Al (middle panel) and C (bottom panel) targets. Colors of the lines define different charge-states (black lines for bare ions, red - H-like, green - He-like, blue - Li-like etc.) 58

5.3 Schematic of the storage and cooler ring ESR at GSI. The layout depicts the beam guiding system (dipole bending magnets, quadrupoles and hexapoles) as well as the most important installations for beam handling and diagnostics (kicker, rf cavities, Schottky noise pick-up, electron cooler). The position of the internal jet-target is marked in addition. 60

5.4 Layout of the electron cooler device used at the storage and cooler ring ESR. Electrons produced in the electron gun at a cathode temperature of $\approx$ 1300 K are guided by a $\approx$0.1 T magnetic field co-propagating over a distance of 2 m with the stored ion beam [93]. 61

5.5 Schottky frequency spectra for a circulating beam of U^{92+} ions at 295MeV/u. The broad distribution refers to the uncooled initial beam, measured directly after injection into the ESR. The narrow distribution reflects the momentum profile of a continuously cooled ion beam. 61

5.6 Scheme of the Gas Jet target at the ESR[100]. 62

5.7 The high-purity germanium x-ray detector (ORTEC) used in the experiment. 65

5.8 Principle of charge-exchange experiments at the internal gas jet target of the ESR, illustrated for the case of stored q^+ ions. The primary beam of stored ions (with charge-state Q) crosses a perpendicularly oriented molecular or atomic supersonic gas jet. The dipole magnet serves as a magnetic spectrometer. Also shown are the particle detectors for electron capture, i.e. $q^+ \rightarrow (q-1)^+$, and for ionization, i.e. $q^+ \rightarrow (q+1)^+$. 67

6.1 Projectile x-ray spectra for 98 MeV/u $U^{89+} \rightarrow N_2$ collisions measured (a) without coincidence requirement (total emission spectrum), (b) with excitation coincidence (U^{89+} charge), (c) with capture coincidence (U^{88+} charge), (d) with ionization coincidence (U^{90+} charge). All spectra were recorded at an observation angle of θ=35^o. Energies correspond to the laboratory frame. 71

6.2 Projectile x-ray spectra for 398 MeV/u $U^{89+} \rightarrow N_2$ collisions measured (a) without coincidence requirement (total emission spectrum), (b) with excitation coincidence (U^{89+} charge), (c) with capture coincidence (U^{88+} charge), (d) with ionization coincidence (U^{90+} charge). All spectra were recorded at an observation angle of θ=35^o. Energies correspond to the laboratory frame. 72

6.3 Schematic of two-electron one-photon transition ($1s2s^2 \rightarrow 1s2s2p_{1/2}$). 74

6.4 Projectile x-ray spectra for 90 MeV/u $U^{88+} \rightarrow N_2$ collisions measured (a) without coincidence requirement (total emission spectrum), (b) with excitation coincidence (U^{88+} charge), (c) with ionization coincidence (U^{89+} charge). All spectra were recorded at an observation angle of θ=35^o. 75

7.1 Energy level scheme for He-like tin. The vertical axis represents the binding energy, the numbers above the levels correspond to the lifetimes. 78

7.2 X-ray detectors at the gas-jet target of the ESR. The 35° detector is the one on the far right. 79

7.3 Total (raw) x-ray spectrum from 300 MeV/u $Sn^{47+} \rightarrow N_2$ collisions, measured at an angle of 35°. 80

7.4 Time spectrum, showing the 'prompt' and 'random' intervals. The time is obtained from the difference between the registered x-ray and particle events. 81

7.5 X-ray spectra of 300 MeV/u $Sn^{47+} \rightarrow N_2$ collisions measured at an angle of 35°, (a) without coincidence (total x-ray spectrum), (b) in coincidence with ionization including random events, (c) in anti-coincidence - random and (d) in coincidence with ionization without random events (Sn^{48+}). 83

7.6 Zoom of the energy region around the K_α and $M1$ peaks. The top panel clearly shows the two peaks, which energies are labelled both for the laboratory and the emitter frame. The bottom panel shows the pure $M1$ peak, obtained by proper timing conditions. 84

7.7 The K_β peaks with different time conditions. The x-ray energies given apply to the laboratory frame. The top panel shows the total spectrum, the lower panel the spectrum with timing conditions (ionization). 85

7.8 The x-ray spectrum from the ^{241}Am-source, as it was taken for the energy and efficiency calibration of the detector. The energy scale is given in channels, and the intensity is normalized to the amplitude of the X_1 peak (59,54 keV). The colors of the spectra denote measurements performed with a thick (red) and a thin (blue) source. 86

7.9 Relative efficiency of the germanium detector (13 mm thick), as provided by the supplier. The energy range of importance for the two-photon spectral shape measurements is marked (20-40 keV). 87

7.10 Measured relative efficiency of the germanium detector (13 mm thick). The red (hollow) and blue (full) circles denote the measurements with and without slit, correspondingly. The energy range of importance for the two-photon spectral shape measurements is marked. 88

7.11 The detector response function for the $M1$ transition. 92

8.1 Top part: Higher energy half of the fully relativistic calculated two-photon energy distribution (the intensity is normalized to 1 at f =0.5) for He-like Ni (dash-doted line), Sn (solid line) and U (dashed line). Vertical dashed lines show the different regions of the spectral shape. Bottom part: Comparison between the higher energy half of the measured two-photon spectral distribution of He-like tin (solid light-gray line), and a fully relativistic calculation for He-like Sn (solid line) and U (dashed line) together with the simulated detector response function for the $M1$ line (dotted line). 94

8.2 (Exp-Theory)/Theory intensity ratio with theoretical values for Ar, Sn, Yb and U as a function of the photon energy fraction. Each point corresponds to bin of 1000 eV energy region. Data has been plotted up to f =0.92, where the low-energy tail of the $M1$ peak does not contribute. Horizontal dotted lines are the mean value and ± 3σ value in case of Sn. 96

10.1 Rates for the various decay modes of the $1s2s^2\ 2S_{1/2}$ state plotted as a function of the atomic number Z [141]. 103

10.2 Photon-photon angular correlations in the $2^1S_0 \rightarrow 1^1S_0$ two-photon decay of the He-like uranium ion. Results are presented for the relativistic and the non-relativistic calculations for the equal share of the photon energy($f = 0.5$) [63]. 104

List of Tables

2.1 The absolute transition rates [17] and energies [7] for the decay modes of $1s2p^3P_2$- and $1s2p^3P_0$-states in He-like uranium (U^{90+}). 26

3.1 Decay rates and transition energies of the lowest excited states for the two extreme cases of one-electron systems [42]. *The sum energy of two simultaneously emitted photons. 33

5.1 The parameters of the high-purity germanium x-ray detector (ORTEC) used in the experiment. 64

7.1 Decay modes, ground state transition energies, and rates for the $n = 2$ states of He-like tin (Sn^{48+}) ions [119, 62, 120, 61]. The numbers in brackets denote the power of 10. 78

7.2 The radiative lines of the ^{241}Am-source used for the energy calibration of the detector. 87

7.3 Input data for the EGS4 simulation of the detector response, and for the *spec*-code for a calculation of the Doppler broadening of the line. 91

8.1 Intensity ratio R=”I3/I1” (bottom part of Fig. 8.1) for the observed $2E1$ spectral distribution of He-like Sn^{48+} ions, compared with theoretical values for different ions along the helium isoelectronic sequence (^{1}with electron-electron correlations included; ^{2}without electron-electron correlations). 95

Chapter 1

Introduction

Important advantages of laboratory experiments is that a very tight control of systematic effects is possible and that one can repeat the experiment under improved conditions. In general, to improve the accuracy of high-precision spectroscopy experiments, very detailed study of systematic effects is required. Thus one usually aims to minimize perturbing influences on the measurement by both experimental and theoretical means.

In this thesis, an experimental contribution is presented to the high-precision two-photon spectroscopy in the highly charged high-Z ions.

Highly charged ions are specific atomic systems where relativistic and quantum electrodynamic (QED) corrections are essential. In these systems the strong Coulomb field enhances rapidly the importance of the inner shell effects, and increases the probability for transitions that are forbidden in light neutral atoms. Furthermore, the decay rate of allowed $E1$ transitions scales approximately with $Z^1 - Z^4$, while various forbidden transitions such as $M1$, $2E1$ scale with $Z^6 - Z^{10}$, they become especially important in highly charged high-Z ions (see figure 1.1).

The two-photon decay is one of the second-order transitions which involves relativistic, quantum electrodynamic, and (in few-electron systems) correlation effects. In this process, two photons are emitted simultaneously (see figure 3.1). The sum energy of the two emitted photons equals the total transition energy between two involved states. The energies of the individual photons form a continuous distribution. The two-photon transitions are especially strong between those levels, where a single photon decay is strictly forbidden by the conserva-

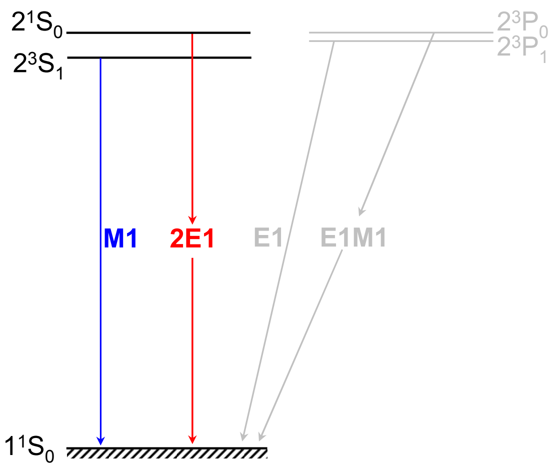

Figure 1.1: Level scheme of the first excited levels of a He-like ion.

tion of angular momentum, e.g. from J=0 to J=0. Existence of the two-photon decays was first suggested by M. Göppert-Mayer in 1930 [18].

Since then, a lot of experimental studies of two-photon transitions in H-like and He-like ions have been performed. Most studies were based on the measurements of the lifetimes of the states emitting the two photons, namely $2s_{1/2}$ state in H-like and 2^1S_0, 2^3S_1 and 2^3P_0 in He-like atoms (see figure 1.1). In He-like systems the first measurements of lifetimes were performed by van Dyck *et al.* [22] and by Prior and Shugart [23] for He and Li^+ ions respectively and by Marrus and Schmieder [24] for Ar^{16+} ions. During the next years, the measurements of the lifetimes of the $2S$ levels in He-like ions were performed for Ni^{26+} and Br^{33+} ions by Dunford *et al.* [25, 26, 27, 28], for Kr^{34+} and Xe^{52+} ions by Marrus *et al.* [29, 30] and for Nb^{39+} ions by Simonovici *et al.* [31]. A measurement of the lifetime of the metastable 2^3P_0 state in He-like gold was carried out by Toleikis *et al.* [32].

In spite of the high precision, all these lifetime experiments can only test the $2E1$ decay probability summed over all continuum photon energies, and the measurements become very difficult for the high-Z systems in which the lifetimes of the levels are very short. More detailed information about the influence of the relativistic corrections on the two-photon transition is provided by measurements of the spectral distribution of the emitted photons. The first measurement has been performed by Mokler *et al.* [33] for the two-photon decay of the $1s2s\ ^1S_0$

in He-like Ge^{30+} ions, and subsequently in Kr^{34+} by Stöhlker *et al.* [34] and by Ali *et al.* [35], in Ni^{26+} ions by Schäffer *et al.* [36] and Dunford *et al.* [37] and in Au^{77+} by Schäffer *et al.* [38]. These experiments (for a review see: [39]) have proven that investigations of the two-photon energy distribution could be an outstanding source of the information about atomic processes and interactions. It has also been shown that for testing of the relativistic corrections, it is important to perform measurements of high-Z ions, where these corrections are large. However, due to a number of experimental difficulties in the high-Z regime, it was hardly possible or even impossible to test relativistic effects with the experimental precision achieved.

In this thesis an alternative experimental technique for the investigation of exotic decay modes (such as two-photon decay, two-electron one-photon transitions) in high-Z highly charged few-electron ions is developed. In this approach a K-shell vacancy is being created selectively, thus providing outstanding background-free conditions for the studying of the transition following the decay of the K-shell hole.

The thesis is structured as follows: In the chapter 2 a short introduction in the structure of a few-electron systems will be given. Main attention will be given to the one- and two-electron ions. The scaling of radiative rates for the most probable transitions will be discussed in detail. Further, the theoretical bases of the two-photon decay will be presented in the chapter 3.1. The phenomenon of the simultaneous emission of two photons will be described and the dependence of the properties of this decay mode will be given with respect to the atomic number for one- as well as for two-electron ions. In the chapter 3.7 the overview to earlier performed experiments on measuring the shape of the two-photon decay will be given. In the chapter 4 a novel experimental approach for studying of exotic transitions (two-photon decay, two-electron one-photon transition, etc.) is presented. The experimental apparatus and experiments proving a feasibility of the developed approach is presented in the chapters 5 and 6 respectively. Measurement of the two-photon decay in He-like tin is presented in the chapter 7 with further description of the data evaluation and results which are given in the chapter 8. Finally, a summary of the obtained results and an outlook will be given in the last two chapters (9,10).

Chapter 2

The Structure of Few-electron systems

Nowadays our knowledge about the atomic structure of the hydrogen and helium atom is extremely precise [2, 3] and the expansion of research along the one- and two-electron isoelectronic sequences up to the heaviest ions is a central subject of atomic physics. With increasing atomic number, Z, the bound electrons experience ever stronger electric fields, and relativistic and QED corrections start to become essential. Figure 2.1 shows the mean value of the electric field strength $\langle|\mathrm{E}|\rangle$ experienced by an electron [4] in a H-like system, for the lowest lying states, as a function of the atomic number Z. The increase of $\langle|\mathrm{E}|\rangle$ by more than six orders of magnitude (as the atomic number increases from Z=1 to Z=92) clearly shows that in the heaviest systems extremely strong electric fields define those effects which affect the atomic structure and can therefore be studied only in heavy ions.

2.1 One-electron ions

The dependence of the electronic binding energies E_B on the atomic number Z and the principal quantum number n was already in 1913 roughly described by Bohr in his postulated model of atom. The energy lines of the hydrogen spectrum

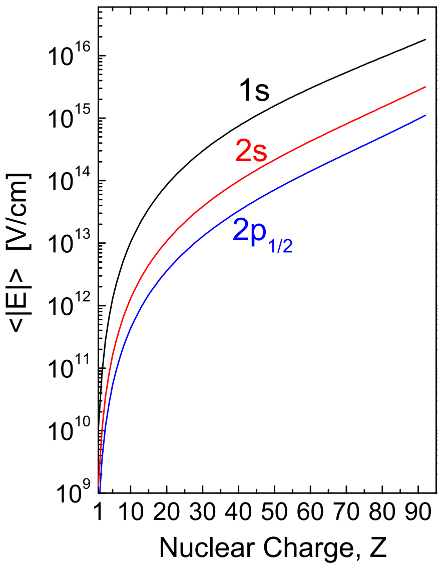

Figure 2.1: The mean value of the electric field strength $< |E| >$ as a function of nuclear charge (Z) for the most strongly bound states in H-like ions.

can already be calculated with Rydberg's formula

$$E_B = -Ry \cdot Z^2/n^2 \tag{2.1}$$

where Ry is the Rydberg constant, which is estimated to be 13.6 eV. This formula correctly describes the n-scaling of the binding energy. However, already in 1885, Balmer observed this dependence described by the *Balmer formula*

$$E = Ry \cdot (1/n^2 - 1/m^2), \tag{2.2}$$

where n, m are the principal quantum numbers with $n < m$, was derived empirically from the four lines (in visible range) of the hydrogen spectrum. The spectroscopic notation for these series are usually referred as: $n = 1$: Lyman series, $n = 2$: Balmer series, $n = 3$: Paschen series. Nevertheless, the atomic model of Bohr was only in rough agreement with the spectroscopic data and gave in particular no explanation for the already observed fine structure splitting of the spectral lines. In turn, *classical* quantum mechanics was able to describe these details of the atomic structure. In order to do that, it was necessary to ascribe a certain angular momentum to the electron. This property of the electron, called

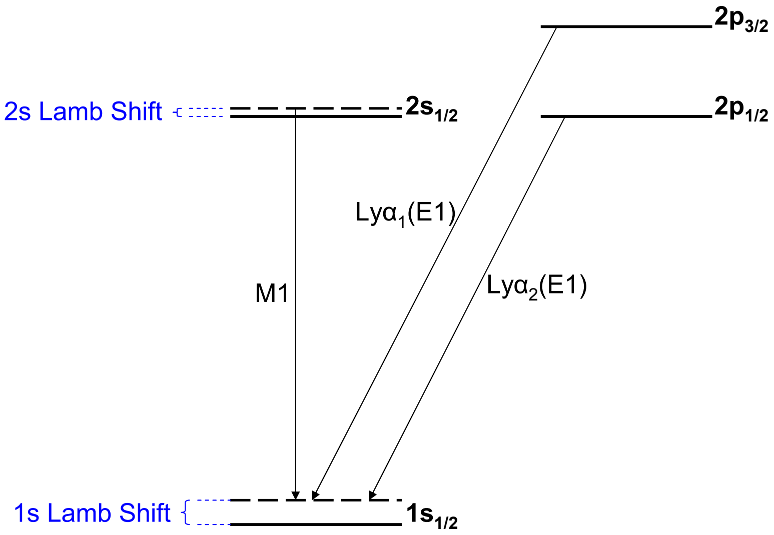

Figure 2.2: The level scheme according to the Dirac's theory for the lowest atomic levels in one-electron ions. The dashed lines represent the QED corrections to the energy levels.

the spin ($s = \frac{1}{2}\hbar$), has no classical analogue. The spin of the electron automatically follows from relativistic quantum mechanics, also known as Dirac theory (1928). Considering the time-independent Dirac equation, the energy eigen-value E_{nj} of a state in an one-electron system, with an infinitely heavy point-like nucleus, is given by an

$$E_{nj} = mc^2 / \sqrt{1 + \left\{ \frac{Z\alpha}{n - |j + 1/2| + \sqrt{(j + 1/2)^2 - (Z\alpha)^2}} \right\}^2}, \tag{2.3}$$

with m - the rest mass of the electron, c - the speed of light in vacuum and α - the fine structure constant. The orbital angular momentum with its quantum number l couples with the spin of the electron to the total angular momentum with the quantum number $j = l \pm 1/2$. Following Dirac theory states with the same n, j are degenerate and their binding energies are given by

$$E_B = E_{nj} - mc^2. \tag{2.4}$$

The level scheme (according to Dirac theory) for the lowest states in H-like ions is shown in figure 2.1, with the ground state $1s_{1/2}$ and the excited states $2s_{1/2}$, $2p_{1/2}$, $2p_{3/2}$. Lyman-α_1 (Lyα_1) and Lyman-α_2 (Lyα_2) are the $2p_{3/2} \rightarrow 1s_{1/2}$ and the $2p_{1/2} \rightarrow 1s_{1/2}$ transitions, respectively. These are electric dipole transitions ($E1$). The $2s_{1/2}$ state only decays via a magnetic dipole transition ($M1$), which plays no role for light atoms, such as atomic hydrogen. However, for the heaviest systems, e.g. H-like uranium, it is of great relevance.

2.2 Two-electron ions

In many-electron atomic systems, the electrons not only interact with the nucleus, but also with each other. Even though very accurate descriptions of the atomic structure for H-like ions can be obtained (except for the Lamb shift corrections), already for few-electron systems (He-like ions) an analytical solution is missing. The energy eigen-values can be obtained by solving the non-relativistic Schrödinger equation:

$$H\Psi = E\Psi \tag{2.5}$$

where Ψ is the two-electron wave function, and H the Hamilton operator which can be expressed as:

$$H = h_s(1) + h_s(2) - \frac{Ze}{r_1} - \frac{Ze}{r_2} + \frac{e}{|r_1 - r_2|} \tag{2.6}$$

with r_1 and r_2 are the coordinates of the two electrons. The terms $h_s(1)$ and $h_s(2)$ are the separate Hamilton operators for free and uncorrelated electrons correspondingly. The $-\frac{Ze}{r_1}$ and $-\frac{Ze}{r_2}$ represent the attraction of the nucleus (with its atomic number Z) for electrons 1 and 2 respectively. The term $\frac{e}{|r_1-r_2|}$ expresses the electron-electron interaction. For approximate solutions of the Schrödinger equation different methods are applied, where for the very light ions a very high precision was achieved. For heavier systems ($Z > 8$) perturbation theory approaches are often used, where the Coulomb repulsion between the electrons is treated as a perturbation of the attractive Coulomb potential between the electron and the nucleus. In the non-relativistic regime the Coulomb repulsion between the electrons determines the energy levels of He-like ions, i.e. as long as the spin-orbit interaction is small compared to the orbit-orbit- and the spin-spin interactions. Since the strength of the Coulomb interaction between the electrons scales with Z, whereas the relativistic effects of the spin-orbit coupling scale with Z^4, the energy levels in heavy He-like ions are determined in terms of jj-coupling.

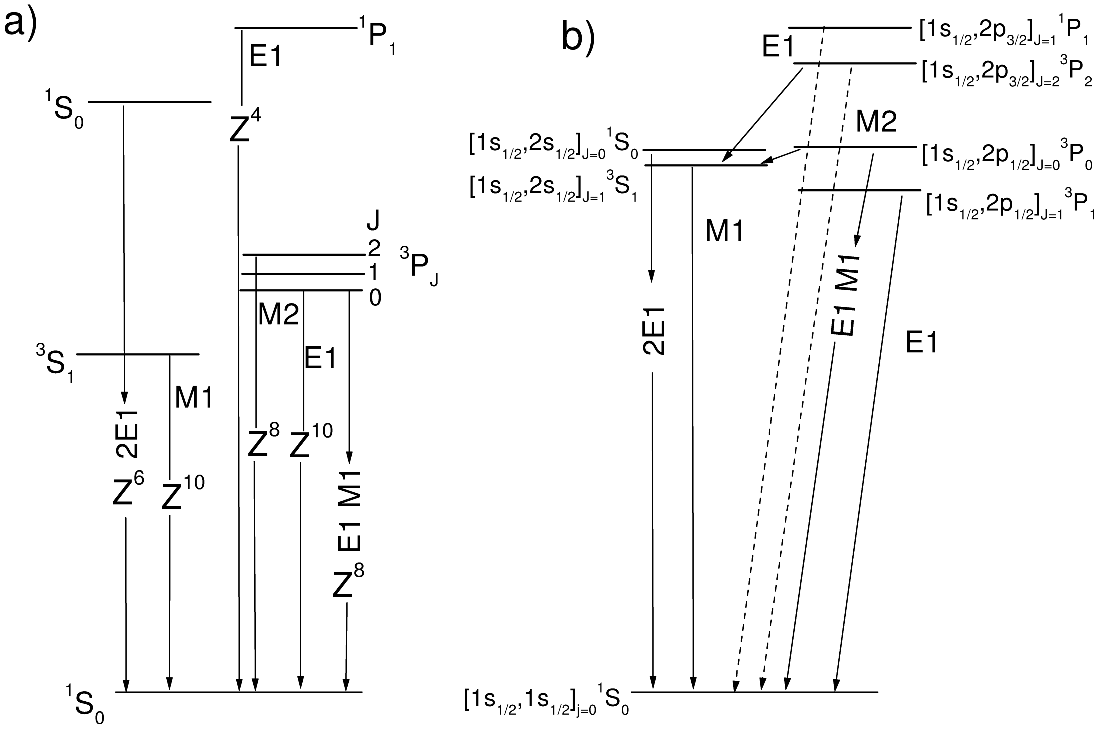
a)
$^1P_1$
E1
$^1S_0$
Z^4
J
2
1
0
^3P_J
M2
E1
$^3S_1$
M1
2E1
Z^6
Z^{10}
Z^8
Z^{10}
E1 M1
Z^8
$^1S_0$
b)
E1
$[1s_{1/2},2p_{3/2}]_{J=1}\,^1P_1$
$[1s_{1/2},2p_{3/2}]_{J=2}\,^3P_2$
M2
$[1s_{1/2},2s_{1/2}]_{J=0}\,^1S_0$
$[1s_{1/2},2s_{1/2}]_{J=1}\,^3S_1$
$[1s_{1/2},2p_{1/2}]_{J=0}\,^3P_0$
$[1s_{1/2},2p_{1/2}]_{J=1}\,^3P_1$
M1
2E1
E1 M1
E1
$[1s_{1/2},1s_{1/2}]_{j=0}\,^1S_0$

Figure 2.3: Level scheme for a) a light(*LS*-coupling) and b) a heavy (*jj*-coupling) He-like ion. Besides the decay mode of every ground state transition, the respective Z-scaling of the transition rates are also presented.

Finally, for very heavy ions the level structure follows nearly the structure of H-like systems. In the figure 2.3 the level structures for two extreme cases of LS- and jj-coupling are shown for the cases of helium and He-like uranium respectively. Besides the multipolarity of every transition, also the Z-scaling of the transition rates are given.

In the helium atom the electron-electron interaction is defined via Coulomb repulsion. However, as was already known from classical electrodynamics, current-current interaction comes into play between moving charges, which is called in atomic physics the *Breit interaction.* The Breit interaction, b_{12}, is very weak for light ions, although formally the terms of the Coulomb and Breit interactions are equivalent (they are both integral components of the electron-electron interaction). For heavy ions it is necessary to take into consideration this dynamical aspect of the electron-electron interaction, g_{12}, in a relativistic description (see e.g. [5]), with

$$g_{12} = \frac{e}{|r_1 - r_2|} + b_{12} \tag{2.7}$$

and

$$b_{12} = -\frac{\alpha_1 \cdot \alpha_2}{r_{12}} + (\alpha_1 \cdot \nabla_1)(\alpha_2 \cdot \nabla_2)\frac{\cos(\omega r_{12} - 1)}{\omega^2 r_{12}} \tag{2.8}$$

Here α_1 and α_2 are the Dirac matrices of both electrons and ω is the momentum of the exchanged photon. The first term is also called the Gaunt interaction [6], and describes the current-current interaction caused by the electrons movement. It contributes about 90% to the Breit interaction. The remaining 10% is due to the second term, which is the retardation of the interaction. In figure 2.4, a comparison of the non-relativistic and relativistic contributions to the ionization potential for the $1s^2\ ^1S_0$ ground state is shown. The absolute binding energies can be obtained by addition of the ground state binding energy of the H-like systems. The theoretical data were taken from the work of Drake [7], who systematically calculated (for the first time) the ionization potentials of the $1s^2$, $1s2s\,^1S_0$, $1s2s\,^3S_1$, $1s2p\,^1P_1$, $1s2p\,^3P_{0,1,2}$ states in He-like systems for all elements. Moreover, Drake introduced a new method, which on the one hand resorts to variation technique, and on the other hand uses a $1/Z$ evolution for the calculation of relativistic corrections. This so-called Unified-method has the big advantage that it describes (for small Z) the electron-electron correlation exactly. The most important relativistic corrections are also taken into consideration. In addition, QED effects and the nuclear expansion (NS) were also included in the calculations (see figure 2.4). However as a result of the $1/Z$-evolution the relativistic and QED effects are not completely treated, and this leads to an uncertainty which is proportional to $(Z\alpha)^4$ [7]. Therefore the Unified-method describes the heaviest ions only relatively.

During the past years theoretical efforts have concentrated on a very precise description of the structure of the heaviest He-like ions [8, 9, 10, 11, 12, 13]. Methods including *Many Body Perturbation Theory* (MBPT [10], *Relativistic Many-Body Perturbation Theory* (RMBPT)[12]) and *Multiconfiguration Dirac-Fock* (MCDF) method [11] have been used. The latter is especially used with the Hartree-(Dirac)-Fock method and is particularly suited for calculations of the binding energies of excited states. The highest precision has been reached with

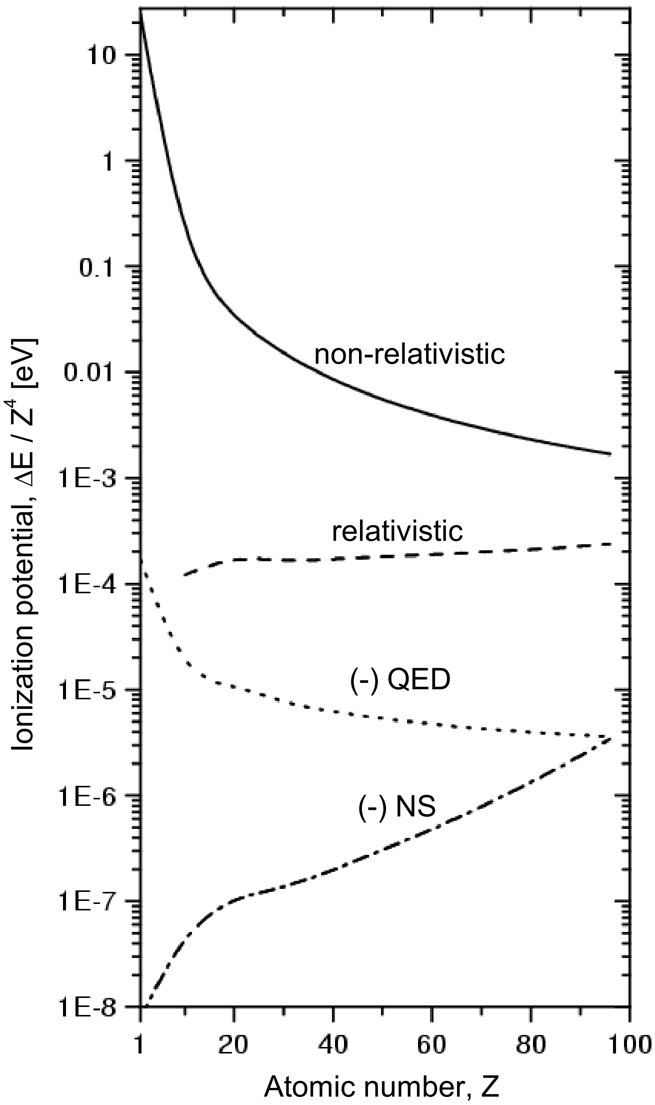

Figure 2.4: The different contributions to the absolute ionization potential in He-like systems [7]. The data refer to the $1s^2\ ^1S_0$ ground state. The corrections that lead to a reduction of the ionization potential are marked with a minus sign.

the MBPT method, which allowed (for the first time) to calculate the electron-electron correlation in relativistic systems to all orders of $Z\alpha$ [14, 12, 13]. The two-electron QED corrections should *ab initio* be introduced into the theory. Thus, it is only possible to completely describe the Breit interaction in the framework of QED [14].

2.3 Transition rates

The description of the atomic structure of few-electron systems would not be complete without mentioning the decay probabilities or transition rates. The transition rates decide in which strength transitions between atomic levels appear (in case those states have been populated), and whether or not they are observable spectroscopically. One has to mention that, almost without exceptions, all transition rates scale with Z. There is also no wonder, that the emission characteristics of light ions are completely different from those of heavy systems.

The probability for the transition of an electron from the initial state $|a>$ to the final state $|b>$, with the simultaneous emission of a photon, is:

$$dA = \frac{e^2\omega}{2\pi\hbar c}| < b|\alpha\epsilon^* e^{-i\mathbf{kr}}|a > |^2 d\Omega, \tag{2.9}$$

where $\omega = (E_a - E_b)/\hbar$ and $\mathbf{k}$ are the frequency and the momentum of the emitted photon, respectively. ϵ^* is the polarization vector and $d\Omega$ is the solid angle segment. In the extreme non-relativistic case, and taking into account the dipole approximation, $e^{-i\mathbf{kr}} \approx 1$, the total emission rate is:

$$A = \frac{4}{3}\frac{e^2\omega^3}{c^2}| < b|\mathbf{r}|a > |^2. \tag{2.10}$$

Even though (2.10) applies to light ions in particular, it is also an excellent approximation for transitions in the heaviest systems, as long as the criterion $kr \ll 1$ is fulfilled. However, if one considers ground state transitions in the heaviest one- and two-electron systems, the previous statement is no longer true. In this case the wavelength, $\lambda = 2\pi/k$, is comparable with the average orbit radius r, and requires the use of equation 2.9 taking into account higher order multipoles

$$e^{-i\mathbf{kr}} \approx 1 - i\mathbf{kr} + \mathbf{k}^2\mathbf{r}^2 \ + \ldots. \tag{2.11}$$

2.3.1 Transition rates for H-like ions

The higher order terms can, under certain conditions, contribute to and even dominate the decay of a state, in particular when dipole decay is forbidden. The most famous example is the decay of the $2s_{1/2}$-state in H-like systems. This state is metastable in hydrogen and can only decay to the ground state via the simultaneous emission of two photons ($2E1$-transition). In heavy ions it decays very fast via a magnetic dipole transition ($M1$). The transition rate for $2E1$-decay scales with Z^6, while the $M1$-rate obeys a Z^{10} dependence [15](also see figure 2.3). Furthermore, in heavy ions also electric quadrupole $E2$-decay starts to play a role and can no longer be neglected.

2.3.2 Transition rates for He-like ions

In the case of He-like ions, increasing nuclear charge leads to an essential change of the level structure (compare equation 2.6), as well as to a drastic rise of the decay rates. For very light ions, the $E1$-decay of the $1s2p$ $^1P_1$-state is the only

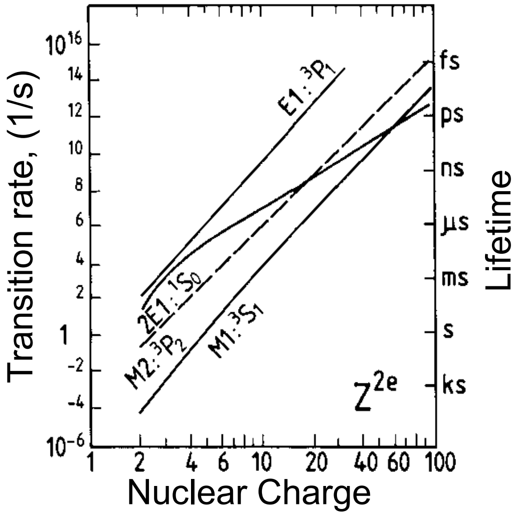

Figure 2.5: The absolute decay rates and lifetimes of the L → K transitions in He-like ions as a function of the nuclear charge (for an explanation of $2E1$-shape see the next chapter).

allowed one-photon $L \to K$ transition, while all triplet-P-states populate the $^3S_1$-level via dipole decay (see figure 2.3).

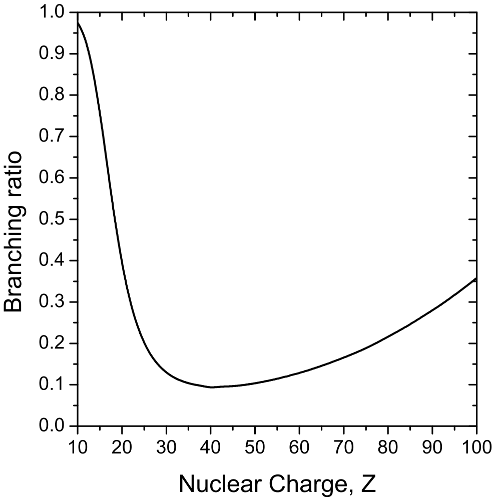

Figure 2.6: Branching ratio for the radiative decay of the $1s2p\ ^3P_2$-level to the $1s2p\ ^3S_1$-state as a function of nuclear charge for He-like ions [17].

Initial state	Final state	Transition type	$\Delta E(eV)$	$\Gamma(1/s)$
$1s2p\ ^3P_2$	$1s2p\ ^3S_1$	E1	4510.0	8.6×10^{13}
	$1s^2\ ^1S_0$	M2	100535.8	2.1×10^{14}
$1s2p\ ^3P_0$	$1s2p\ ^3S_1$	E1	252.77	1.2×10^{10}
	$1s^2\ ^1S_0$	E1M1	96282.5	5.6×10^{9}

Table 2.1: The absolute transition rates [17] and energies [7] for the decay modes of $1s2p^3P_2$- and $1s2p^3P_0$-states in He-like uranium (U^{90+}).

However, increasing Z causes an exceptionally strong increase of the rates for all forbidden transitions, with the following scaling [15, 16]: $^3P_1 \propto Z^{10}$ ($E1$), $^3S_1 \propto Z^{10}$ ($M1$), $^3P_2 \propto Z^8$ ($M2$), $^1S_0 \propto Z^6$ ($2E1$), $^3P_0 \propto Z^8$ ($E1M1$). In figure 2.5 the absolute decay rates or the lifetimes of the individual $L \to K$ transitions in He-like ions are depicted. All excited states of U^{90+} predominantly decay to the ground state via direct transitions. However, the $\Delta n = 0$ transitions of the $^3P_2$ and $^3P_0$ to the $^3S_1$ or $^1S_0$ states, respectively, play an important role, those transitions are of particular interest for spectroscopic investigations. In the decay of the ${}^3P_2$ state two competing relativistic trends are manifested. While in the low Z range with increasing Z the $M2$-decay becomes important, in the range of $Z > 38$ the trend is vice versa. In the latter case, as a result of the drastic increase of energy splitting ($\Delta E[{}^3S_1$ - ${}^3P_2]$), the Δn=0 ($2^3P_2 \rightarrow 2^3S_1$) transition becomes more important. In figure 2.6 the contribution of the $\Delta n = 0$ transitions to the total decay probability of the 2^3P_2-level is shown. In the case of U^{90+}, this state decays with a branching ratio of 30% to the 2^3S_1-level. In table 2.1 the absolute decay rates and energies for both $\Delta n = 0$ transitions are given for U^{90+}.

Chapter 3

Two-photon transitions

3.1 The simultaneous emission of two photons

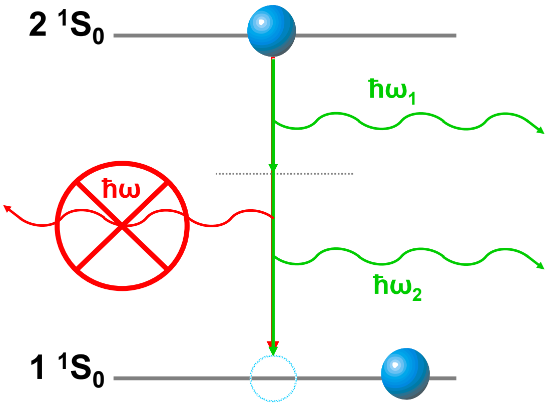

Figure 3.1: Schematic of forbidden and allowed transitions with respect to the angular momentum conservation law.

The theory of two-photon decay was first introduced by Maria Göppert-Mayer [18],[19]. Two-photon decay is a second order process, where the radiative transition between initial and final states occurs with the simultaneous emission of two-photons instead of one, which is far more common (figure 3.1). Conservation of the energy requires the sum energy of both emitted photons to be equal to the energy difference (E_0) between the initial (E_I) and the final (E_F) states, i.e.

$$\hbar\omega_1 + \hbar\omega_2 = E_I - E_F = E_0. \tag{3.1}$$

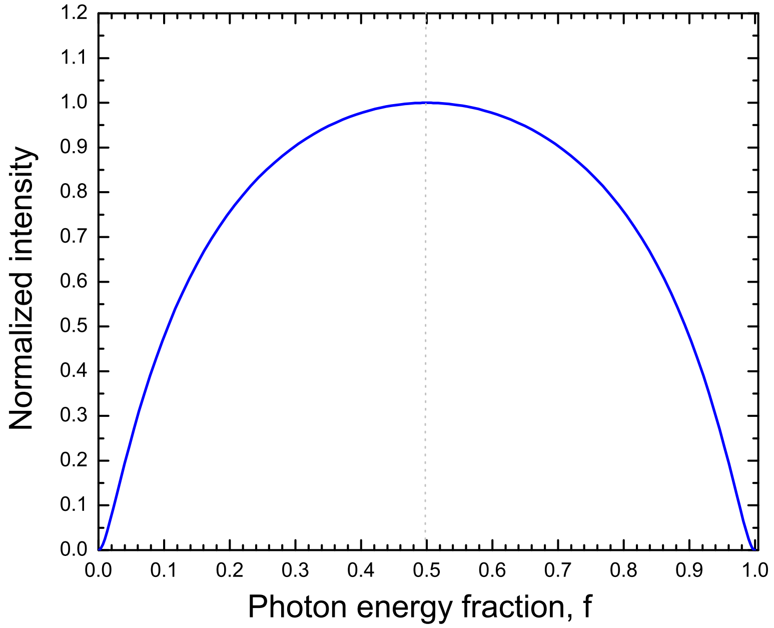

Figure 3.2: Calculated typical energy distribution of the two-photon decay of the 2 $^1S_0$-state of a He-like ion. The intensity is normalized to the middle of the distribution. The photon energy is normalized to the energy difference (E_0) between the initial and the final state (see equation 3.1).

Within this requirement, any of the photons can form a continuum energy spectrum ranging from zero to E_0 (figure 3.2). The probability for the simultaneous emission of two-photons is given by [20]:

$$A(\omega_1)d\omega_1 = \frac{\omega_1\omega_2}{(2\pi)^3c^2}|M_{fi}|^2 d\omega_1 \tag{3.2}$$

where ω_1 and ω_2 are the frequencies of the photons. M_{fi} is the matrix element of the 2E1 decay defines as

$$M_{fi} = \sum_{n=2}\left\{\frac{\langle f\|D_1\|n\rangle\langle n\|D_2\|i\rangle}{\omega_{ni}+\omega_1} + \frac{\langle f\|D_2\|n\rangle\langle n\|D_1\|i\rangle}{\omega_{ni}+\omega_2}\right\} \tag{3.3}$$

where $|i\rangle$ represents the initial state and $|n\rangle$ and $|f\rangle$ the intermediate and the final state, respectively. D_1 is the dipole operator, and ω_i is the frequency of transition i. The frequency difference ω_{ni} in the denominator is defined as $\omega_{ni} = \frac{2\pi}{h}(E_n - E_i)$. The total transition probability A_T for a transition with frequency ω_1 is obtained

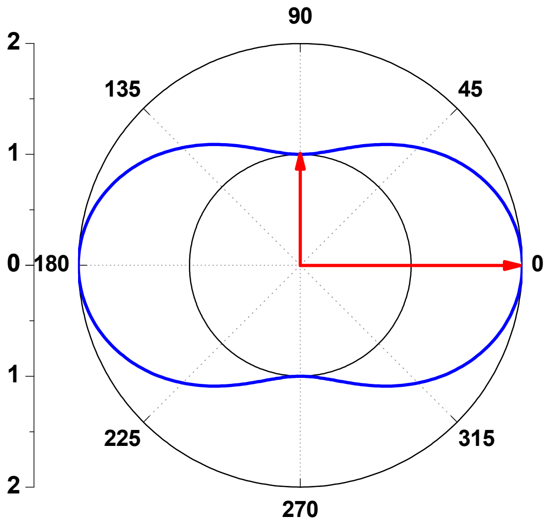

Figure 3.3: Calculated theoretical angular distribution of two-photon emission from $ns - 1s$ transition ($1 + \cos^2\theta$); θ is the angle between the two photons [79], [130], [59], [131].

by integration of equation (3.2) over the available states, i.e.

$$A_T = \frac{1}{2}\int_0^{\omega_{if}} A(\omega_1) d\omega_1 \tag{3.4}$$

The factor of $\frac{1}{2}$ takes into consideration the double counting of the photon ω_1 in the frequency interval $[0, \omega_{if}]$. The inverse of A_T represents the mean lifetime τ of the level. Besides the summation over the infinite number of intermediate states, other mathematical difficulties appear with the calculation of the two-photon decay. These, however, depend on the examined system and should therefore be discussed separately.

Along side the continuous energy distribution, both emitted photons in the $2E1$ process have an angular distribution $A(\theta)$ given by [40]:

$$A(\theta) \propto 1 + \alpha \ cos^2\theta, \tag{3.5}$$

where $\alpha = 1$ for $ns \rightarrow 1s$ transitions and θ is the angle between the emitted photons. According to equation (3.5) all angles are in principle possible (Fig. 3.3). However, as can be seen from cos^2 term, 0° and 180° are the preferred emission directions, which has experimentally been confirmed by Lipeles et al. [21]. The angular correlation is predicted to be very sensitive to relativistic corrections [41].

Hence in contrast to light ions, for very heavy ions higher order multipoles are being considered, which lead to deviations from the ideal $cos^2\theta$-distribution. Thus if all multipole interactions are included, the angular distribution deviates from the $1 + cos^2\theta$ form. In particular, there are $cos\theta-$ and $cos^3\theta-$dependent terms in the angular distribution, which result from the interference of the multipole transitions [136]. The dominant interference comes from that between the dipole and the quadrupole.

3.2 Two-photon decay in one-electron ions

A typical level scheme of the first excited states for one-electron systems is shown in figure 3.4. The scaling of the decay channels with the atomic number Z is also indicated. In ions with low Z, the total orbital angular momentum L couples with the total spin S, the so-called LS-coupling. Within this coupling scheme, the only possible one photon transitions from the excited L-states to the ground state $1s_{1/2}$ are the *Lyman-alpha* transitions, namely $2p_{3/2} \rightarrow 1s_{1/2}$ $(Ly\alpha_1)$ and $2p_{1/2} \rightarrow 1s_{1/2}$ $(Ly\alpha_2)$. Other one-photon transitions to the ground state are strictly forbidden by parity and angular momentum conservation laws. Hence, the metastable $2s_{1/2}$-state can only decay via a $2E1$-transition. In heavy ions, LS-coupling breaks down due to the very large electromagnetic fields (high-Z). Here, only the individual total angular momenta $(j = l + s)$ couple with each other, which is called jj-coupling. In high-Z ions, the $2s_{1/2}$-state can decay via a magnetic dipole $(M1)$ transition as well, which corresponds to a spin-flip transition. From the Z-scaling in figure 3.4 it can be seen that the $2E1$-decay is the dominant channel for light systems, while in heavy systems $(Z > 50)$ the $2s_{1/2}$-state decays almost exclusively via $M1$-radiation. Examples of the decay rates and transition energies for two extreme cases of one-electron systems, namely hydrogen and H-like uranium, are given in table 3.1. Note the huge difference in energy, H $\approx$ 10 eV and H-like U $\approx$ 100 keV. The data for $Ly\alpha$ lines are taken from [35], and those for the $2E1$ or $M1$ decay from [43].

Breit and Teller [44] performed the first estimation of the decay rate A_T of the $2s_{1/2}$-state in hydrogen. The matrix element (equation 3.3) was estimated in the framework of a non-relativistic treatment. Introducing the approach where the

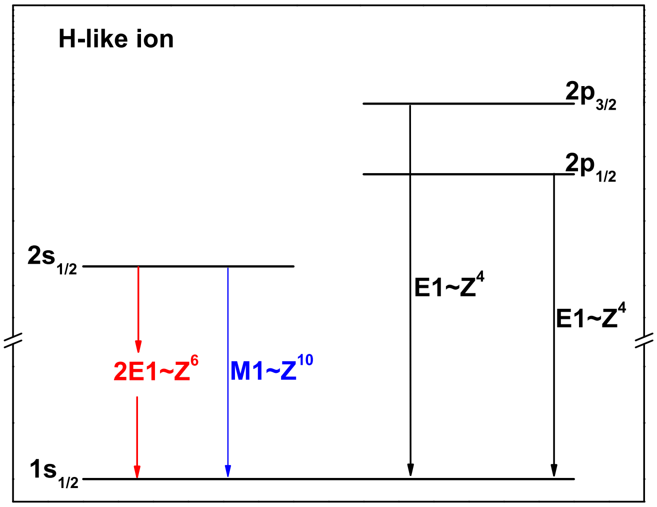

Figure 3.4: Level scheme of the first excited states of hydrogen. The scaling of the corresponding transition rates with the atomic number Z is also given.

electron in the Coulomb field is described with the help of a Green's function, one could also treat the problem analytically [45, 46], because one can attribute the spectral distribution on known Gauss hyper-geometrical functions. By extending

Transition Type	Decay rate A_T (s^{-1})		Transition energy (eV)	
	hydrogen	H-like uranium	hydrogen	H-like uranium
$2E1$ $(2s_{1/2} \to 1s_{1/2})$	8.2291	3.8251×10^{12}	$10.19881^{\star}$	$97692.148^{\star}$
$M1$ $(2s_{1/2} \to 1s_{1/2})$	2.4946×10^{-6}	1.9468×10^{14}	10.19881	97692.148
$E1$ $(2p_{3/2} \to 1s_{1/2})$	6.2648×10^{8}	3.9502×10^{16}	10.198851	102180.227
$E1$ $(2p_{1/2} \to 1s_{1/2})$	6.2649×10^{8}	4.7260×10^{16}	10.198806	97616.852

Table 3.1: Decay rates and transition energies of the lowest excited states for the two extreme cases of one-electron systems [42]. *The sum energy of two simultaneously emitted photons.

this description one can also investigate any two-photon $(2E1)$ transition from higher quantum states $ns \to 1s$ and $nd \to 1s$ [47, 48].

Another non-relativistic approach for the solution of equation (3.2), based on second order perturbation theory, was suggested by Kelsey and Macek [50]. Tung et al.[40] used this approach to solve the inhomogeneous Schrödinger equation, and to calculate the matrix element with the preserved solutions of the wave function. As a result, the two-photon ($2E1$) transition rate could be obtained with the help of multiple parametric differentiations of hypergeometric functions. Hereby any transition from the $n_1l_1m_1$- to the $n_2l_2m_2$-state can be calculated for one-electron ions. These calculations showed for the first time (for transitions from initial states with $n > 3$) sharp resonance structures for certain energies in the spectral distribution, which correspond to real cascade processes.

An alternative non-relativistic method for calculating equation (3.2) was introduced by Drake [61]. This procedure is based on the fact that the summation over infinite intermediate states is substituted with a summation over a discrete set of virtual states, which was found by diagonalization of the Hamilton operator in a finite-basis-set of the right symmetry. Only a few of these virtual states are sufficient to reproduce the result of the exact, non-relativistic, but much more extensive calculation of Klarsfeld [46]. This procedure is the most attractive due to its speed and simple numerical implementation.

All the calculations described above were carried out using the non-relativistic approximation, and therefore agree very well with the experimental data for light systems. However, for heavy systems with high Z relativistic corrections become important.

The first approach for a solution of the equation (3.2) including of relativistic corrections was made by Johnson [49] and Parpia [43]. They applied Green's function in order to solve the Dirac equation and those solutions allow one to calculate the matrix elements. The calculations clearly show, that the competing process - the magnetic dipole ($M1$) transition - becomes an issue. This decay mode becomes even more dominant for heavier systems [43]. Goldman and Drake [20] used the Finite-Base-Method for their relativistic calculation. Generalized Laguerre-functions, used as a basis set of wave functions [51] for the solution of the Dirac equation, allow one to reach a much higher precision as compared to (the precision of) usual numerical methods.

3.3 Two-photon decay in two-electron ions

In figure 3.5 the lowest excited states are schematically shown for He-like ions.The electron spins can couple to form 2 states, namely the triplet ${}^3S_1$ state ($s = 1$)

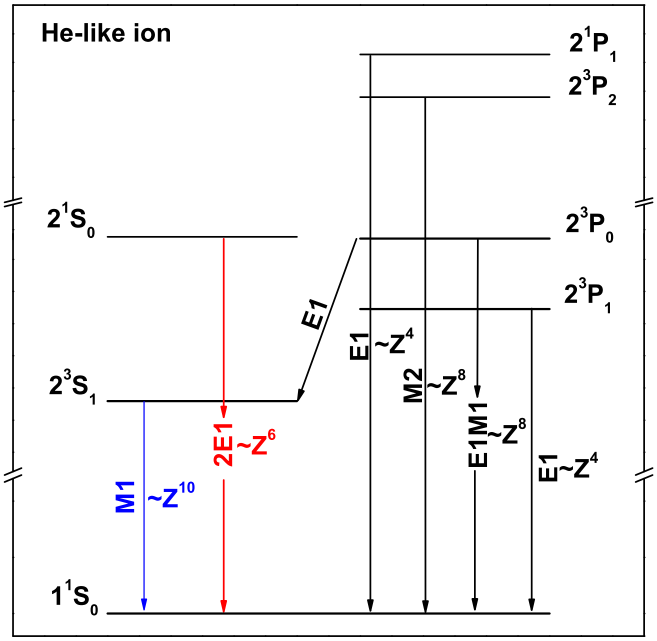

Figure 3.5: Level scheme of the first excited states of a He-like ion. The scaling of the corresponding transition rates with the atomic number (Z) is also shown.

and the singlet $^1S_0$ state ($s = 0$). The first one ($1s2s\ ^3S_1$) decays to the $^1S_0$ ground state mainly via the magnetic dipole ($M1$) transition. The two-photon ($2E1$) process can be neglected in this case because of the spin-flips requirement.
In general, for a one-photon transition with angular momentum l from an initial state with total angular momentum J_i to a final state with J_f, the following relation must be fulfilled:

$$|J_i - J_f| \leq l \leq |J_i + J_f| \tag{3.6}$$

where $J_i = 0 \rightarrow J_f = 0$ is strictly forbidden. Therefore the $1s2s\ ^1S_0$ state can only decay to the ground $1s^2\ ^1S_0$ state with the simultaneous emission of two photons. The same is true for the $1s2p\ ^3P_0$ state. In the first case two electric dipole ($E1$) photons will be emitted, while in the second case one of the emitted photons will be magnetic dipole ($M1$) radiation, and the other will be electric dipole ($E1$). Because $M1$ transitions usually have a very small decay probability, the $E1M1$-decay of the $1s2p^3P_0$ state is a very improbable transition. The calculation of two-photon ($2E1$) decay processes in He-like ions is conceptually more difficult, because of the complex nature of two-electron system.

The first evaluation of the lifetime of the $1s2s\ ^1S_0$ state in helium was performed by Dalgarno [52]. He used an explicit summation over the oscillator strengths of the discrete and continuous intermediate states. This result was also found by Victor [53] with the help of the time-dependent coupled Hartree-Fock approximation. Other non-relativistic calculations up to atomic number $Z = 34$ (krypton) were carried out by Drake [61], who uses a finite-basis-set method with correlated variational wave functions (see section 3.2).

Latter relativistic configuration-interaction calculations [62] for ions with $Z \leq 92$ were also performed. Derevianko and Johnson determined their wave functions with the variational principle, seeking extrema of the expectation value of the no-pair Hamiltonian, which includes the Coulomb and Breit interactions.

For the lightest systems, i.e. hydrogen and helium, a strong variation is already established. In figure 3.6 the two-photon ($2E1$) distributions are shown for hydrogen and helium as a function of the normalized transition energy, $\hbar\omega/\Delta E_{2E1}$. The maximum intensity (in the middle) was normalized to one [63]. The wave functions of the states in helium are changed by the electron-electron interaction, which clearly affects the energy distribution. The wave functions enter equation (3.3) directly, being different for both ions. However, because the energy eigenvalues of the states likewise depend on the wave functions, the denominator of the matrix element also changes.

3.4 Dependence of the two-photon decay properties on the atomic number Z

The spectral distributions of the two-photon decay in one- and two-electron ions have a different shape with respect to atomic number Z, as was shown by the relativistic calculations [63]. In figure 3.6 the normalized spectral distributions of the $2E1$ decay of different ions are shown.

Theoretical calculations predict a strong decrease of the intensity on the ”wings” of the distribution in H-like systems for high-Z ions, while for He-like ions in-

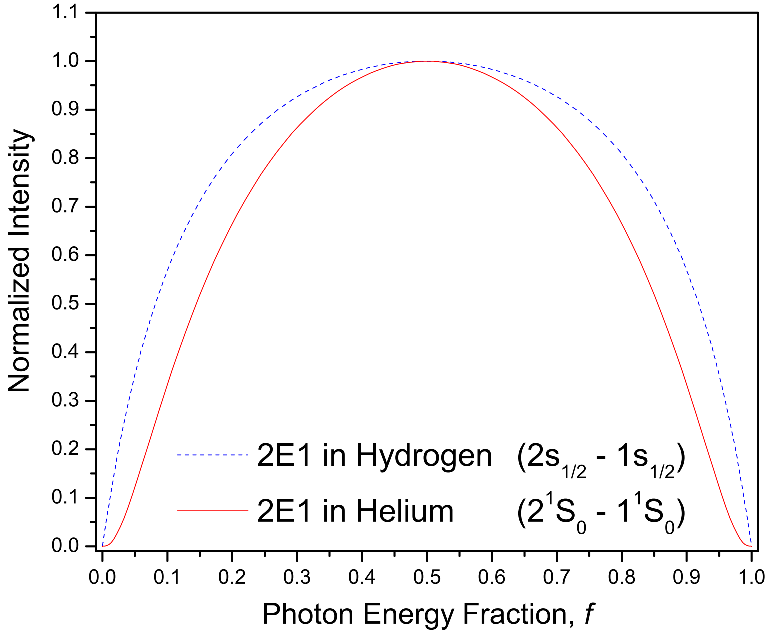

Figure 3.6: Theoretical energy distributions of the two-photon ($2E1$) decays in hydrogen and helium [63].

crease in intensity is only observed for $Z \leq 20$. Then, however, it again decreases with increasing atomic number. This behavior is due to the different Z-scaling of the different intermediate energy levels with main quantum number n. This can be seen from a rough estimate of the coupling by virtual photons in the $n \geq 2$ intermediate states. In H-like ions, the $2s - 2p$ fine structure splitting has a Z^4 dependence due to the effect of relativity. Whereas for the energy splitting between different n-shells a Z^2 dependence was found. In H-like ions, disregarding the matrix elements in equation (3.3), for high Z the $2s2p$-coupling decreases relative to the $2snp$-coupling, because $\Delta E(n = 2)/\Delta E(n > 2) \propto Z^2$. Therefore the coupling of the virtual photons appears stronger for intermediate states with $n > 2$.

The energy distribution therefore becomes more symmetric (for high Z) for both emitted photons. This is exhibited by the stronger decrease of the intensity in the wings of the distribution.

For light He-like systems the $2s2p$ energy separation is determined by the electron-electron interaction, which depends linearly on Z. For ions up to calcium

($Z \leq 20$), the $2s2p$-coupling thus becomes more important than the $2snp$-coupling for higher Z, because $\Delta E(n=2)/\Delta E(n>2) \propto 1/Z$. The asymmetry in the distribution of the transitional energy between the emitted photons becomes more and more likely leading to an increase of the intensity in the wings of the distribution. From $Z > 20$ the fine structure is the dominant contribution to the splitting of the $n = 2$ states, in analogy with H-like ions. Therefore the spectral distributions for heavy H- and He-like ions become more and more similar for higher Z. In fact, the calculation of Derevianko and Johnson showed [62] that the spectral distributions are nearly identical for the one- and two-electron uranium ions. So, for very heavy ions, statements about the spectral distribution for He-like systems can be derived from the spectral distribution for H-like systems, although the latter cannot be examined with today's experimental methods because of the dominating $M1$-decay of the initial state.

3.5 The $2E1$ decay rate and energy distribution

In figure 3.7 the first highly accurate non-relativistic calculations of the two-photon decay rates for transitions from the $2\,^1S_0$ state in He-like ions with nuclear charges Z from 2 to 92 calculated by Drake [61] are shown. The relativistic corrections to the rates were also estimated. In non-relativistic calculation of the two-photon transition, the decay rate increases with Z. In relativistic estimation Drake *et al.* [61] found that the decay rate, instead, reaches a maximum at $Z \approx 42$. The rates are reduced by the electron-electron interaction at low-Z, and by the relativistic effects at high-Z.

The first fully relativistic calculations of $2\,^1S_0$ decay rates and photon energy distributions for He-like ions with nuclear charges Z ranging from 2 to 100 have been carried out by Derevianko and Johnson [62]. In their formulation the probability per unit time for a transition from state Ψ_I to state Ψ_F, with the emission of two photons (ω_1 and ω_2) is given by [62]:

$$dw_{FI} = \frac{8}{9\pi}\alpha^6 \omega_1^3 \omega_2^3 d\omega_1 \sum_{M_1 M_2} \mid M_{M_1 M_2} \mid^2, \tag{3.7}$$

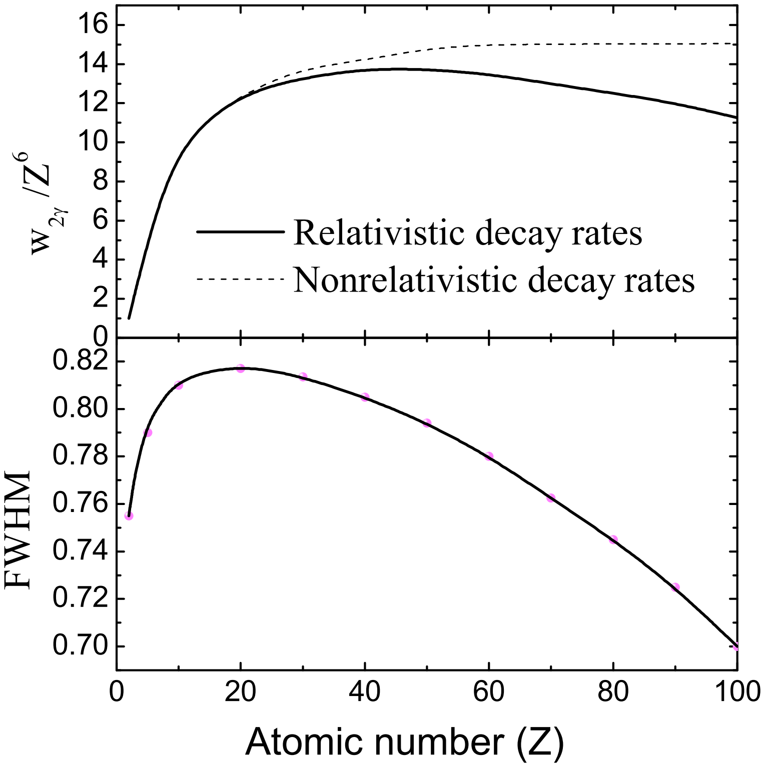

Figure 3.7: (Top panel) Comparison of relativistic and non-relativistic estimations of the decay rates for the 2 $^1S_0$ state [61]. (Lower panel) Full width at half maximum (FWHM) of the two-photon energy distribution of the 2 $^1S_0$ state ploted as a function of Z [62].

where

$$M_{M_1M_2} = -\sum_n \Big[\frac{\langle\Psi_I \mid Q_{M_2} \mid \Psi_n\rangle\langle\Psi_n \mid Q_{M_1} \mid \Psi_F\rangle}{E_n+\omega_2-E_I} + \frac{\langle\Psi_I \mid Q_{M_1} \mid \Psi_n\rangle\langle\Psi_n \mid Q_{M_2} \mid \Psi_F\rangle}{E_n+\omega_1-E_I}\Big] \tag{3.8}$$

is the two-photon matrix element. In this equation Q_M is the retarded electric-dipole operator (see Ref. [62]) Ψ_F is a relativistic wave function of the 1^1S_0 ground state of a two-electron ion and Ψ_I is a relativistic wave function of the 2^1S_0 excited state. The two-photon matrix can be expressed as a sum of two parts: a direct and an exchange matrix element [62]:

$$M_{M_2M_1} = D_{M_2M_1} + E_{M_2M_1}, \tag{3.9}$$

where the direct-matrix element $D_{M_2 M_1}$ can be written as:

$$D_{M_2 M_1} = (-1)^{1-M_2} \begin{pmatrix} 1 & J_I & 1 \\ -M_2 & M_I & M_1 \end{pmatrix} \sqrt{[J_I]} D_I \tag{3.10}$$

whereas the exchange-matrix element $E_{M_2 M_1}$ is:

$$E_{M_2 M_1} = (-1)^{1-M_1} \begin{pmatrix} 1 & J_I & 1 \\ -M_1 & M_I & M_2 \end{pmatrix} \sqrt{[J_I]} E_I \tag{3.11}$$

The explicit formulae for the direct and exchange amplitudes D_I and E_I can be found in reference [62]. Using the relations above, the two-photon matrix element can be expressed as:

$$\sum_{M_1 M_2} \mid M_{M_1 M_2} \mid^2 = \mid D_I + (-1)^{J_I} E_I \mid^2 \tag{3.12}$$

This equation shows that both, direct and exchange, contributions add coherently for the $2\ ^1S_0$ state, leading to a high sensitivity of the rate and the photon energy distribution to the relativistic corrections [62]. The final $2E1$ decay rates and energy distribution can be obtained by combining equations (3.7) and (3.12) [62]. Theoretical two-photon decay rates grow approximately as Z^6, see fig. 3.7. The full width at half maximum (FWHM) of the photon energy distribution increases with the nuclear charge as Z^2. The reduced FWHM of the $2\ ^1S_0$ energy distribution, measured in terms of the E/E_0 (see fig. 3.6), increases with as Z runs from 2 to 20, and then decreases gradually up to $Z = 100$. These changes in the distribution are due to correlation and relativistic effects, both of them are narrowing the energy distribution [62].

The relativistic calculations show that a non-relativistic approach overestimates the rate by 30% for the high-Z regime. The reduction of the decay rates for high-Z ions is caused by relativistic effects. By studying the Z-dependence of the photon energy distribution, it was found that the reduced width of the energy distribution, changes considerably as a function of Z due to an interplay between the electron-electron correlation and relativistic effects [62]. These clear influences of correlation and relativity allow one to directly test the theoretical predictions. Experimental results for low Z confirm the strong suppression of the

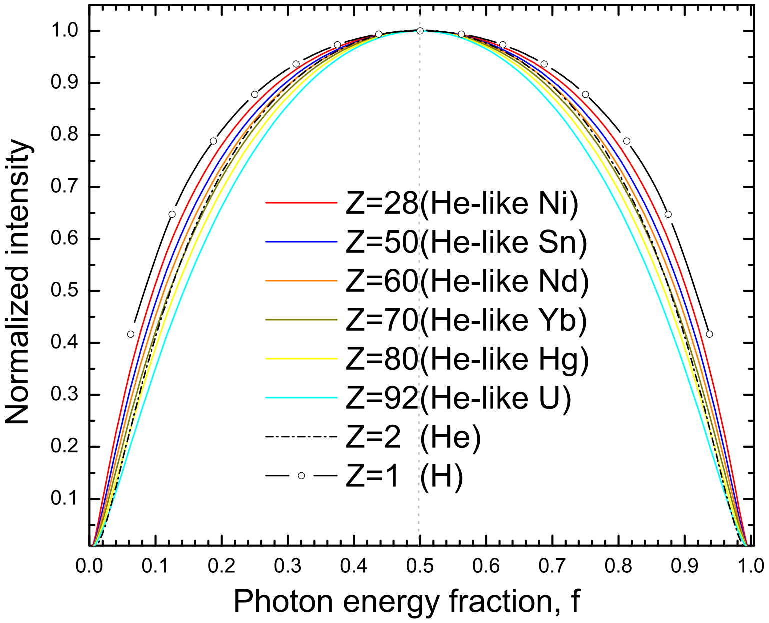

Figure 3.8: Energy distribution of the 2 $^1S_0$ - 1 $^1S_0$ two-photon transition, calculated using a relativistic approach [63].

two-photon decay rate due to the electron-electron Coulomb interaction. Investigations of the high Z regime provide accurate tests of the relativistic corrections.

3.6 Two-photon decay of ions with inner-shell vacancy

Although Göppert-Mayer published her theory of the two-photon decay in 1931, this theory was first applied to atoms with a K-shell vacancy in 1973 by Freund [54]. In the non-relativistic one-electron approximation it was shown that, for copper, the two-photon ($2E1$) emission rate is approximately 10^{-6} of the allowed $E1$-rate, and can therefore be in principle experimentally measured. The problem of the required summation over the matrix element was solved by Freund, who replaced the summation over non-occupied bound states by an integration over continuum states [55]. Several non-relativistic calculations followed this work by using a dipole approximation [56, 57] which, however, showed even stronger discrepancies with corresponding experiments.

A breakthrough in the understanding of the $2E1$ decay in atoms with a K-shell vacancy was reported by Guo [58]. Within the scope of quantum electrodynamics (QED), he showed that the problem can be dealt with by using the one-particle approximation, which is formally similar to that of the H-like ion. The only differences lie in the potential as felt by the electron, and in the procedure of the summation over initial, intermediate, and final states. Guo showed that the summation should be also performed explicitly over all occupied states and it is not in the contradiction to the Pauli principle. If such occupied states lie between the initial and final states (e.g., the $2p$ state in the two-photon transition $3d \rightarrow 1s$) than there is a large increase in the differential transition probability (intermediate-state resonance) when the energies of the photons approach the values of a cascade decay via these levels. Results of Guo's work are of particular importance, especially for transitions with initial states with $n > 2$. Tung et al. [40] and Florescu et al. [47], have already pointed out that for H-like ions, an intermediate state resonance structure occurs. This is characterized by a strong increase of the $2E1$ rate for a certain energy, which corresponds to a possible cascade. Relativistic self consistent field (SCF) calculations, which take into consideration all multipoles of the radiation field, were carried out for silver and molybdenum [59, 131]. The infinite sum over all matrix elements M_{fi} was performed with the help of the procedure by Brown et al. [60], who found the solution to the set of differential equations. In addition, Tong et al. [131] systematically examined relativistic and many-electron effects.

3.7 Earlier Two-Photon Decay Experiments

Many attempts have been made to observe the two-photon decay. As discussed earlier (chapter 3), in ions that have the ground and the excited state with spin and parity 0^+, the excited state can only decay by the simultaneous emission of two photons, each with a continuous energy spectrum, but summing up to the transition energy. As a result of the small $2E1$ branching ratio ($\approx 10^{-4}$), the two-photon transition cannot be measured so easily. In fact, there were many successful experiments aiming mainly for measurements of the decay rates/lifetimes of this exotic transition. However, investigations of the (shape of) spectral distribution are far more rare.

The existence of spontaneous two-photon decay was first experimentally verified by Lipeles, Novick and Tolk [21]. Normally for hydrogen, the two-photon continuum is not observable, because in plasmas the Stark effect, caused by the electric fields of ions and electrons, leads to a mixing of the $2s$ and $2p$ levels, and thus to a quenching of the $2s$ state by the $2p$ state. However, with increasing Z the two-photon rate becomes much larger and, moreover, the Stark quenching rate is reduced considerably. For these reasons, it proved possible to detect simultaneous two-photon emission in an ionized helium beam, using coincidence photon-counting techniques. Lipeles et al. detected two-photon coincidences from a He^+ $2s_{1/2}$ beam. Even though, all photons wavelengths ranging from 300 to 1200 $\mathring{A}$ were registered, a lack of knowledge about the detector efficiency did not allow for a precise determination of the two-photon decay rate.

R. C. Elton et al. [64] first obtained the two-photon frequency distribution. They observed a deuterium-neon plasma using a 2.2-m grazing-incidence grating spectrometer where a photographic plate served as a detector. However, almost over the whole range the two-photon continuum was contaminated with x-rays from the gases present in the plasma.

Two-photon emission (x-rays) from inner-shell transitions has been observed for the first time by Bannett and Freund in 1982 [74, 82]. Vacancies were produced by irradiating a thin Mo foil with Ag x-rays from a sealed x-ray tube. As in previous measurements [21, 24], they detected both emitted photons in fast time coincidence, which served to minimize the effects of the large one-photon background. They measured both $2s \rightarrow 1s$ and $3d \rightarrow 1s$ decays in molybdenum. The continuum shape was observed over a restricted energy range near the midpoint of the distribution. The data for the $3d \rightarrow 1s$ decay were consistent with the expected intermediate-state resonance. However, the observation of a coincidence event does not usually guarantee that true two-photon emission is observed. In addition to fast atomic cascades that appear coincident on the $\sim 10^{-7}s$ time scale of the apparatus, there are other true two-photon processes, such as double-Compton scattering, which may be of appreciable intensity. Also, cross-talk between the detectors is an intrinsic problem induced by the large one-photon flux. The elucidation and elimination of such interfering phenomena are, in fact, the most time-consuming aspects of this technique.

Besides in few-electron systems, as investigated by Bannett and Freund, the two-photon decay was also observed in many-electron systems with a K-shell vacancy. Ilakovac with co-workers [83, 75, 76] performed experiments where the K-shell vacancy in an atom was produced via inner-shell electron capture. Two detectors were used to measure, in coincidence, the x-rays from transitions inside the hollow atoms. Two-photon emission in $2s \rightarrow 1s$, $3s \rightarrow 1s$, $3d \rightarrow 1s$ and $4s, d \rightarrow 1s$ transitions were observed and compared with various theoretical calculations. Thus the fact that resonance structures (see section 3.6) should appear in the spectral distribution has been confirmed experimentally.

After a pioneering study of the $2s \rightarrow 1s$ transition in ionized helium by Novick and co-workers [80, 21], their basic method was subsequently expanded by Marrus and Schmieder [24, 65]. They have performed the first experiments aiming on the lifetime measurements in the middle-Z range with the help of beam foil spectroscopy of accelerated ions for the $2s_{1/2}$-state in H-like and 2^1S_0-state in He-like argon.

This method was used to observe the two-photon continuum in H-like Ni [66], Kr [67], and Nb [31], and in He-like Ni [66], Br [68], Kr [29], and Ag [31]. These experiments resulted in measurements of the lifetimes of the two-photon-emitting states, but detailed measurements of the shapes of the continua were not attempted. The continuum radiation from double-photon decay was also observed in connection with studies of resonant transfer and excitation in He-like Ge [33], and Kr [69, 70]. These experiments pointed to a technique for selective excitation of the $2\ {}^1S_0$ level in He-like ions, which could be important in future studies.

The experimental conditions for lifetime measurements (e.g. Br [68]) in such a technique were not optimum for measuring the distribution of the two-photon decay. One reason was that, in the experiment, intense low-energy lines were blocked using mylar absorbers. This was necessary in order to reduce the accidental coincidence rate, but it also restricted the range over which one could observe the two-photon continuum. In addition, much of the integration time in that experiment was spent with the foil at large distances from the detectors (i.e. many decay lengths) where the two-photon rate was low. So, a dedicated experiment was needed to measure the continuum shape. In planning such an experiment, many efforts have to be made to maximize the sensitivity to low-energy x-rays, and the foil position and detector geometry need to be chosen such that the two-photon-coincidence rate is optimised.

The shape of the two-photon decay from the $1s2s\ ^1S_0$ state in He-like krypton was measured by Ali and co-workers [35]. The desired initial state was populated via excitation of the Kr^{34+} beam by a thin carbon foil. Experimentally, coincidences between pairs of Si(Li) detectors, whose efficiencies as a function of photon energy had been measured over a broad range (1-15 keV), had to be registered. However, the comparison with theory was made with the aid of a Monte Carlo simulation. Although the results were in agreement with the non-relativistic calculations of Drake, the errors in the simulation, due to uncertainties in detector efficiencies, were of the order of the difference between the theoretical shapes for helium (Z=2) and He-like Kr (Z=36). Therefore, this measurement was not of sufficient precision to provide the needed determination of the spectral shape for medium-Z ions. Because it appeared difficult to significantly improve the determination of the efficiency of the Si(Li) detectors, particularly in the region below 3 keV, **a new experimental approach was needed**.

In their experiment with nickel [36], Schäffer et al. were able to partially remove the former limitations by measuring the two-photon decay in both H- and He-like nickel in the same experiment, switching between the two ions several times during the measurement. Since the continuum shape in the two-photon decay of the $^2S_{1/2}$ level in hydrogen-like nickel was known precisely, this served as a calibration of the spectral efficiency of the detection system. In fact, there was an improvement over previous measurements of the shape of the continuum radiation from the $2\ ^1S_0$ state in He-like krypton. They proved the fact that measurements of the two-photon distribution provide a viable means for testing theoretical calculations of two-photon transition probabilities. However, there was a need for sensitivity to the relativistic corrections, in particular for medium-Z. As discussed in chapter 3, the theoretical curves (figure 3.8) suggest that the best approach is to extend the data to the wings of the energy distribution where the relativistic effects are largest. To do this one needs to improve the coincidence detection efficiency at low energy, which is a non-trivial challenge.

Sensitivity below 1 keV could be improved by using windowless detectors, but a more difficult problem is the poor time resolution at low energy.

Using a similar photon-photon coincidence technique, Schäffer at al. also performed measurements of the spectral shape of the $2E1$ in He-like gold [71, 72, 38, 73]. Here, the systematic errors in the Monte Carlo simulation were limiting the accuracy of the comparison between theory and experiment.

Chapter 4

Experimental Approach for Studying Exotic Transitions

4.1 Collisions of Highly Charged Ions.

The interaction processes of highly charged ions with matter are important to all experiments that deal with the atomic structure of heavy few-electron systems. But also accelerator relevant research, that deals with the production and acceleration of highly charged ions, requires a deep understanding of atomic physics processes. Central questions in this connection are:

- Production of a specific charge state,
- Charge-exchange cross-sections for ions in a specific charge state,
- Selective population of specific atomic levels (states).

Heavy systems are an extremely exotic state of matter, and its dynamics as well as its structure are substantially affected by the physics of strong ($Z\alpha \rightarrow 1$) fields. In this sense the structure and the dynamic of heavy highly charged ions are closely coupled with each other. In the following the processes most relevant for this work will be discussed, namely ionization and excitation in relativistic collisions of highly charged ions with matter.

4.2 Ionization and Excitation Processes

In relativistic collisions of highly charged ions and gas atoms (molecules) the K-shell ionization plays an extremely important if not the most important role. Using perturbation theory in asymmetrical collision systems can be treated fairly accurately, so long as the condition $Z_T \ll Z_P$ is fulfilled. In the simplest case, the projectile moves with speed v along a straight trajectory in z-direction. The projectile movement follows, in this case, the classical expression $\mathbf{R}(t)$=$\mathbf{b}$+$\mathbf{v}t$, where $\mathbf{b}$ is the impact parameter with respect to the target nuclei. The Liénard-Wiechert potential than describes the potential, caused by the charged projectile in the system of the target [84]:

$$\Phi(\mathbf{r}, t) = \frac{\gamma Z_P e}{r'}$$
$$\mathbf{A}(\mathbf{r}, t) = \frac{\mathbf{v}}{c}\Phi(\mathbf{r}, t), \tag{4.1}$$

The path of the ejected electron, in the projectile system, is expressed by

$$r'(t) = \sqrt{(x-b)^2 + y^2 + \gamma^2(z - vt)^2}, \tag{4.2}$$

where the coordinates of the electron in the projectile frame is given by (x, y, z, t). In this description the bound electron of the projectile is perturbed by the Coulomb potential $Z_T e/r$ of the target (where e is the elementary charge and r is the electron coordinate measured from the target).

Taking into account the Liénard-Wiechert potential, and following the solution of the time-dependent Dirac equation, the amplitude for a transition from the initial state ϕ_i to the final electronic state ϕ_f is given by

$$A^e_{fi}(b) = i\frac{\gamma Z_P e^2}{\hbar}\int dt\ e^{i(E_f - E_i)t/\hbar}\int d^3r\ \phi^\dagger_f(r)(1 - \beta\alpha_z)\frac{1}{r'}\phi_i(r). \tag{4.3}$$

One has to mention that, in contrast to non-relativistic collisions, as a result of the Liénard-Wiechert potential the transition amplitude contains two contributions, namely an electric $(1/r')$ and a magnetic contribution $(\beta\alpha_z/r')$, which must be added coherently. The magnetic term is often referred to as the *transverse* contribution to the ionization. The cross section can be expressed as follows

$$\sigma_{fi} = 2\pi\int_0^\infty |A^e_{fi}|^2\ b\ db. \tag{4.4}$$

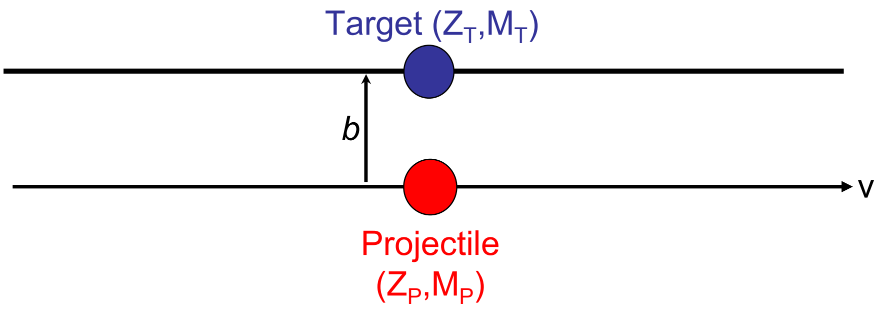

Figure 4.1: Impact parameter (b) in collision of ion (projectile) with atom (target).

where b denotes the impact parameter (see figure 4.1). However, the ionization cross-section σ_{fi} must be substituted by an energy differential expression, which would require an additional integration over all continuum states, however this numerical treatment is very time-consuming. Hence, in practice one often uses the suggestion of Anholt [85, 86], which is a non-relativistic treatment within the scope of the *Plane-Wave-Born-Approximation* (PWBA) or *Semi-Classical-Approximation* [87]. It can be shown that the ionization cross section σ_L^{ION} (also often called as *longitudinal* ionization cross section) follows a scaling law, which is given by

$$\sigma_L^{ION} = const \cdot \frac{Z_T^2}{Z_P^4} \mathcal{F}(\frac{v}{v_K}), \tag{4.5}$$

where v_K is the speed of the *active* K-shell electron. The function $\mathcal{F}$ reaches its maximum at $v/v_K \approx 1$ (see e.g. [87]). In order to take the influence caused by the relativistic wave functions of the heavy projectile into account, equation 4.5 can, in first approximation, be multiplied by

$$F = \left[1 + \left\{\frac{\alpha Z_P}{2}\right\}^2\right]. \tag{4.6}$$

In the end, the so-called transversal contribution to the ionization cross section must be considered as well. Within the scope of the dipole approximation, the transversal cross section is given by

$$\sigma_T^{ION} = \sigma_L^{ION} \cdot \frac{ln(\gamma^2) - \beta^2}{ln(\beta^2)/E_K}. \tag{4.7}$$

The entire ionization cross section is given therefore by:

$$\sigma^{ION} = F \cdot [\sigma_L^{ION} + \sigma_T^{ION}]. \tag{4.8}$$

An overview of all experimental data, compared to the discussed theoretical model, can be found in reference [88]. A detailed discussion of the approximation can be found in reference [84].

4.3 Selective Generation of Excited States in Few-Electron Ions

In order to perform a high-precision experiment of the two-photon decay, effective and reliable creation of the desired initial excited state would result in an extreme improvement in experimental accuracy.

A very effective way is to create the initial $1s2s$ state by selective ionization of a $1s$ electron in a Li-like ion (via a relativistic collision with a nitrogen molecule in a storage ring). In this process, the other two electrons are basically not affected (see figure 4.2).

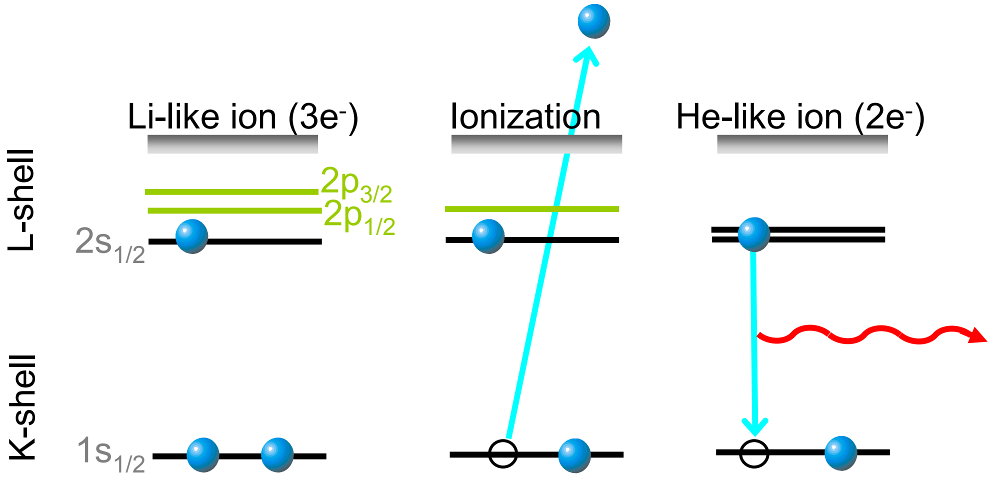

Figure 4.2: Production of the excited $1s2s$ state by selective K-shell ionization. One K-shell electron is ionized without disturbing the remaining two electrons.

The high selectivity can be explained by a simplified treatment of the dynamics of the K-shell ionization process in relativistic ion-atom collisions involving few-electron projectiles. First, one can assume that the process of interest can be treated as a two-step process, where in the first step ionization occurs, and in the second step the formation of the specific states in the He-like ion takes place independently. The latter step would be treated by considering the rearrangement of the atomic orbitals only.

For the first step one assumes that the K-shell ionization can be treated within the independent particle approximation, and that the same holds true for possible inner and intra-shell excitations of the $2s$ electron of the Li-like ion occurring simultaneously within the collision. The motivation for this approach is that the general many-body problem one deals with, can be reduced to a single-electron problem. The framework of an independent particle approximation postulates that the change of state of one electron does not affect the other one. In other words, it is assumed that excitation and ionization are not correlated. A further calculation assumes that the inter-nuclear motion can be treated classically, i.e. that the projectile trajectory can be well approximated by a straight line, characterized by the impact parameter b. In this approach, the probability $p_{nlj}^{\mathrm{ion-exc}}$ for simultaneous ionization and excitation of a ground state electron into a final nlj state of the projectile, can be expressed as an (uncorrelated) product of single-electron probabilities:

$$p_{nlj}^{\mathrm{ion-exc}}(b) \approx 2\, p^{\mathrm{ion}}(b)\, p_{nlj}^{\mathrm{exc}}(b). \tag{4.9}$$

Here, $p^{\mathrm{ion}}(b)$ is the single-electron ionization probability for a collision with impact parameter b, and $p_{nlj}^{\mathrm{exc}}(b)$ is the single-electron excitation probability into the state characterized by quantum numbers nlj.

Expression (4.9) is based on the assumption that bound projectile electrons excited and ejected simultaneously. The total cross-section for simultaneous excitation and ionization into the nlj state of the projectile is then given by:

$$\sigma_{nlj}^{\mathrm{ion-exc}} = \int_0^\infty 2\pi\, b\, p_{nlj}^{\mathrm{ion-exc}}(b) db. \tag{4.10}$$

The description of simultaneous excitation and ionization within the IPA framework requires an impact parameter formulation for the individual single-electron processes (see Eqs. 4.9,4.10).

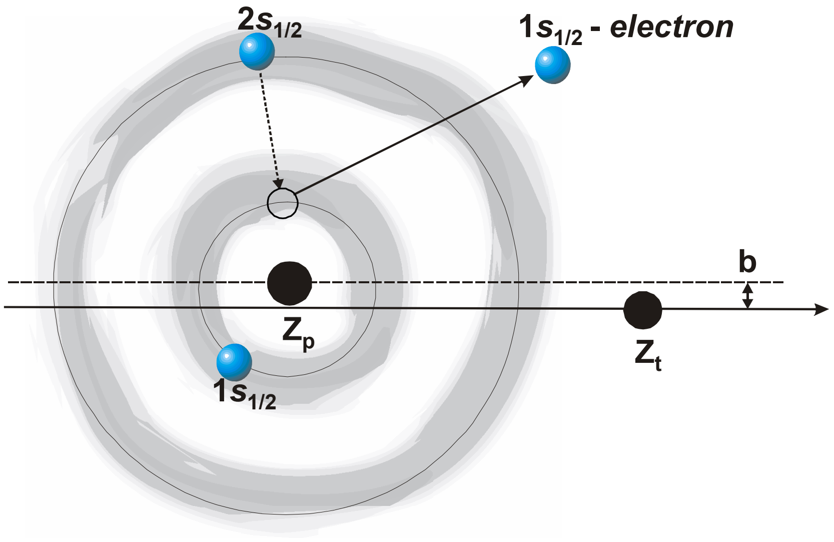

Figure 4.3: Impact parameter dependent description of the ionization/excitation processes.

4.3.1 Ionization and excitation probabilities

For the description of impact parameter-dependent ionization, the semi-classical-approximation (SCA) [112] can be adopted. In the SCA, the ionization probability $p^{\text{ion}}(b)$ is determined within first order perturbation theory, assuming that the perturbation potential can be derived according to the classical inter-nuclear trajectory. The calculations are performed with the SCA code of Trautmann and Rösel [113], which exploits relativistic hydrogenic-like wave-functions for the description of the bound state of the projectile electron. A theoretical binding energy of H-like uranium [114], and the continuum electron states with angular momentum $0 \leq \ell \leq 4$ can be used. In the SCA calculations, the correct relativistic Dirac bound-state and continuum-state wave-functions are used. However, this model neglects the magnetic part of the full interaction potential, and assumes non-relativistic collision kinematics. The latter is accounted for by adopting a collision energy for which the projectile velocity matches that given by the relativistic expression. Note, that such a rough treatment might be justified due to the moderate γ-values of relevance for the collisions considered here ($\gamma = 1.10$

and $\gamma = 1.43$ for 98 MeV/u and 398 MeV/u uranium energies correspondingly).

For the description of electron excitation, a fully relativistic calculation, considering a complete (Liénard-Wiechert) interaction potential, can been used (see Ref. [105] for a detailed description). In the impact parameter picture, similarly to ionization, the cross section for excitation is given by Eq.(4.4). Within first-order perturbation theory, the transition amplitude in a strictly relativistic formalism has the form as given by Eq.(4.3) [115]. For the description of initial and final electron states, the Coulomb-Dirac wave-functions are used. For the binding energies, however, the relevant ones for the states in Li-like uranium are adopted. One has to point out here that, the perturbation description of K-shell ionization and/or excitation can be used only for fast collisions ($v_p \gg v_K$), where v_p and v_K are the projectile and K-shell electron velocities, respectively. In the case of the K-shell electrons in uranium ($v_K \approx 0.67$) the projectile velocities used in our experiment are just at the limit. For the highest collision energy (398 MeV/u) we have $v_p \approx 0.71$, while for the lowest one (98 MeV/u) $v_p \approx 0.43$, which is considerably below v_K.

4.3.2 Simultaneous excitation and ionization in the IPA framework

Figure 4.4 shows the theoretical probabilities for ionization and excitation as a function of the impact parameter. The $1s$ ionization probabilities attain their maximum already at an impact parameter $b \approx 1\lambda_c$ ($\lambda_c \simeq 386$ fm) and rapidly decrease by many orders of magnitude for $b \approx 20\lambda_c$. The probabilities for $2s - 2p_{1/2}$ and $2s - 2p_{3/2}$ excitation first rise, and then remain almost constant. This means that $2s$ excitation is the dominant process during the relevant collisions.

In addition, figure 4.4 also shows the reduced cross-section for simultaneous excitation and ionization, calculated according to equation (4.9). Due to its multiplicative nature, the cross-section for excitation and ionization is completely suppressed at large impact parameters. Thus, the probabilities for simultaneous $1s$ ionization and $2s$ excitation are many orders of magnitude smaller than all other impact parameters. Therefore, one can conclude, that in relativistic collisions leading to the K-shell ionization of Li-like systems, despite of a relatively

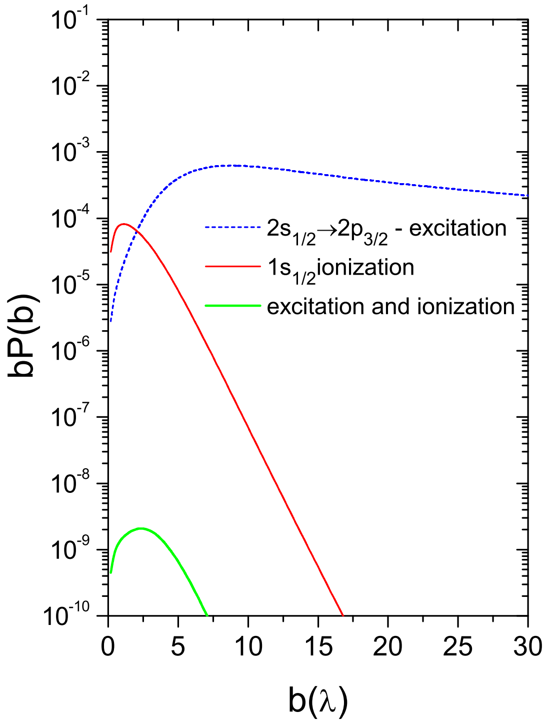

Figure 4.4: The $1s_{1/2}$ ionization and/or $2s_{1/2}$ excitation probabilities for relativistic 398 MeV/u $U^{89+} \rightarrow N_2$ collisions as a function of the impact parameter b(λ); with λ - Compton wavelength [104], [105].

strong ion-atom interaction, the other two electrons remain unaffected.

4.3.3 Relaxation of Electron Orbitals

Because hydrogen-like wave functions were used for the calculation, it was not possible to obtain theoretical information on the population of S-substates in He-like system by the theoretical concept applied. Therefore, the theoretical study on the relaxation properties of the $2s_{1/2}$ orbitals of the initial $(1s^2 2s)\ {}^2S_{1/2}$ state in Li-like uranium, and two possible excited states $(1s2s)\ {}^1S_0$ and $(1s2s)$ ${}^3S_1$ in He-like system was extended. These calculations have been performed by using the GRASP package, which is based on the multi-configuration Dirac-Fock (MCDF) method [116]. It was found that in the $[1s2s]_{J=1}$ and $[1s2s]_{J=0}$ states of He-like uranium, the $2s$ orbital radii are slightly different. For the J=1 and J=0 states the values of the average $2s$ orbital radii are 5.38×10^{-2} and 5.47×10^{-2}

atomic units, respectively. The average 2s orbital radius in the initial $[1s^2 2s]$ state of Li-like uranium is 5.43×10^{-2} atomic units.

In the next step the theoretical values for the overlap integral (rearrangement probabilities) of the $2s$ electron in the initial ${}^2S_{1/2}$ state of Li-like uranium, and in the final ${}^1S_0$ and ${}^3S_1$ states in He-like uranium are determined using the sudden perturbation (SP) approximation [117]. In this approximation, the probability for the rearrangement of the $[1s_{1/2}2s_{1/2}]$ electrons from the initial $\langle i|$ state of Li-like uranium into the final $|f\rangle$ excited states of the He-like uranium, can be expressed as

$$P(i \rightarrow f) = |\langle i|f\rangle|^2. \tag{4.11}$$

Because of the relatively weak dependence of the radial overlap of the $1s$ electrons on the $2s$ electron state, the rearrangement probability can be calculated in the relaxed-orbital single-channel Hartree-Fock approximation proposed in ref. [118]. In this approximation, the assumption is made that the $1s$ ionized electron escapes from Li-like uranium so quickly, that the remaining $[1s2s]$ electrons have sudden change of the effective potential as seen by the electron. Due to the new field, created by the nucleus and remaining $[1s2s]$ electrons, new states 2^1S_0 or 2^3S_1 states (figure 3.5) of the He-like system are formed by relaxation (rearrangement). Theoretical rearrangement probabilities, calculated as the square of the overlap integral of the $2s$ electron radial orbitals in the initial ${}^2S_{1/2}$ (Li-like system) and the final 2^1S_0 and 2^3S_1 states (He-like system), are

$$\left|\left\langle \Psi^i_{2s}\left({}^2S_{1/2}\right) \mid \Psi^f_{2s}\left(2^3S_1\right)\right\rangle\right|^2 = 0.998 \tag{4.12}$$

and

$$\left|\left\langle \Psi^i_{2s}\left({}^2S_{1/2}\right) \mid \Psi^f_{2s}\left(2^1S_0\right)\right\rangle\right|^2 = 0.994, \tag{4.13}$$

respectively. Both values are high and very close to each other. The probabilities for a rearrangement of the $2s$ electron into the 3^1S_0 and 3^3S_1 states are a few orders of magnitude smaller than those for the n=2 S-states, namely

$$\left|\left\langle \Psi^i_{2s}\left({}^2S_{1/2}\right) \mid \Psi^f_{3s}\left({}^{1,3}S\right)\right\rangle\right|^2 < 10^{-4}. \tag{4.14}$$

Chapter 5

Experimental Facility

The possibility to perform experimental investigations of two-photon transitions, and other high-quality experiments, is given by the GSI facility. The recent achievements in producing, accelerating, cooling and storing of heavy highly-charged ions at the SchwerIonen Synchrotron (SIS) and the Experimental Storage Ring (ESR) provide unique and clean conditions for two-photon decay investigations in the high-Z regime.

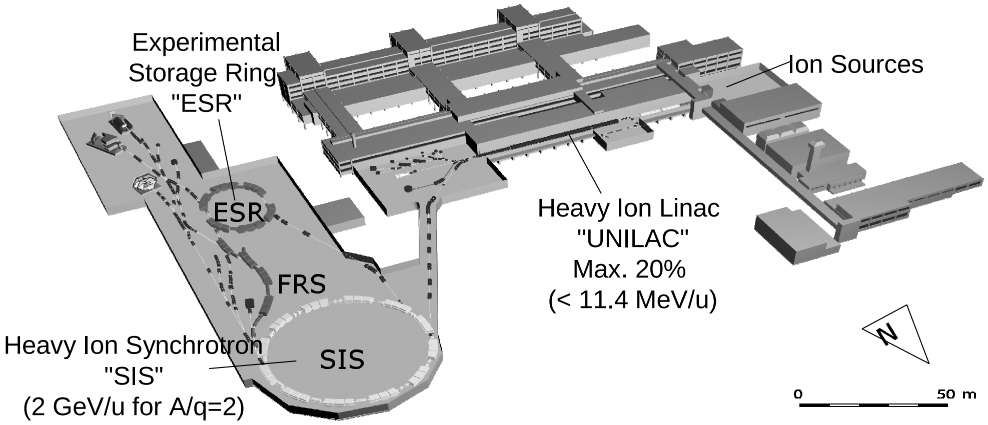
Experimental
Storage Ring
"ESR"
Ion Sources
ESR
FRS
Heavy Ion Linac
"UNILAC"
Max. 20%
(< 11.4 MeV/u)
Heavy Ion Synchrotron
"SIS"
(2 GeV/u for A/q=2)
SIS
N
0
50 m

Figure 5.1: Layout of the accelerator facility at GSI, showing the linear accelerator UNILAC, the heavy-ion synchrotron SIS18, and the experimental storage ring ESR.

5.1 The GSI Accelerator Facility

The GSI accelerator facility (see figure 5.1) consists of the UNILAC linear accelerator, where low-charged ions are accelerated to an energy of 11.4 MeV/u. The production of the desired ion charge species is accomplished by extracting the ions from the UNILAC, and subsequently injecting them into the transfer line towards the experimental installations. In the transfer line the ions pass through stripper foil. The thickness and the material of the stripper foil is chosen in an optimal way so that the yield of the desired charge-state is maximal. As an example, in fig. 5.2 is shown the calculated charge-state distribution for 300 MeV/u uranium ions impinging on Cu (top panel), Al (middle panel) and

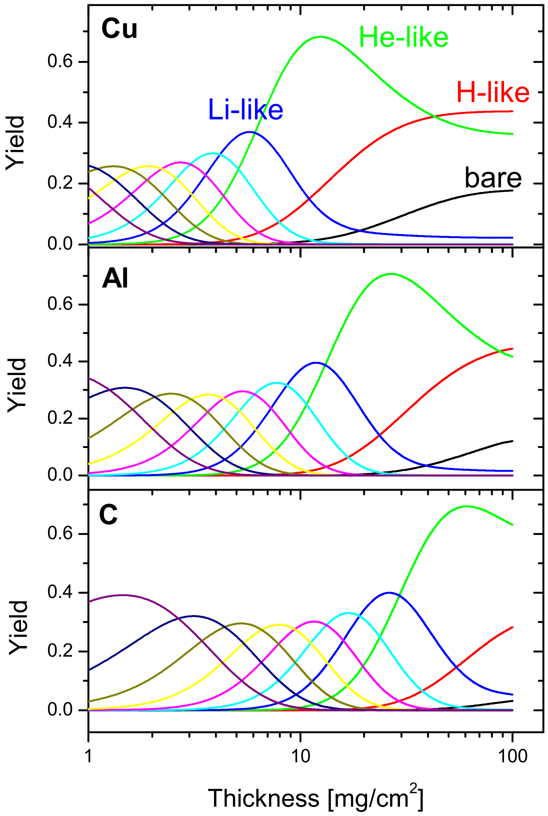

Figure 5.2: Calculated charge-state evolution as a function of target thickness for 300 MeV/u uranium ions impinging on Cu (top panel), Al (middle panel) and C (bottom panel) targets. Colors of the lines define different charge-states (black lines for bare ions, red - H-like, green - He-like, blue - Li-like etc.)

C (bottom panel) targets. The calculations were performed with the help of the GLOBAL code [89], which was developed in order to estimate ionic charge-state distributions of relativistic projectiles traversing solid and gaseous targets.

From the emerging charge state distributions, the fraction of the ions with the desired charge state is magnetically separated and directed towards the heavy-ion synchrotron SIS. In the SIS, the ions are subject to a further acceleration up to the desired energy. The stripping procedure can also be done after the acceleration in the SIS. The produced species are finally injected into the experimental storage ring ESR.

5.2 Experimental Storage Ring

A unique part of the GSI accelerator facility is the experimental storage ring (ESR) [94], which is shown in figure 5.3. The circumference of the ESR amounts to 108 m, and its magnetic rigidity to 10 Tm. The injected hot ion beam, which has a typical emittance of about 5π mm mrad, is very efficiently cooled via the Coulomb interaction with the electrons in the electron cooler (see figure 5.4). For efficient cooling of high-energy beams, stochastic cooling is applied [95]. Cooling reduces the emittance to 0.1π mm mrad or less, and provides beam diameters of less than 5 mm. The emittance is particularly important for precise measurements at the jet target, where full control over geometrical factors and possible Doppler corrections is required.

The relative longitudinal momentum spread of the injected ion beam after cooling is reduced from $\Delta p/p \approx 10^{-3}$ to about 10^{-5}. This can be deduced from the signal of a pickup via Schottky noise spectrum of the circulating ions [90, 91, 92]. As an example, a Schottky frequency spectrum of a cooled ion beam in comparison with the initial (uncooled) one is given in Fig. 5.5. Electron cooling also guarantees a well-defined beam velocity and therefore energy. The absolut beam energy is basically determined by the electron cooler voltage and by the space charge of the electron beam. The uncertainty in the beam energy is due to a possible offset in the power supplies of the electron cooler, and can be estimated to amount ±10 V. For a detailed discussion of the electron cooling technique see [93]. Another important feature of the ESR is that many (highly-charged)

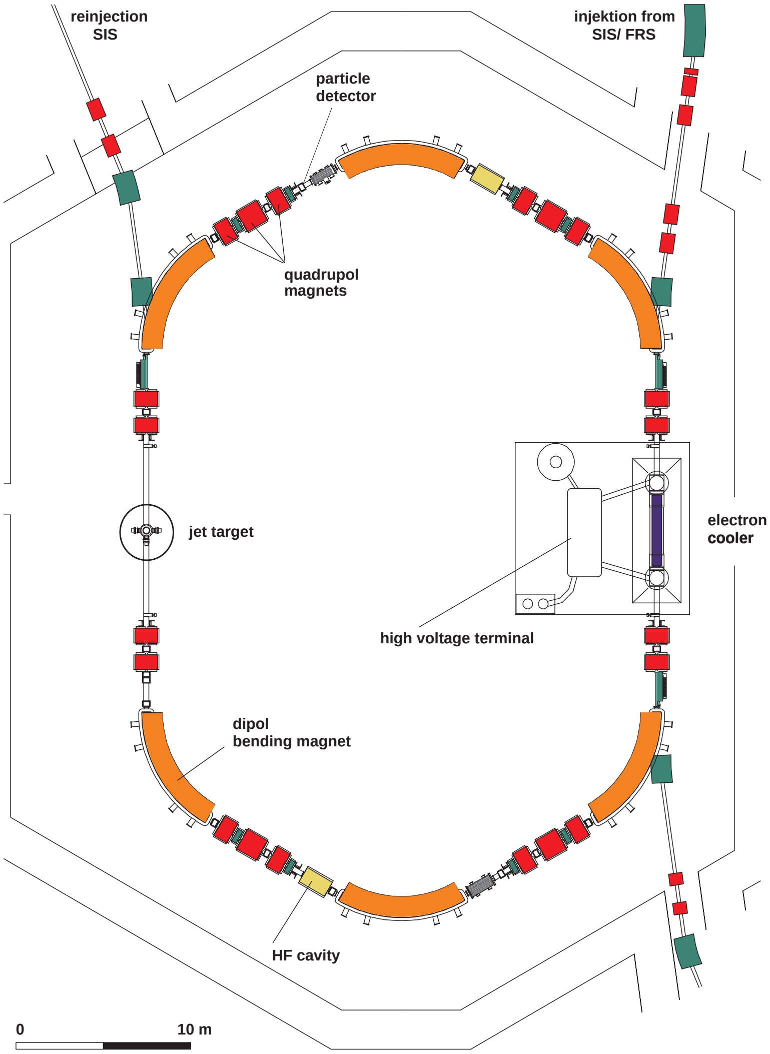
reinjection
SIS
injektion from
SIS/ FRS
particle
detector
quadrupol
magnets
jet target
electron
cooler
high voltage terminal
dipol
bending magnet
HF cavity
0
10 m

Figure 5.3: Schematic of the storage and cooler ring ESR at GSI. The layout depicts the beam guiding system (dipole bending magnets, quadrupoles and hexapoles) as well as the most important installations for beam handling and diagnostics (kicker, rf cavities, Schottky noise pick-up, electron cooler). The position of the internal jet-target is marked in addition.

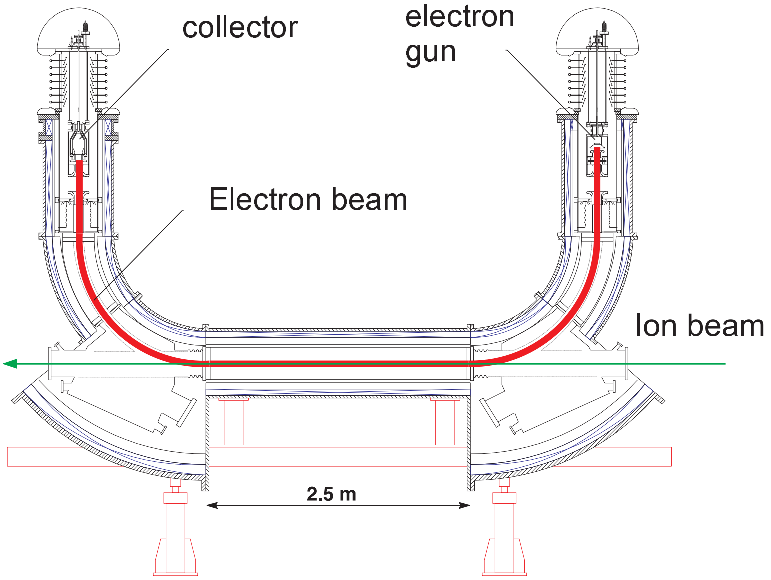

Figure 5.4: Layout of the electron cooler device used at the storage and cooler ring ESR. Electrons produced in the electron gun at a cathode temperature of ≈ 1300 K are guided by a ≈0.1 T magnetic field co-propagating over a distance of 2 m with the stored ion beam [93].

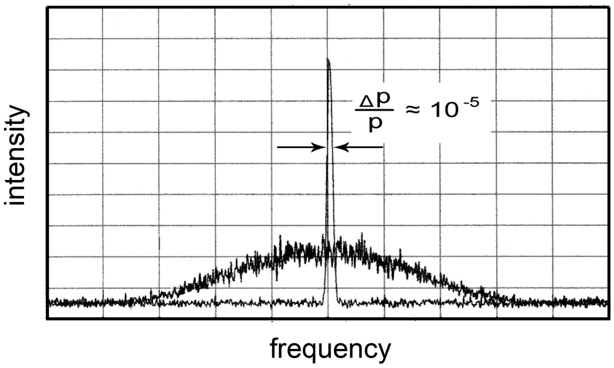

Figure 5.5: Schottky frequency spectra for a circulating beam of U^{92+} ions at 295MeV/u. The broad distribution refers to the uncooled initial beam, measured directly after injection into the ESR. The narrow distribution reflects the momentum profile of a continuously cooled ion beam.

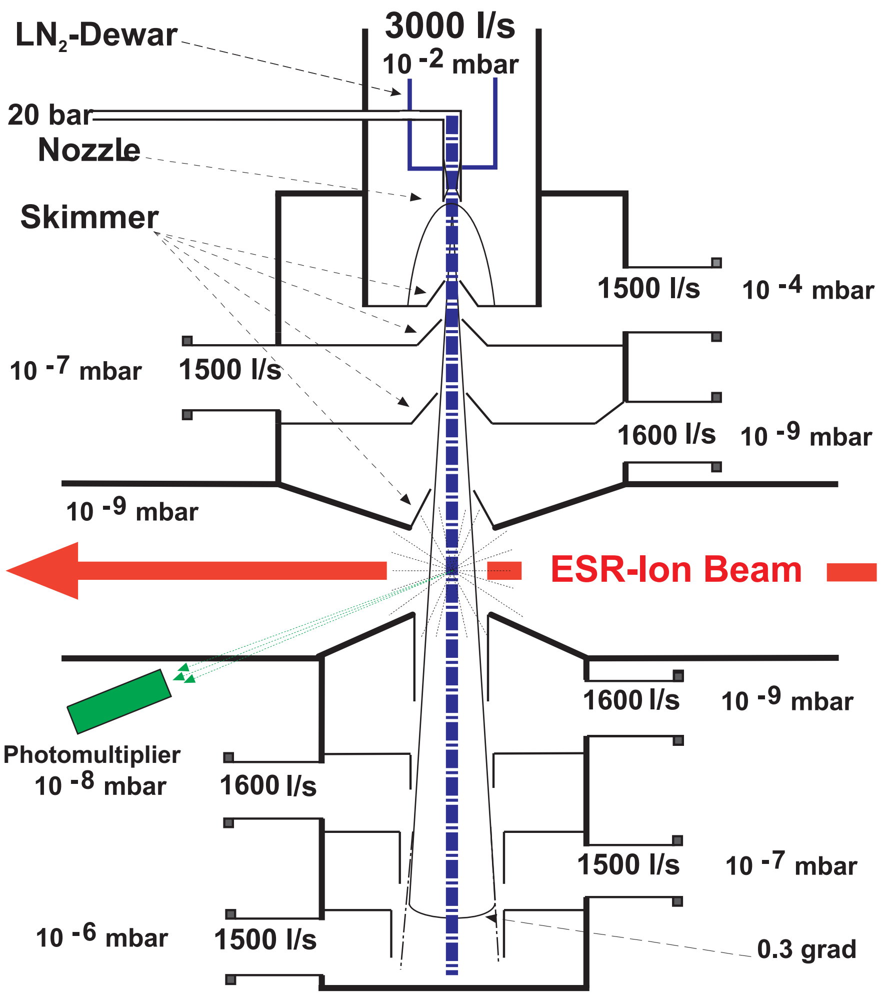
LN₂-Dewar
3000 l/s
10 -2 mbar
20 bar
Nozzle
Skimmer
1500 l/s
10 -4 mbar
10 -7 mbar
1500 l/s
1600 l/s
10 -9 mbar
10 -9 mbar
ESR-Ion Beam
1600 l/s
10 -9 mbar
Photomultiplier
10 -8 mbar
1600 l/s
1500 l/s
10 -7 mbar
10 -6 mbar
1500 l/s
0.3 grad

Figure 5.6: Scheme of the Gas Jet target at the ESR[100].

ions can be stored. For uranium, up to 10^8 ions can be stored routinely. This number is still below the maximum. The limit is set by the space charge potential of the stored ion beam, and restricts the number of stored bare uranium ions at 556 MeV/u to 9.3×10^9, and at 50 MeV/u to 4.4×10^8 [96, 97].

5.3 The Gas-jet target at the ESR

Figure 5.6 shows a schematic of the gas jet [100]. The jet is produced by expanding a gas through a *de Laval* nozzle of 0.1 mm in diameter. To meet the ultra-high vacuum (UHV) requirements of the ESR ($\approx 10^{-11}$ mbar), the actual setup consists of an injection and a dump part, both separated by skimmers and four stages of differential pumping. The present target concept can be described as *the creation of a supersonic jet with a large number of well-defined small clusters* [100]. For a detailed description of the target setup and the design, we refer to [100] and [101].

The typical gas jet target density is about 10^{12} particle/cm^2 [100]. Target gases currently available are: H_2, N_2, CH_4, Ar, Kr, and Xe. For the expensive noble gases such as krypton or xenon, a recycling system is used. The diameter of the target, which was measured experimentally by scanning the jet profile with low intensity ion beams (and with a small diameter), was about 5 mm at the collision centre.

5.4 X-ray Detectors

There is a large range of detectors available for energy dispersive x-ray spectroscopy. These can be split into three main types:

► Solid state semiconductor

These are usually based on silicon or germanium crystalls. The x-rays enter through a thin beryllium window, and produce electron-hole pairs in the semiconductor region of the detector. The number of electron-hole pairs formed depends on the energy of the incoming x-ray. The higher the x-ray energy, the larger the number of electron hole pairs. In order to pull the electrons to the back of the detector, a high voltage is applied. At the back of the detector the electrons are collectively recorded as a negative pulse. A multi-channel analyzer (or similar electronic module) then counts these pulses, and sorts them according to their amplitudes (which are equivalent to the x-ray energies).

Solid state detectors are typically cooled with liquid nitrogen (LN_2) in order to provide acceptable energy resolution.

In many cases this cooling is also vital for maintaining the correct dopant dispersion throughout the crystal, and heating-up can cause serious damage to the detector. However, new generations of high-purity detectors remove these concerns, and allow the detectors to be repeatedly temperature cycled as required – cooling is only required during operation (when the high voltage is applied).

Operating High Voltage	-2500 V
Crystal Length	13 mm
Crystal Diameter	16 mm
Inactive Germanium	0.3 μm
End Cap to Crystal	7 mm
Beryllium Window	0.127 mm
Energy Resolution (FWHM)	195 eV @ 5.9 keV and 495 eV @ 122 keV

Table 5.1: The parameters of the high-purity germanium x-ray detector (ORTEC) used in the experiment.

▶ Silicon drift detectors

These are also based on a silicon detection element, but the design is somewhat different from the typical solid state detector discussed above. Concentric electrodes are placed on the back surface of the silicon, which are used to steadily pull the electrons (arising from x-ray absorption) towards the centre of the crystal. As before, the electrons are collected as a negative pulse, and counted by a multi-channel analyzer (or similar electronic module).

With a silicon drift detector, a very good energy resolution can be obtained, solely with Peltier cooling (typically down to -20 to -30 °C). In addition, multiple-incident x-rays can be detected sequentially, since electrons formed by x-ray absorption in different regions of the detector will have different drift times to the anode. As a result, much higher count rates can be tolerated.

In contrast to the solid state detectors, silicon drift detectors show relatively poor sensitivity for high-energy x-rays.

★ **The 35° detector.**

For the experiment described in this thesis, a planar high-purity germanium semiconductor detector (HPGe) was used for the detection of photons. It was placed closed to the collision centre under 35° with respect to the ion beam direction (see Fig. 5.8). The primary advantage of semiconductors compare to other detectors is the small average energy needed to create electron-hole pairs. For the same radiation energy, the number of electron-hole pairs created (in a semiconductor) is almost one order of magnitude greater than in gases [110]. The germa-

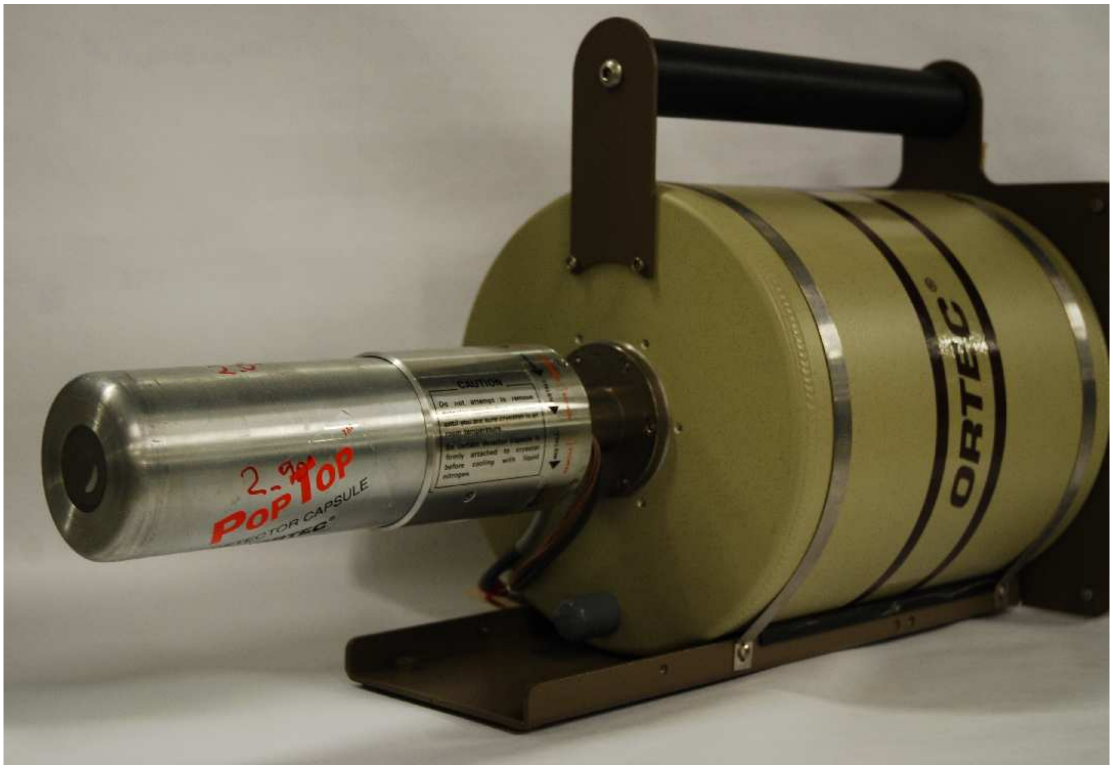

Figure 5.7: The high-purity germanium x-ray detector (ORTEC) used in the experiment.

nium semiconductor detectors are the most commonly used for a registration of the x-ray spectra. However, the spectrum obtained with a germanium detector is an absorption spectrum since germanium is efficient as a photon absorber. In general, the germanium detector, similar to other semiconductor detectors, is a large reverse-biased (p-n junction) diode. At the junction between p- and n-type material, the migration of electrons from the n-type material, and holes from the the p-type material, gives rise to a region of net zero charge. This region is the depletion region. The net positive charge on one side of the junction, and the net negative charge on the other side, sets up an electric field gradient across the depletion region. Any photon interacting with the germanium crystal through any process like Compton scattering, Photoelectric effect, Pair production etc., will produce electron-hole pairs in the depletion region, which will then be swept to the edges of the detector because of the electric field gradient, constituting an electric current. The photon energy required to create an electron-hole pair in germanium is approximately 3 eV, thus an incident photon, with an energy of several tens of keV, produces a large number of such pairs, leading to a very good detection efficiency and low statistical fluctuations. The major characteristics of the germanium detector used in the experiment are listed in the table 5.1.

The germanium detector is usually operated at a temperature of about 77 K, in order to reduce noise from electrons that may be thermally excited across the small band gap in Ge (0.67 eV) at room temperature. This is achieved through thermal contact of the Ge crystal with a dewar of liquid nitrogen. Photons entering the detector firstly traverse the 0.127 mm thick beryllium entrance window of the detector. The attenuation caused by the beryllium window is estimated to be very small, and can be neglected according to

$$\frac{I(x)}{I_0} = exp(-\mu x) \tag{5.1}$$

where I_0 is the incident beam intensity, $I(x)$ is the outgoing beam intensity, μ is the mass attenuation coefficient ($\mu = 0.30176\ cm^{-1}$ for beryllium at 40 keV), and x is the thickness of absorber ($x = 1.27 \times 10^{-3}$) cm for the beryllium window. In general, beryllium windows of the mentioned thickness are considered to be nearly 100% transparent for photons energies above 5 keV.

5.5 Experiments at the ESR

The gas jet experimental chamber is especially designed to study X-ray emission at different observation angles. The accessible angles are 4°, 35°, 60°, 90°, 120°, and 150°, [102], see figure 5.8 for comparison [103]. All detectors are separated from the UHV system of the ESR, either by 50 μm thick stainless steel (4°, 60°, and 120°) flanges at the setup, or by 100 μm thick Be windows (35°, 90°, and 150°). The basic principle of charge-exchange experiments at the ESR gas-jet target is depicted in figure 5.8. After electron capture or ionization, the ions are deflected by a dipole magnet towards the particle detectors. For this purpose Multi-Wire Proportional Counters (MWPC) are used, which allow one to accurately measure the position of the up- or down-charged ions on the detector [99] with a detection efficiency of almost 100%. Time coincidences between events registered by the x-ray detector and by one of the particle detectors are measured in order to extract the x-rays associated with ionization or capture.

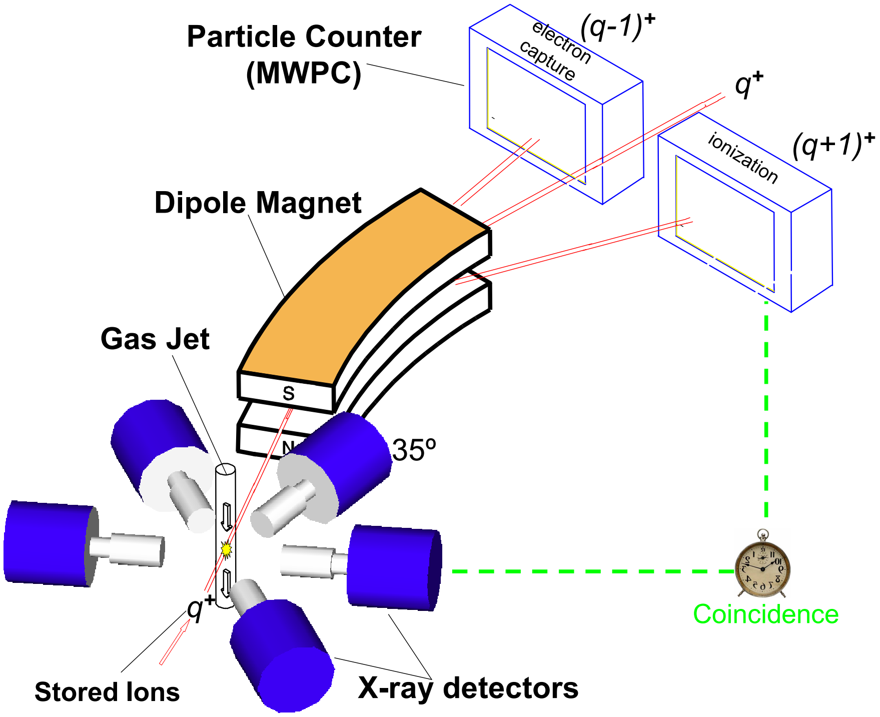
Particle Counter (MWPC)
electron capture
$(q-1)^+$
q^+
ionization
$(q+1)^+$
Dipole Magnet
Gas Jet
S
N
35°
q^+
Coincidence
Stored Ions
X-ray detectors

Figure 5.8: Principle of charge-exchange experiments at the internal gas jet target of the ESR, illustrated for the case of stored q^+ ions. The primary beam of stored ions (with charge-state Q) crosses a perpendicularly oriented molecular or atomic supersonic gas jet. The dipole magnet serves as a magnetic spectrometer. Also shown are the particle detectors for electron capture, i.e. $q^+ \rightarrow (q-1)^+$, and for ionization, i.e. $q^+ \rightarrow (q+1)^+$.

Chapter 6

Feasibility of the Exclusive Production of the K-shell vacancy

6.1 Selective ionization of the K-shell electron of Li-like Uranium

For the experiment, uranium ions with energies of 98 MeV/u and 398 MeV/u were provided by the SIS synchrotron. In order to produce Li-like ions from the 398 MeV/u beam, the primary ions penetrated a 10 mg/cm^2-thick carbon stripper foil. This thickness is well below the equilibrium thickness. For the production of Li-like ions from the 98 MeV/u beam a standard copper foil with a thickness of 50 mg/cm^2 was used. With these methods, about 30% of the initial beam ended up in the Li-like state. After passing through the foil, the ions were analyzed by their charge to mass ratio with a dipole magnet and transferred to the ESR. Typically, 10^8 ions were stored and electron cooled in the ring. For the purpose of cooling, the ESR electron cooler (see figure 5.4) was operated with electron currents in the range between 100 mA and 200 mA. As a result, a beam emittance better than 0.1 π mm mrad, and a momentum spread smaller than $\Delta p/p \leq 10^{-4}$ were achieved. After the initial cooling, the supersonic gas-jet target (see figure 5.6) of the ring was switched on, producing a well-collimated beam (5 mm in diameter) of neutral nitrogen molecules that perpendicularly crosses the ion beam trajectory. The area density of the target amounts up to 10^{12} particles/cm^2. A schematic of the experimental target area of the ESR is depicted in figure 5.8.

After passing through the target area, the projectiles which lost (Q=90+) or captured (Q=88+) one electron were separated from the primary beam by next bending magnet of the ring. Both, the up- and down-charged uranium ions were registered by position-sensitive particle detectors (see section 5.5)

The x-rays emitted from the beam-target interaction area were detected by planar Ge(i) detectors surrounding the gas-jet target at observation angles close to 10°, 35°, 60°, 90°, 120° and 150° with respect to the beam axis (see 5.5). All detectors were equipped with a combination of lead/cupper collimators in order to reduce the Doppler broadening to values below 1 keV. In general, these collimators defined the solid angle of the individual detectors to a value close to 3×10^{-4} of 4π, each. Finally, all x-ray detectors were energy and efficiency calibrated using ^{182}Ta, ^{133}Ba, and ^{241}Am radiation sources.

Standard NIM/CAMAC/VME modules were used in the experiment for data acquisition. X-ray and particle detector events, supplied by the various detectors, were recorded independently *event-by-event*. In addition, all detectors were connected to fast scalers in order to correct for possible electronic dead-time effects. The time signals of the x-ray detectors served as a trigger and no hardware coincident event selection was used. This resulted in typical event rate of 1 to 2 kHz. Coincidences were reconstructed from the listmode data by an analysis of the time information provided by the TDC modules used for every detector. Depending on the x-ray detector, the typical time resolution achieved for x-ray/particle coincidences was in the range between 20 and 50 ns. The trigger technique applied enabled us also to register x-ray emission in coincidence and anti-coincidence with projectile charge exchange.

Sample x-ray spectra recorded at the particular angle of 35°, for 98 MeV/u and 398 MeV/u $U^{89+} \rightarrow N_2$ collisions, are shown in figure 6.1 and 6.2, respectively. The spectra refer to the laboratory frame and are not corrected for detector efficiency. In fig. 6.1(a) and 6.2(a) the single x-ray spectra are displayed, i.e. all x-rays, regardless of their origin (excitation, ionization, or capture), are contained

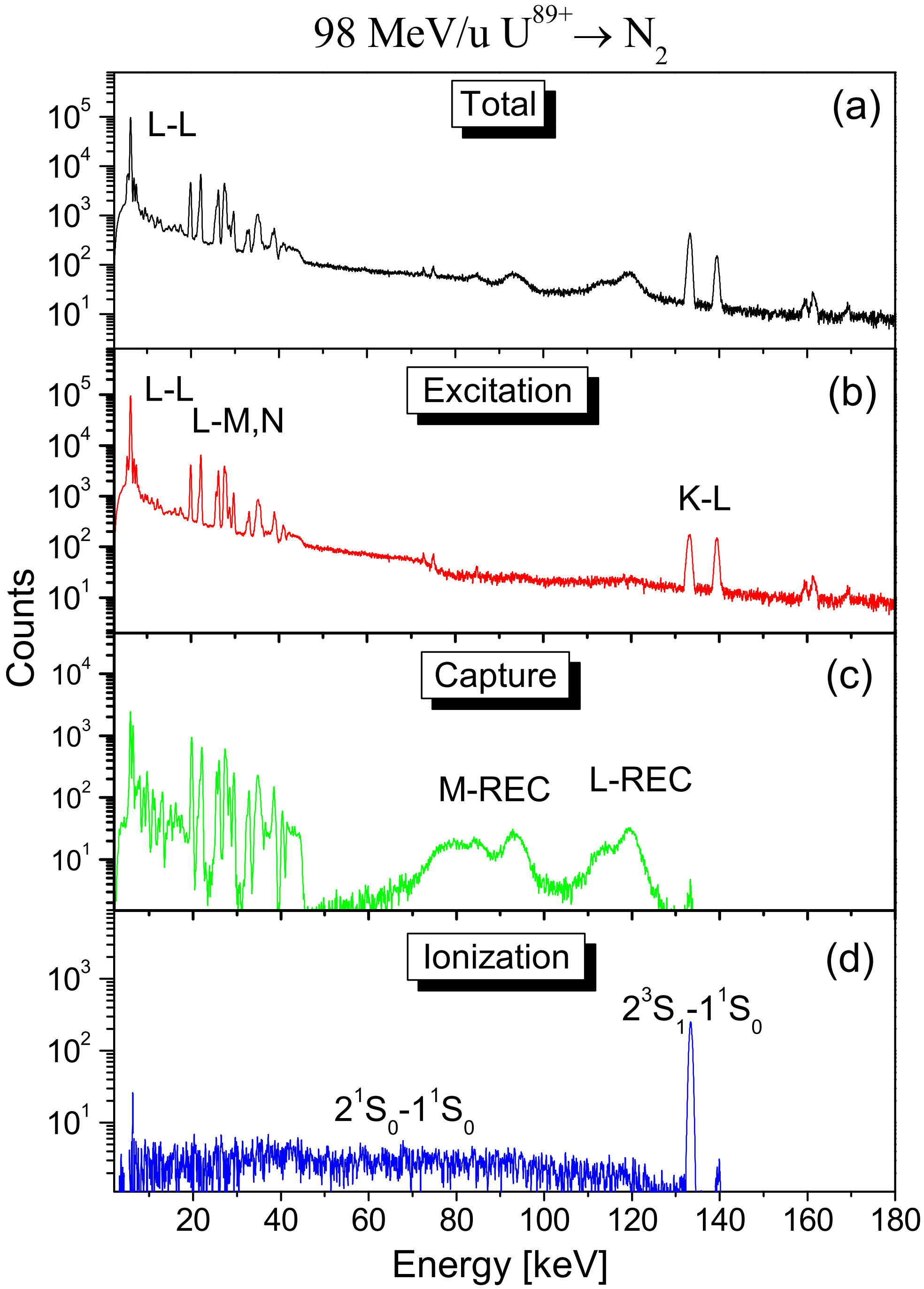

Figure 6.1: Projectile x-ray spectra for 98 MeV/u $U^{89+} \rightarrow N_2$ collisions measured (a) without coincidence requirement (total emission spectrum), (b) with excitation coincidence (U^{89+} charge), (c) with capture coincidence (U^{88+} charge), (d) with ionization coincidence (U^{90+} charge). All spectra were recorded at an observation angle of $\theta=35^o$. Energies correspond to the laboratory frame.

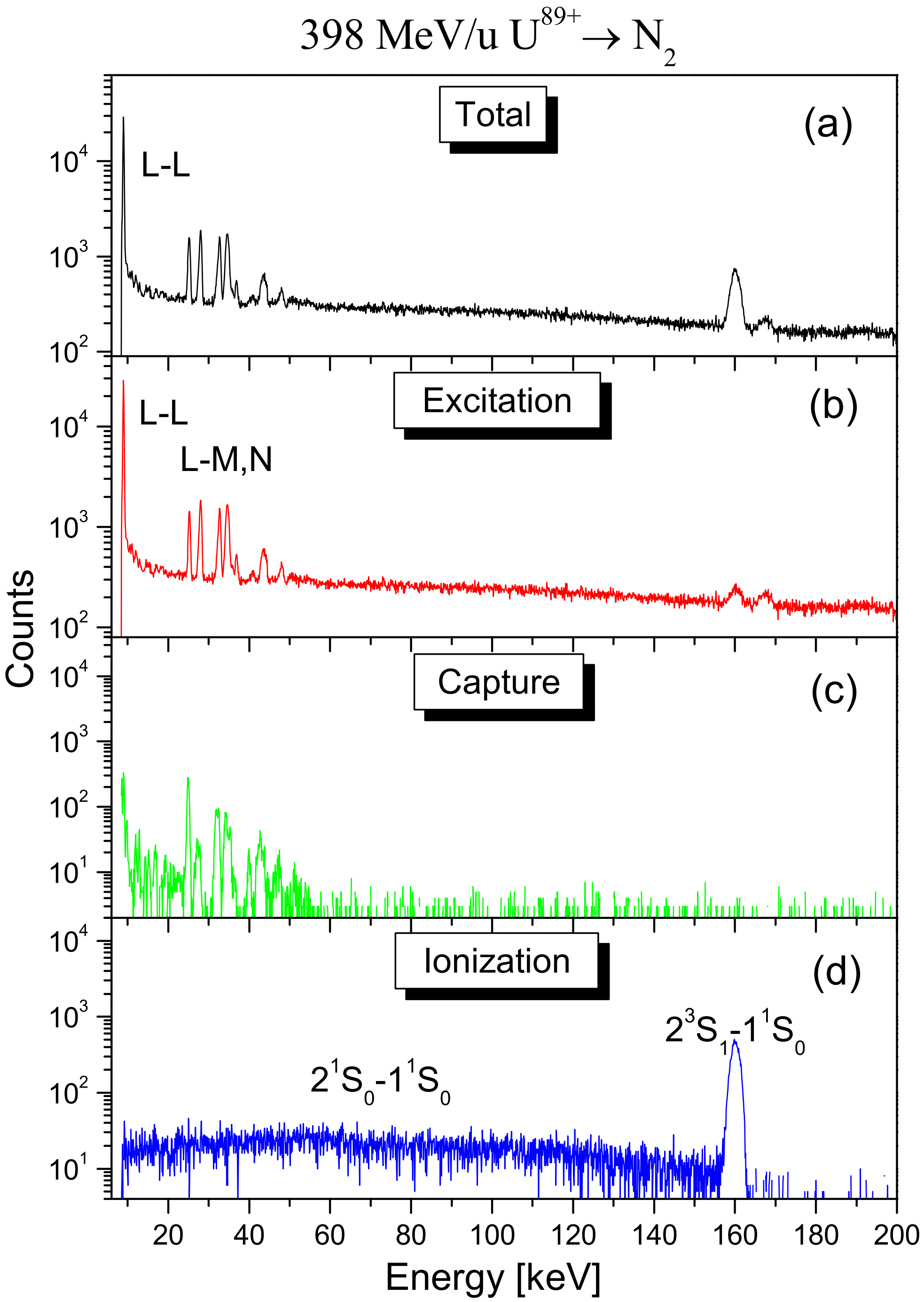

Figure 6.2: Projectile x-ray spectra for 398 MeV/u U^{89+} → N$_2$ collisions measured (a) without coincidence requirement (total emission spectrum), (b) with excitation coincidence (U^{89+} charge), (c) with capture coincidence (U^{88+} charge), (d) with ionization coincidence (U^{90+} charge). All spectra were recorded at an observation angle of θ=35^o. Energies correspond to the laboratory frame.

within these spectra. In order to disentangle between the various collision processes leading to projectile x-ray emission, the coincidence time information was used. In figure 6.1(c) and 6.2(c) the corresponding spectra associated with electron capture (outgoing charge state of U^{88+}) are shown, containing in particular strong x-ray transition lines in the low energy region (Balmer lines). In the mid energy region of figure 6.1(c), the observed radiation is dominated by radiative electron capture (REC) into the L and higher shells of the projectile. Please note that due to the blocked K-shell, no $K\alpha, K\beta, ...$ emission is visible within this spectrum. The L- and M-REC lines for the higher collision energy are not visible (figure 6.2(c)) because their energies (∼400 keV) are out of the presented energy range. Part (d) of figure 6.1 and 6.2 shows the corresponding spectra associated with electron loss, e.i. ionization, (coincidence with ions of charge state of 90+). It can clearly be seen that these spectra are entirely dominated by a single $K\alpha$ ground state transition and a broad continuum. For completeness, part (b) of figure 6.1 and 6.2 shows the spectra recorded in anti-coincidence with events related to projectile charge exchange. These spectra result from the subtraction of the spectra recorded in coincidence with projectile charge exchange from the total spectrum, i.e. (b) = (a) - (c) - (d). These anti-coincident spectra are dominated by x-ray transitions produced by excitation of the L-shell or K-shell only. Also strong continuous radiation due to electron Bremsstrahlung is clearly visible. From the spectra (b) we learn that the $2s \rightarrow 2p$ excitation (L - L) is the most dominant process for the collision system under discussion.

However, the most remarkable aspect of the presented spectra is the simple structure of the photon emission associated with ionization of the initial Li-like projectile (fig. (d)). Obviously, and in contrast to the excitation spectrum, only one $K\alpha$ transition, the $K\alpha_2$ line, shows up in addition to the broad continuum ranging from basically 0 keV up to the $K\alpha$, reaching its maximum in the middle part (see fig. 6.2d). This continuum is caused by the $2E1$ decay of the $[1s2s]\ ^1S_0$ state in He-like uranium, whereas the intense $K\alpha_2$ results from the $M1$ decay of the $[1s2s]\ ^3S_1$ level.

Therefore, K-shell ionization of Li-like high-Z ions has been found to be a highly selective mechanism for the production of n=2 S-states. The maximum probability for the simultaneous $2s \rightarrow 2p$ excitation and $1s$ ionization in the charge exchange (electron loss) processes can be estimated as 5×10^{-4} and 8×10^{-5} for 98-MeV/u and 398-MeV/u collision energies, respectively. As it was shown in chapter 4, this selectivity in the production of the n=2 S-states in the K-shell ionization stays undisturbed by the following rearrangement processes. This highly selective mechanism in relativistic ion-atom collisions gives a unique opportunity to obtain perfect conditions for studying exotic transitions in high-Z highly charged ions. For the particular case of He-like ions, the properties of two-photon decay of the $[1s2s]\ ^1S_0$-state can therefore be studied in great detail in background-free measurements.

6.2 Selective ionization of the K-shell electron of Be-like Uranium

The developed approach was also used for initially Be-like ions aiming on exclusive population of the $1s2s^2$ state in Li-like ions. This state is expected to undergo predominantly an exotic two-electron one-photon decay (TEOP) (see fig. 6.3). In turn the sensitivity of the TEOP transition to electron correlation provides a new access for detailed investigations of the interplay of relativistic and correlation effects on the atomic structure of few electron systems. Therefore selective production of the initial $1s2s^2$ state of Li-like ion would provide clean conditions for the investigation of the exotic TEOP transition.

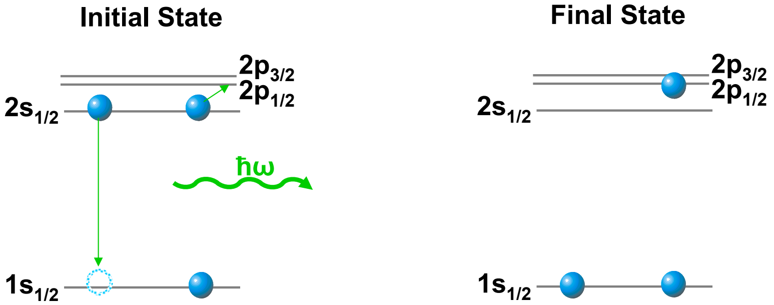

Figure 6.3: Schematic of two-electron one-photon transition ($1s2s^2 \rightarrow 1s2s2p_{1/2}$).

The experiment was performed at the experimental storage ring ESR at GSI-Darmstadt (see chapter 5). For the experiment, uranium ions with an energy of

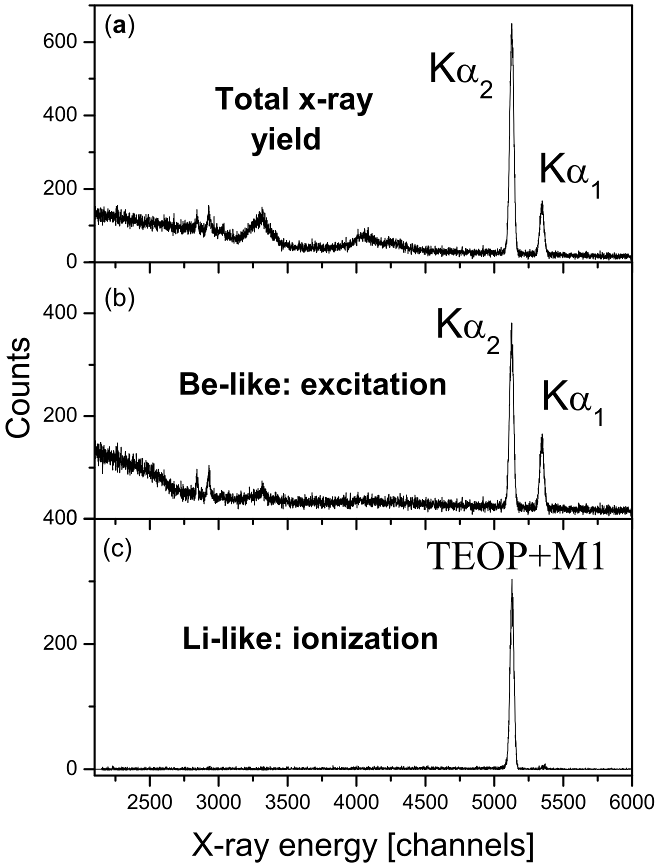

Figure 6.4: Projectile x-ray spectra for 90 MeV/u $U^{88+} \rightarrow N_2$ collisions measured (a) without coincidence requirement (total emission spectrum), (b) with excitation coincidence (U^{88+} charge), (c) with ionization coincidence (U^{89+} charge). All spectra were recorded at an observation angle of θ=35^o.

90 MeV/u were provided by the SIS synchrotron. After acceleration to the final energy, the Be-like charge state was produced by using a thin carbon stripper foil, with a thickness much below the equilibrium thickness, which allowed us to achieve a high production yield for Be-like ions. Behind the foil the beam was magnetically analyzed, and the fraction of U^{88+} ions was transferred into the ESR storage ring. Typically, 10^8 ions were stored and electron cooled in the ring. For the purpose of cooling, the ESR electron-cooler was operated with electron currents in the range between 100 mA and 200 mA. After the cooling cycle, the accumulated ions, forming a beam with a full width at half maximum of about 2 mm, were colliding with a supersonic nitrogen gas-jet target with a typical area

density of about 10^{12} particles/cm^2. The beam energy-loss, caused by the interaction of the beam with the target atoms, was compensated by the continuous electron cooling. The x-rays following the collisions of the ions with the target, were registered by an array of germanium detectors covering observation angles from 0° to 150° with respect to the ion beam direction. After passing trough the target area, the projectiles that lost or captured one electron were registered after the next bending magnet of the ring with an efficiency close to 100%. Up- and down-charged uranium ions were detected by two position sensitive particle detectors (Multi-Wire Proportional Counters) located at the inner and outer side of the ring, respectively. The time signals of the x-ray detectors served as a trigger and no hardware coincident event selection was used. By an analysis of the time information, this trigger technique allowed reconstruction of those x-rays that were coincident or anti-coincident with projectile charge exchange from the list mode data. In Fig. 6.4, we present preliminary x-ray spectra recorded at an observation angle of 35°. By the timing technique applied, the x-rays associated with K-shell excitation (no projectile charge exchange, anti-coincidence) are disentangled from events where x-rays are produced by K-shell ionization (coincidence with up-charged projectiles).

As can be seen in Fig. 6.4, K-shell ionization again appears to be a very selective population process (compare the results for He-like ions in the previous section). In the associated photon spectrum only one single x-ray line is observed, which stems from the decay of the $1s(2s)^2$ state. One has to point out that, in contrast to low-Z ions, this state may also decay by a fast $M1$ transition.

Chapter 7

Measurement of the two-photon decay in He-like tin and the data evaluation

The experiment aimed for a measurement of the spectral shape of the two-photon decay, and was performed in August 2006 at the experimental storage ring. The measurement was based on the experimental technique discussed in chapter 4. For this purpose, the experimental setup at the gas target was exploited (see fugure 5.8).

7.1 The Experiment

In the experiment tin (Z=50, A=114) ions were used (7.1). After stripping behind the UNILAC, and choosing the desired Li-like (Sn^{47+}) charge state, the ions were injected in the SIS and accelerated up to an energy of 300 MeV/u. The beam was then injected into the ESR, and cooled by the electron cooler (current=250 mA, voltage=164,550 kV) to achieve a well-defined constant velocity of $\Delta\beta/\beta \approx 10^{-5}$, as well as a reduced emittance. The accumulated ion current in the ESR, after cooling, was about 800 μA. In order to exclude data that might have been influenced by the complicated beam-handling procedures during injection and cooling, there were no x-ray spectra recorded during the beam accumulation periods. Only after the completion of a whole cycle, the gas-jet was switched on

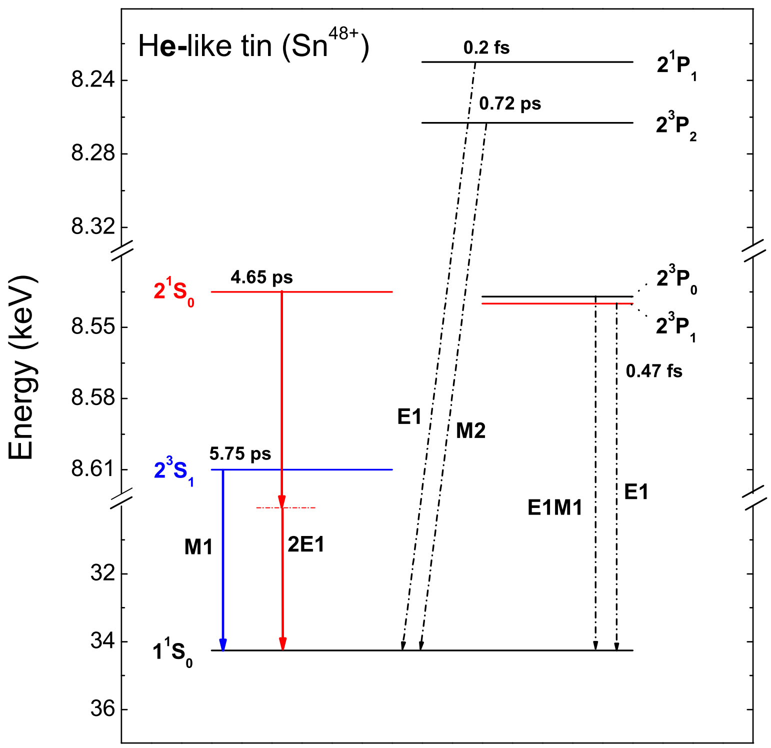
He-like tin (Sn^{48+})
Energy (keV)
8.24
8.28
8.32
8.55
8.58
8.61
32
34
36
0.2 fs
2^1P_1
0.72 ps
2^3P_2
4.65 ps
2^1S_0
2^3P_0
2^3P_1
0.47 fs
E1
M2
5.75 ps
2^3S_1
E1M1
E1
M1
2E1
1^1S_0

Figure 7.1: Energy level scheme for He-like tin. The vertical axis represents the binding energy, the numbers above the levels correspond to the lifetimes.

Initial State	Decay Mode	Transition Rate (s^{-1})	Transition Energy (eV)
2^1S_0	2E1	2.15(11)	25712
2^3S_1	M1	1.74(11)	25637
2^3P_0	E1M1	1.37(9)	25720
2^3P_1	E1	2.12(15)	25707
2^1P_1	E1	5.08(15)	26016
2^3P_2	M2	1.38(12)	25983

Table 7.1: Decay modes, ground state transition energies, and rates for the $n = 2$ states of He-like tin (Sn^{48+}) ions [119, 62, 120, 61]. The numbers in brackets denote the power of 10.

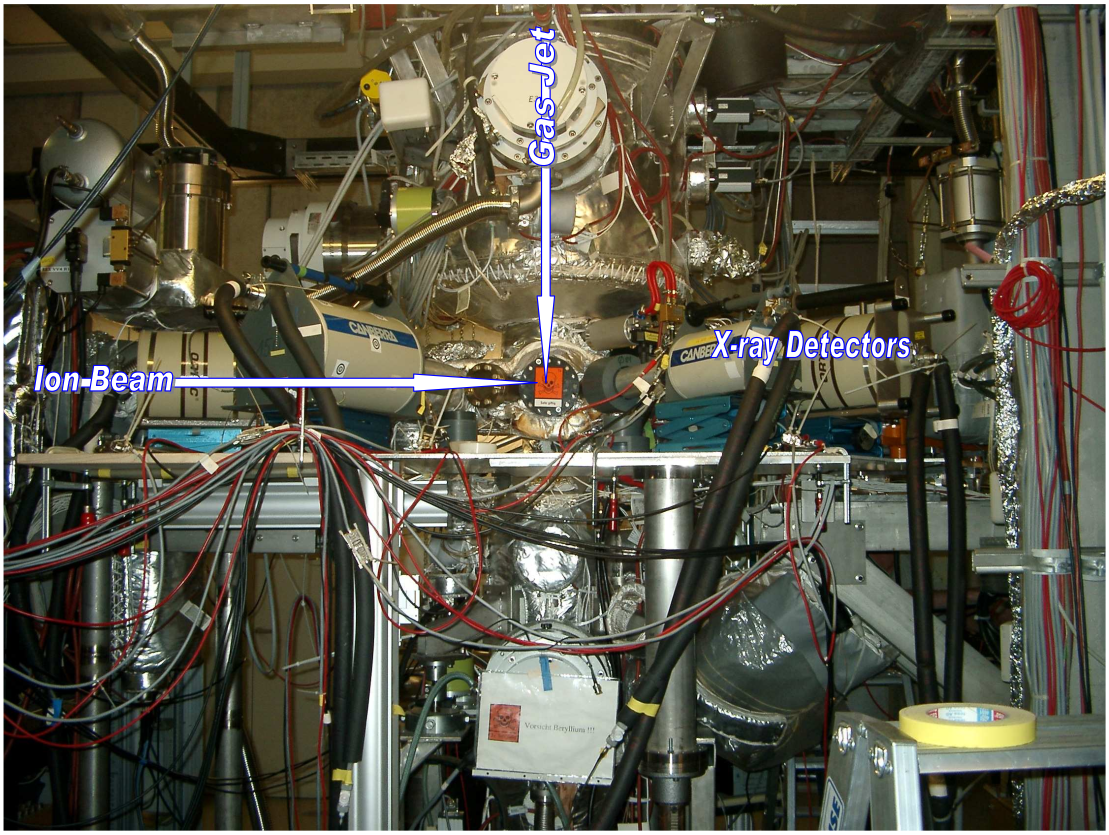

Figure 7.2: X-ray detectors at the gas-jet target of the ESR. The 35° detector is the one on the far right.

and the measurement was started. As a target nitrogen gas [106] was used with a density of 2×10^{12} particle/cm^3. The measuring cycle was defined mainly by the charge-exchange cross sections of the ions interacting with the gas-jet. The x-rays produced in the ion-atom collisions were registered by a planar Ge detector placed at an angle of 35° with respect to the ion beam direction (see figure 7.2). The detector was separated from the ultra-high vacuum ($\sim 10^{-11}$ mbar) of the interaction chamber by a 100 μm beryllium window. A 4-mm wide copper-lead slit was mounted in front of the detector in order to reduce the Doppler broadening. After the interaction, the up-charged projectile ions were separated by the dipole magnet, and registered by a multi-wire particle detector. Energy and efficiency calibration of the detector were carried out carefully, before and after the experiment, using calibrated thin ^{57}Co, ^{133}Ba and ^{241}Am radioisotopes.

7.2 Total x-ray spectrum

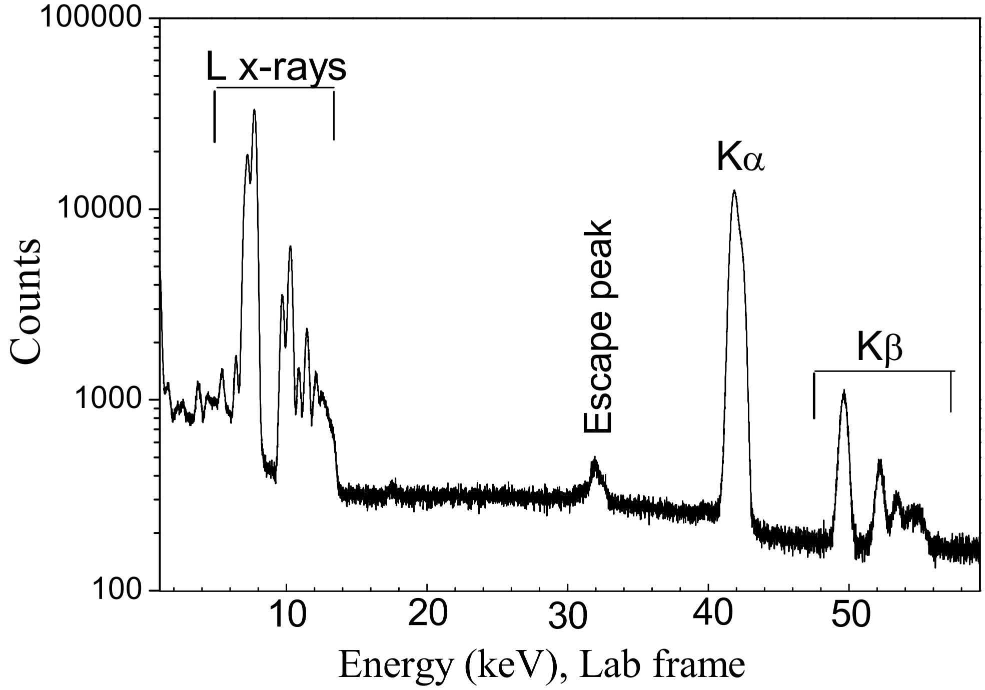

Figure 7.3: Total (raw) x-ray spectrum from 300 MeV/u $Sn^{47+} \rightarrow N_2$ collisions, measured at an angle of 35°.

The total x-ray emission spectrum (without coincidence requirement) is presented in figure 7.3. The spectrum represents all registered x-rays associated with radiative processes. Most x-rays stem from the interaction of the projectiles with the gas-jet target, but also fluorescence from the surrounding materials can be observed. Starting from the right, the spectrum shows the $K\beta$ and $K\alpha$ transition lines, the two escape peaks from the germanium crystal appear in the middle, and some resolved lines of L-transitions along with the fluorescence from the slits of the detector dominate the low energy side. Already in the total spectrum the broad continuum, starting from almost zero energy up to the $M1$-peak, associated with the two-photon decay can be identified.

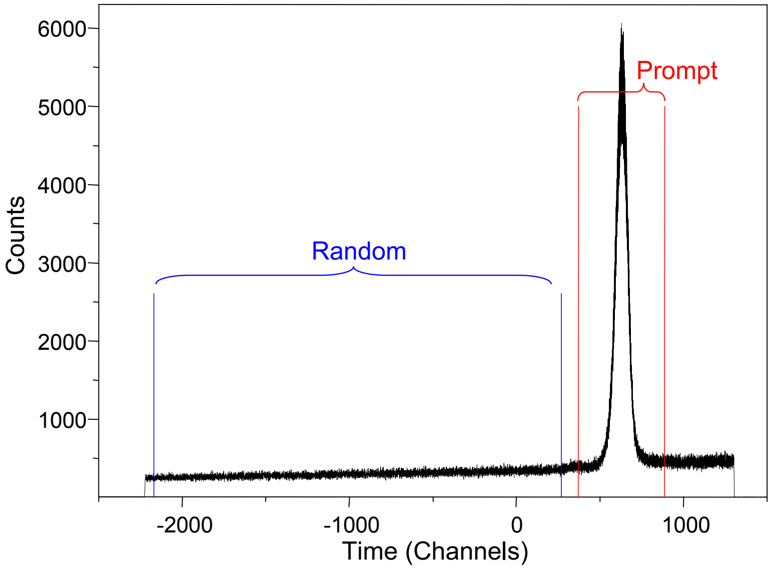

Figure 7.4: Time spectrum, showing the 'prompt' and 'random' intervals. The time is obtained from the difference between the registered x-ray and particle events.

7.3 Random subtraction

As described in chapter 5.5, the experiment implied the detection of the x-rays and of the up-charged ions, along with the corresponding timing. The time coincidence information was then used to select the events associated with projectile ionization. The spectrum of the difference in time between the x-rays and the particles is shown in figure 7.4. One can see a pronounced peak of 'prompt' events, which corresponds to x-rays registered in coincidence with particles. Since the experimental data were recorded in an *event-by-event* mode, it is possible to select only ionization events by extracting the prompt events from the corresponding time spectrum. The x-ray spectrum associated with the prompt events is depicted in figure 7.5b. However, the prompt peak is contaminated with 'random' events, which form a slope on the broad time range (see fig. 7.4). The x-ray spectrum associated with the random events is shown in figure 7.5c. In order to separate the 'random' events from the 'prompt' ones, a linearly fit to the data was made. This allowed us to estimate the amount of random events in the prompted area. Finally, the whole procedure lead to the extraction of only those events that could be associated with projectile ionization (see fig. 7.5d). Even though the intense L x-rays from the projectile and fluorescence photons from the surrounding material contaminate the spectrum in the low energy region below 10 keV (see fig. 7.5d), as will be discussed later, the low energy half won't be used for the analysis of the two-photon distribution.

7.4 Ionization spectrum

The true ionization (coincidence) spectrum, presented in figure 7.5d, shows the broad continuum, from the two-photon decay of $1s2s\ {}^1S_0$ state [111] and an intense monoenergetic line from the magnetic dipole $M1$ transition from the decaying $1s2s\ {}^3S_1$ state. Additional lines, e.g. from the decay of the $2\ {}^1P_1$ (electric dipole transition) and $2\ {}^3P_2$ (magnetic quadruple transition) states have not been observed. This fact indicates that the present collision system leads to selective K-shell ionization of Li-like tin, and subsequent exclusive formation of the $1s2s\ {}^1S_0$ and the $1s2s\ {}^3S_1$ states of He-like tin. The high level of selectivity for K-shell ionization of Li-like uranium ions in relativistic collisions with nitrogen has already been discussed in chapter 4. Since the $2s$ electron stays almost passive during the collision, the measured $M1$ line, and especially the $2E1$ energy distribution, are not contaminated by decays from the $2\ {}^3P_0$ ($E1M1$) or $2\ {}^3P_1$ ($E1$) states. The decay of the $2\ {}^3S_1$ state to the ground state via $2E1$ (apart from $M1$) transition, which also has continuum shape, can contaminate the $2E1$ spectrum from the $2\ {}^1S_0$ state. The calculated branching ratio is 10^{-4} for the $2E1$ to $M1$ transition from the $2\ {}^3S_1$ state. From the total counts in the observed $M1$ peak, the contribution of $2E1$ decay of the $2\ {}^3S_1$ state is several parts per thousand compared to the counts in the $2E1$ continuum from the decay of $2\ {}^1S_0$ state. This means that decay from the $2\ {}^3S_1$ state can be neglected for the final result.

Since the spectral distribution of the two-photon decay is symmetric with respect to its middle point, one may take either of the halves of the distribution for the further analysis. In the present measurement, the higher energy part has several clear advantages. First of all, the higher part of the measured spectrum lies in the energy range between 20 keV and 50 keV, where the efficiency of the detector is close to 100%. This can clearly be seen from Fig. 7.9 and 7.10. Therefore,

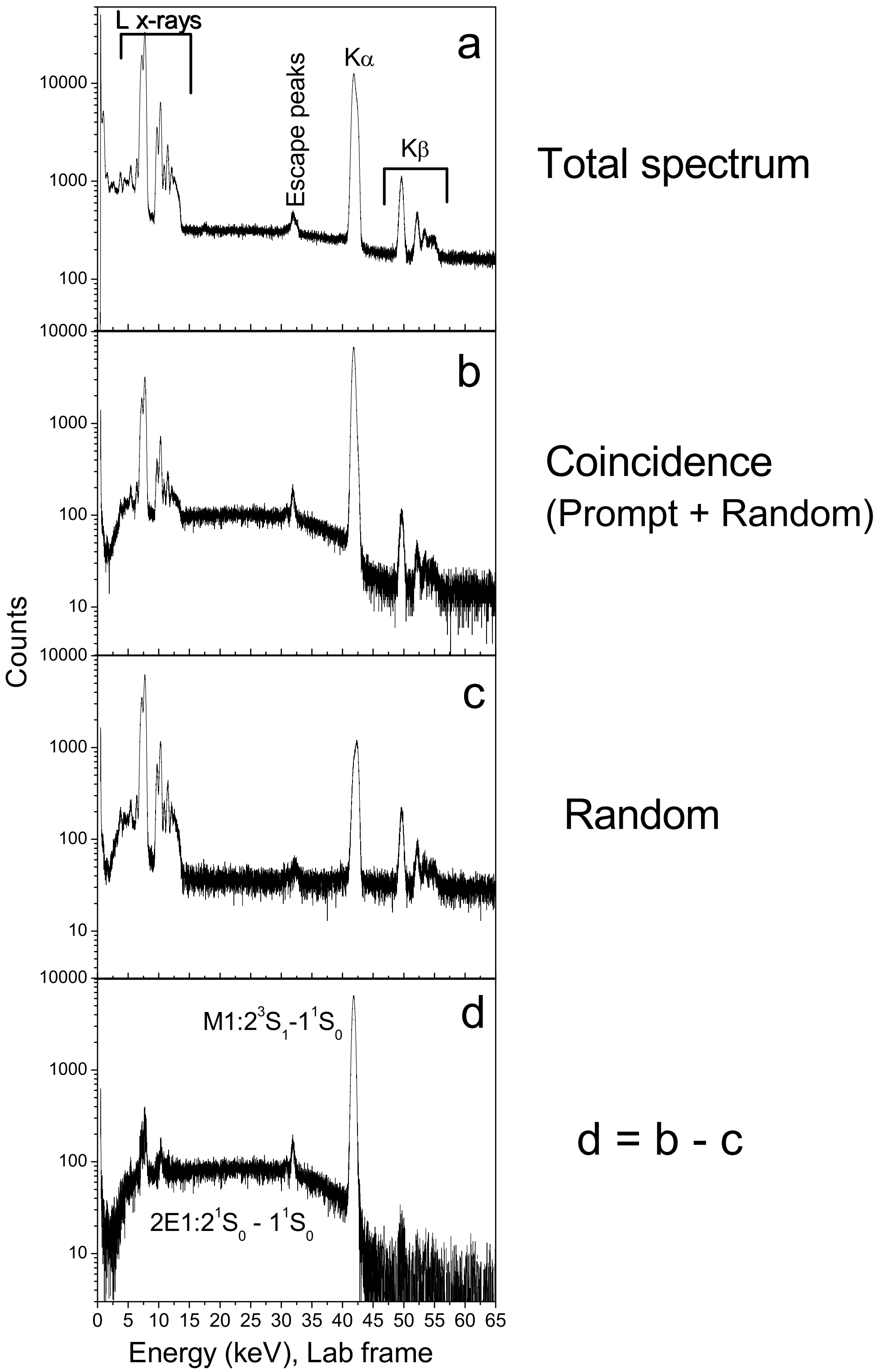

Figure 7.5: X-ray spectra of 300 MeV/u $Sn^{47+} \rightarrow N_2$ collisions measured at an angle of 35°, (a) without coincidence (total x-ray spectrum), (b) in coincidence with ionization including random events, (c) in anti-coincidence - random and (d) in coincidence with ionization without random events (Sn^{48+}).

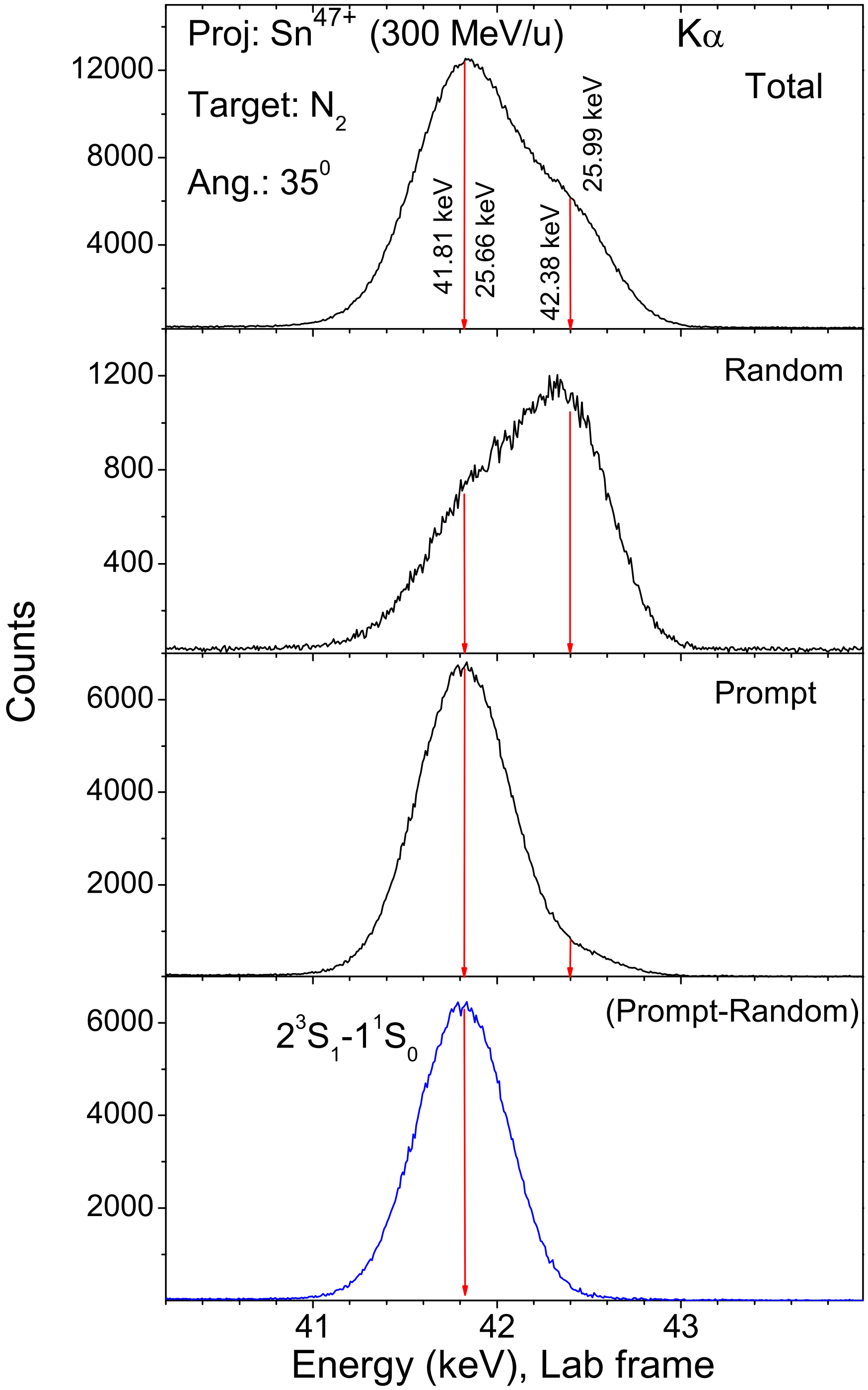

Figure 7.6: Zoom of the energy region around the K_α and $M1$ peaks. The top panel clearly shows the two peaks, which energies are labelled both for the laboratory and the emitter frame. The bottom panel shows the pure $M1$ peak, obtained by proper timing conditions.

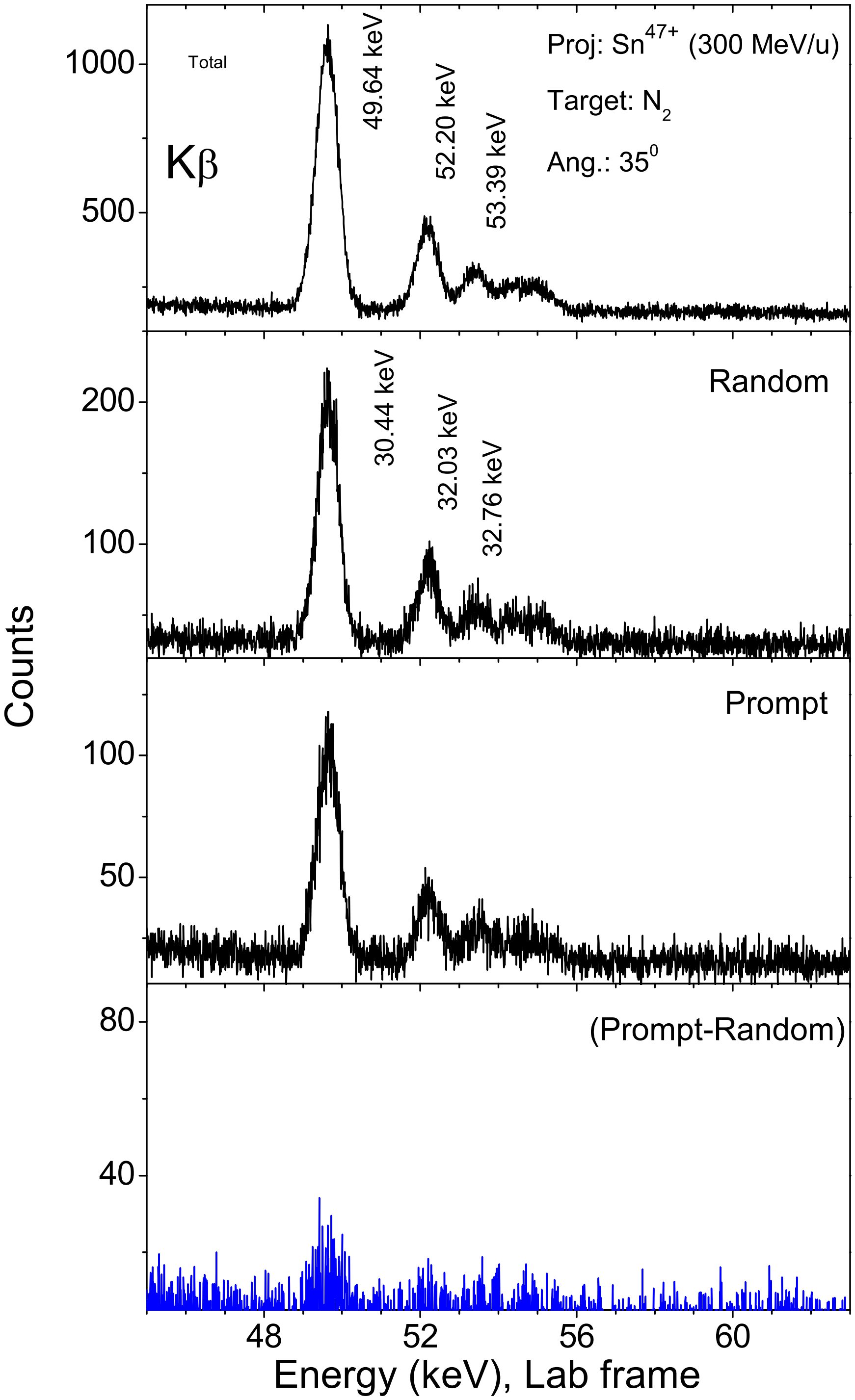

Figure 7.7: The K_β peaks with different time conditions. The x-ray energies given apply to the laboratory frame. The top panel shows the total spectrum, the lower panel the spectrum with timing conditions (ionization).

the corresponding corrections won't significantly affect the distribution. Also, the higher energy part is not contaminated by any radiation not related to ionization of the projectile (e.g. fluorescence), and the only contribution to the two-photon shape is due to the $M1$ transition.

7.5 Energy and Efficiency calibration

The Ge(i) detector was calibrated with a radioactive americium (^{241}Am) source before and after the experiment. The source has a half-life of 432.7 years and decays into neptunium (^{237}Np) through the emission of alpha particles and low energy gamma rays (59.54 keV). In the resulting spectrum, shown in Fig. 7.8, we recognize the two americium spectral lines (X_1, X_2), and the x-ray lines (X_3-X_6). The radiation type, energy and relative intensity of the lines X_1...X_6 are listed in table 7.2). The energy values are taken from [107, 108], while relative probabilities are taken from [109].

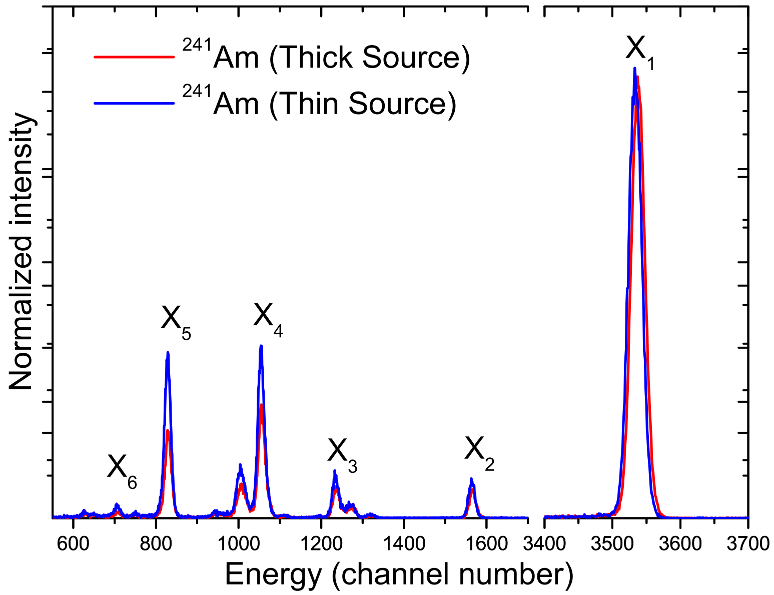

Figure 7.8: The x-ray spectrum from the ^{241}Am-source, as it was taken for the energy and efficiency calibration of the detector. The energy scale is given in channels, and the intensity is normalized to the amplitude of the X_1 peak (59,54 keV). The colors of the spectra denote measurements performed with a thick (red) and a thin (blue) source.

Peak Label	Radiation type	Energy (keV)	Relative intensity(%)
X_1	γ	59.54	35.7
X_2	γ	26.4	2.4
X_3	$Np\ L_\gamma$	20.8	4.93
X_4	$Np\ L_\beta$	17.8	19.3
X_5	$Np\ L_\alpha$	13.9	13.3
X_6	$Np\ L_l$	11.9	0.86

Table 7.2: The radiative lines of the ^{241}Am-source used for the energy calibration of the detector.

Please note, the difference between spectra taken with a thick (1 mm) and a thin (10 μm) source. Due to a higher self-absorption of the thick source, the detector registered less low-energy photons as compared to the thin source.

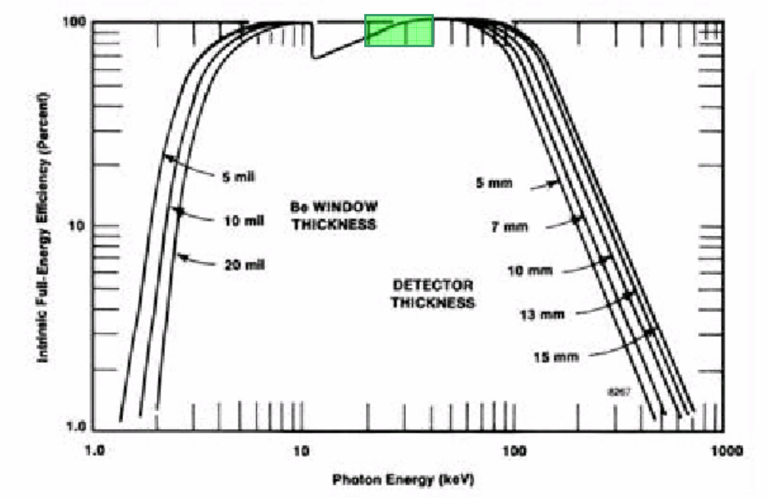

Figure 7.9: Relative efficiency of the germanium detector (13 mm thick), as provided by the supplier. The energy range of importance for the two-photon spectral shape measurements is marked (20-40 keV).

In figure 7.9 the relative efficiency of the germanium detector is shown, as provided by the supplier. The energy range of importance for the two-photon spectral shape measurements is also marked (see figure 7.9). According to the

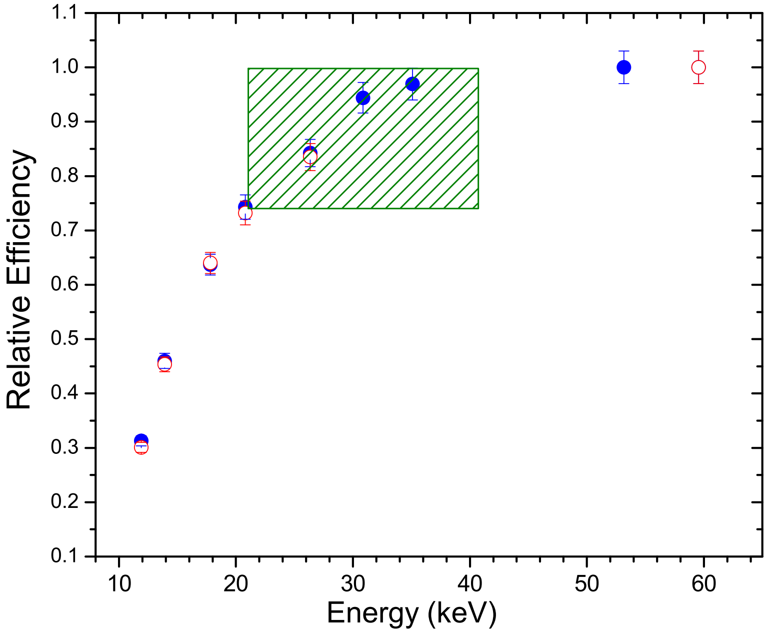

Figure 7.10: Measured relative efficiency of the germanium detector (13 mm thick). The red (hollow) and blue (full) circles denote the measurements with and without slit, correspondingly. The energy range of importance for the two-photon spectral shape measurements is marked.

supplier, the efficiency in the mentioned energy range is 80-100%. Therefore, only negligible efficiency corrections of the measured two-photon spectra are required. Hence, experimental uncertainties due to the efficiency of the detector are minimized.

In addition, relative efficiency measurements were also performed after the experiment, in the same environment. The measurements were performed with and without the copper-lead slit (used in the experiment), in order to test the slit's influence on the measurement. Within the error bars of the efficiency measurements, no influence of the slit on the photon detection efficiency was found.

7.6 Spectra simulations

As can clearly be seen from Fig. 7.5d, the high-energy part of two-photon spectral shape is exclusively blended by x-rays from the $M1$-transition. Therefore, a precise and truthful estimation of this contribution is one of the crucial points in the data analysis. This procedure is usually done by simulating the main effects of x-ray detection by a computer code.

7.6.1 Relativistic Doppler shift

In order to compare the measured energy spectrum of a fast moving source with its theoretical prediction, the x-ray spectrum observed in the laboratory system has to be transformed into the rest frame of the ion. Since the 300 MeV/u projectile was moving at 65% of the speed of light, the energies of the emitted photons, measured in the laboratory frame, have to be corrected for the relativistic Doppler shift [121]:

$$E_\gamma^{emit} = E_\gamma^{lab} \cdot \gamma \cdot (1 - \beta cos\theta_{lab}), \tag{7.1}$$

where E_γ^{emit} and E_γ^{lab} are the photon energies in the emitter and the laboratory systems, respectively; θ_{lab} denotes the laboratory observation angle, β is the speed of the ion in units of the speed of light, and γ is the relativistic Lorentz factor:

$$\gamma = \frac{1}{\sqrt{1-\beta^2}}, \ \beta = \frac{v}{c}. \tag{7.2}$$

According to equation (7.1), the energy in the emitter frame depends on the observation angle in the laboratory system and on the β-value of the projectile. The observation angle of the detector was 35°, and the β-value was determined from the cooler voltage, since the velocity of the cooling electrons defines the velocity of the stored ions. The cooler voltage (U_e) can be expressed as follows

$$eU_e = (\gamma - 1)mc^2 \tag{7.3}$$

In equation 7.3, e is the charge of electron and mc^2 is its rest mass. The value U_e represents the voltage of the high-voltage generator, corrected by the potential depression due to the space charge of the electron beam, and by the small work function of the cathode.

Thus, the measured energy of the $M1$ peak in the coincidence spectrum (see 7.6), after the transformation, is 25650 eV. This is in good agreement with the predicted value of the $2\ ^3S_1 \rightarrow 1\ ^1S_0$-transition energy in He-like tin (see table 7.1).

7.6.2 Doppler broadening of the x-ray lines

The detector was placed under 35° (with an uncertainty of 1°), but 390 mm away from the projectile-target interaction region. The gas target has a diameter of 5 mm. A 4 mm-wide slit was placed front of it. This causes an additional uncertainty in the observation angle. This corresponding energy uncertainty can be derived from equation (7.1):

$$\Delta E_{\gamma}^{lab} = \frac{E_{\gamma}^{lab}\beta sin\theta_{lab}}{1-\beta cos\theta_{lab}}\Delta\theta_{lab}. \tag{7.4}$$

where E_{γ}^{lab} was defined earlier (see equation 7.1), and $\Delta\theta$ is the opening angle uncertainty.

7.6.3 Detector Response

The influence of the detector response function on the measured distribution also has to be estimated. In the high-energy regime, where Compton scattering in the detector becomes non-negligible, the detector response needs to be known, in order to correctly identify all the spectral lines. Due to the escape peaks of the germanium crystal of the detector, the $M1$ photon could be detected as two low-energy photons. This would, of course, modify the shape of the two-photon energy distribution.

The response function of the germanium detector was simulated with the EGS4 code [122], including the LSCAT package [123],[124]. In the simulation, the photoelectric effect, the Compton effect for bound electrons, Rayleigh scattering, as well as L- and K-shell fluorescence were considered. The geometry model contained a point-like source, which represented the ion beam-gas target interaction point, two beryllium windows (ESR beamline port and the detector entrance), and the planar cylindrical germanium crystal (sensitive volume of the detector). The dimensions and distances represented those of the experimental setup.

In order to estimate the effect of the Doppler broadening of the spectral lines, in particular that of the $M1$-peak, simulations with the *spec*-code were performed. The corresponding parameters of the experimental setup, listed in table (7.3), were used as input data for the programs.

Projectile's Atomic Number(Z)	50
Target's Atomic Number(Z)	7
Target Width	5 mm
Beam Energy	300 MeV/u
Transition Energy	25 647 eV
Transition Natural Width	5.7×10^{-5} eV
Detector to Source Distance	390 mm
Detector Angle	35°
Detector Width	4 mm
Detector Height	16 mm
Detector Resolution	348 eV
Number of Channels	8064
Energy Range	0-80 keV

Table 7.3: Input data for the EGS4 simulation of the detector response, and for the *spec*-code for a calculation of the Doppler broadening of the line.

The simulation results were convoluted with the energy-dependent resolution of the detector, and corrected for the Doppler broadening due to the finite opening angle of the detector. As discussed earlier, the resolution as a function of energy was obtained by measurements of the mono-energetic lines from the following radioactive sources: ^{57}Co, ^{133}Ba, ^{152}Eu, ^{207}Bi, and ^{241}Am. The obtained energy resolution was 390 eV for 60 keV photons, and 520 eV for 120 keV radiation. The Doppler broadening was calculated according to eq. (7.4). The angle uncertainty $\Delta\theta$, calculated according to the experimental detector/chamber geometry (given in the table 7.3), was of the order of 1 degree, leading to a Doppler broadening of about 1 keV for the 60 keV line. As a consequence, the line width used in the simulation was mainly determined by the Doppler broadening (see 7.11). The simulated detector response for the $M1$ line, convoluted with the theoretical two-photon distribution, agrees well with the measured $2E1$ photon distribution. The spectrum shown in Fig. 8.1 clearly demonstrates this good agreement. Small discrepancies are only observed for the region close to the $M1$ line. These are probably a result of the low-energy asymmetry of the $M1$ line. Figure 7.11 shows

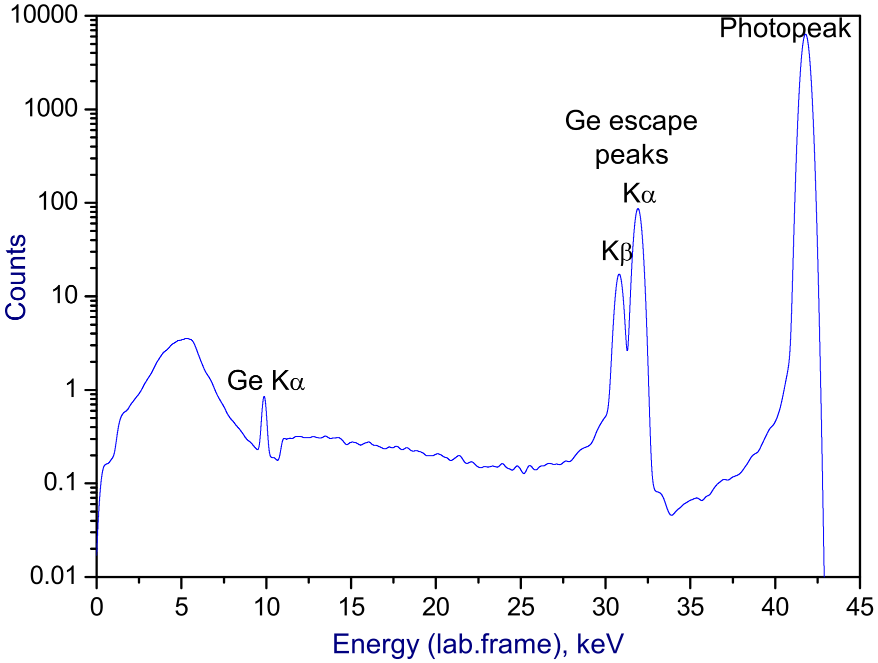

Figure 7.11: The detector response function for the $M1$ transition.

that corrections for the $M1$ line response function are only important for the low-energy side of the two-photon spectrum. This region is also very sensitive to absorption in the view ports. However, for the further data analysis only the high-energy half of the two-photon distribution will be considered.

Chapter 8

Results and Discussions

In order to compare the theoretical and the measured two-photon spectral shapes, both distributions were normalized to the maximum energy of the $2E1$-transition, thus energy difference between 2 $^1S_0$- and 1 $^1S_0$-levels.

Since the 'first' photon with energy $\hbar\omega_1$ cannot be distinguished *a priori* from the second one, the photon distribution is expected to be symmetrical around half the transition energy, which is given by E$_i$ - E$_f$ $= \hbar\omega$. $\hbar\omega$ is the total transition energy and E$_i$ and E$_f$ are the energy of initial and final electron states. The two photons get an equal share of energy ,$f = \hbar\omega_1\hbar\omega_2/(\hbar\omega_1+\hbar\omega_2)$, where $\hbar\omega_1+\hbar\omega_2 = \hbar\omega$; $\hbar\omega_1$ or $\hbar\omega_2$ is the energy of either of the photon.

Therefore, for the further analysis one can consider either of the *halves* of the spectral distribution (see Fig. 3.8). Since the detector efficiency is better for higher photon energies, and there are no further contamination in this region, we consider in the following always the 'upper half' of the spectral distribution, $f \geq 0.5$. For this part, only the lower tail of the intense $M1$ line might affect the end of the $2E1$ spectrum with, say, $f > 0.90$. Therefore, as described earlier (see previous chapter) the response function of the Ge detector was simulated.In the simulation, different photon-atom collision processes in the Ge crystal and the geometrical parameters were considered. The simulation results (bottom part of Fig. 8.1) have then been convoluted with the energy dependent resolution of the detector and the Doppler broadening due to the finite opening angle of the detector. The detector simulations reproduce the measured position and intensity of the Ge K escape peaks very well compared to the $M1$ line intensity (Fig. 8.1).

The low-energy tail of the $M1$ peak extends up to around $f = 0.92$ (38.6 keV photon energy in the lab frame), and the Ge K escape peak rides on the $2E1$ spectral distribution from $f = 0.68$ - 0.78 (28.5 - 32.7 keV photon energy in the lab frame) (region II in Fig. 8.1).

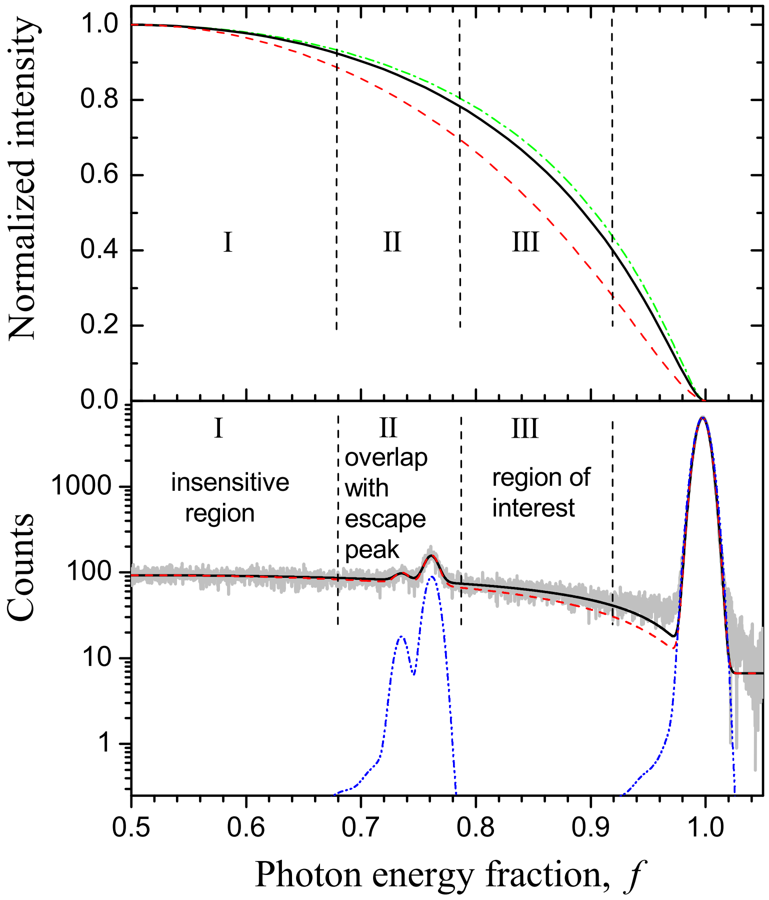

Figure 8.1: Top part: Higher energy half of the fully relativistic calculated two-photon energy distribution (the intensity is normalized to 1 at f=0.5) for He-like Ni (dash-doted line), Sn (solid line) and U (dashed line). Vertical dashed lines show the different regions of the spectral shape. Bottom part: Comparison between the higher energy half of the measured two-photon spectral distribution of He-like tin (solid light-gray line), and a fully relativistic calculation for He-like Sn (solid line) and U (dashed line) together with the simulated detector response function for the $M1$ line (dotted line).

The observed spectral distribution of the photons is compared with fully relativistic computations that are based on a dual-kinetic-balance finite basis set method [125] in order to perform the summation over the complete Dirac spec-

Z	Experiment	Theory		
	He-like	Relativistic^1	Relativistic^2	Non-relativistic
28	-	0.403	0.418	0.416
50	0.390±0.003	0.386	0.396	0.422
60	-	0.374	0.381	0.423
70	-	0.366	0.367	0.424
92	-	0.324	0.329	0.425

Table 8.1: Intensity ratio R="I3/I1" (bottom part of Fig. 8.1) for the observed $2E1$ spectral distribution of He-like Sn^{48+} ions, compared with theoretical values for different ions along the helium isoelectronic sequence (^{1}with electron-electron correlations included; ^{2}without electron-electron correlations).

trum. In these computations, the interelectronic interaction has been taken into account by means of an effective screening potential. To compare the $2E1$ spectral distribution of (helium-like) ions with different charge Z, the distributions were normalized for $f = 0.50$ (see Fig. 8.1). For the FWHM of the $2E1$ distribution, the theory predicts a reduction of 14% in going from Ni ($Z = 20$) to U ($Z = 92$). This is indicated by region III, defined as, $f = 0.80$ - 0.90, in the upper part of Fig. 8.1. Within the 'region of interest', the advantage is that we have a clean two photon decay spectrum. Outside this region, i.e. for $f = 0.50$ - 0.80 and $f = 0.9$ - 1.0, the $2E1$ distribution behaves very similarly for the differentions (Fig. 8.1). Region I ($f = 0.50$ - 0.68) is insensitive to (changes in) Z. A direct check of the shape difference can be made by comparing the integrals of region I and III via their ratio R="I3/I1" (see table 8.1). The measured ratio is found to be in agreement with the theoretical ratio for He-like Sn. Furthermore, the measured spectral shape was compared with the theoretical one using the MINUIT minimization code [126], which requires the best agreement (minimum χ^2) between the theoretical and the measured distributions. The result of this comparison is presented in Fig. 8.2, where the fraction (Exp-Theory)/Theory is plotted versus f, for different Z. In the insensitive region, the shapes cannot be distinguished, while the difference is clearly visible in the sensitive region ($f =$ 0.80 - 0.90). The Sn data points come within $\pm 3\sigma$ of the average values, whereas

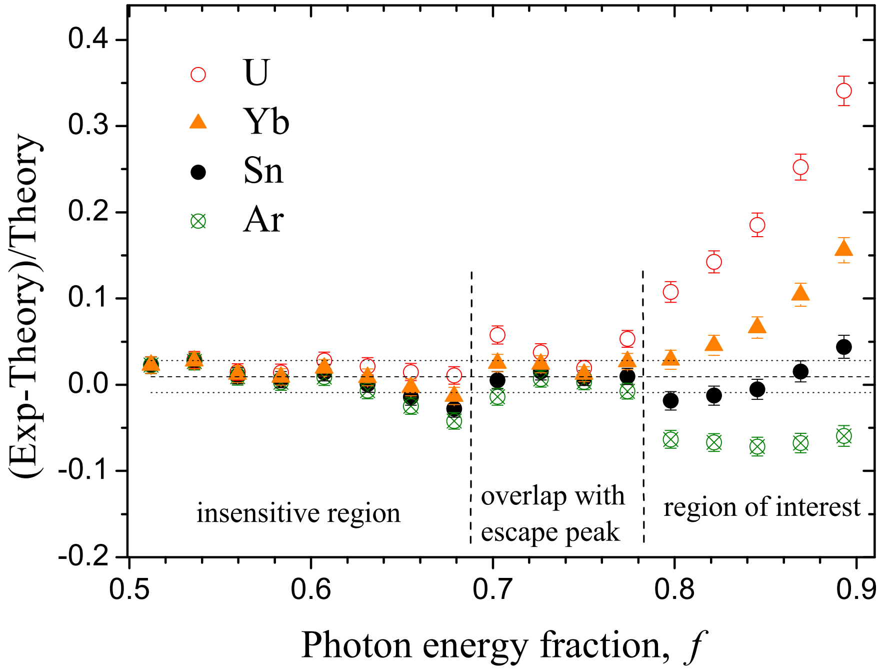

Figure 8.2: (Exp-Theory)/Theory intensity ratio with theoretical values for Ar, Sn, Yb and U as a function of the photon energy fraction. Each point corresponds to bin of 1000 eV energy region. Data has been plotted up to f =0.92, where the low-energy tail of the $M1$ peak does not contribute. Horizontal dotted lines are the mean value and ± 3σ value in case of Sn.

the U data points start deviating from 0.80 and depart up to several 10 σ at $f = 0.90$. This deviation is due to the relativistic effects, which make the $2E1$ spectrum for Yb and U substantially narrower than that of Sn.

The developed coincidence technique allowed us to substantially reduce the amount of background radiation. The total spectrum (no coincidences) comprises all x-rays from the projectile ions, including those resulting from excitation, ionization or electron capture, as well as from the detected electron bremsstrahlung. The x-ray continuum in the total spectrum not only stems from the $2E1$-decay, but also from the bremsstrahlung [127, 128, 145] that arises from target electrons that interact with the projectile's Coulomb potential. The continuum associated with the primary bremsstrahlung is distributed over the whole range of the two-photon decay in the total spectrum, up to the energy $E_{max} = (\gamma - 1)mc^2\gamma^{-1}(1 - \beta cos\Theta)^{-1} \approx 268$ keV, where β is the projectile velocity in units of the speed of light, $\gamma = (1 - \beta^2)^{1/2}$, mc^2 is the electron rest mass in keV, and Θ is the observation angle in the laboratory frame. However, since the bremsstrahlung is not correlated to electron ionization, it was possible to disentangle the two-photon decay x-rays from the bremsstrahlung photons by using the time coincidence information between the x-rays and the up-charged Sn^{48+} ions (ionization). Besides the bremsstrahlung radiation the coincidence technique substantially reduces other time-uncorrelated background radiation, such as cosmic rays.

In conclusion, our approach allows for a new kind of measurement of the energy distribution of the two-photon decay. The achieved sensitivity to the $2E1$ spectral shape allowed for measurements that confirmed, for the first time, the fully relativistic calculations. The future experiments will be devoted to studies of angular and polarization correlations in the two-photon decay.

Chapter 9

Summary

A novel experimental approach for studying exotic transitions in few-electron high-Z ions was developed. In this approach, few-electron ions with selectively produced single K-shell holes are used for the investigation of the transition modes that follow the decay of the excited ions. The feasibility of the developed approach was confirmed by an experimental study of the production of low-lying excited states in He-like uranium, produced by K-shell ionization of initially Li-like species. It was found that K-shell ionization is a very selective process that leads to the production of only two excited states, namely the $1s2s\ 2^1S_0$ and $1s2s\ 2^3S_1$. This high level of selectivity stays undisturbed by the rearrangement processes. These experimental findings can be explained using perturbation theory and an independent-particle model, and are a result of the very different impact parameter dependencies of K-shell ionization and L- intrashell excitation. The L-shell electron can be assumed to stay passive in the collision, whereas the K-shell electron is ionized.

It was stressed that the current result might directly be applied to accurate studies of the two-photon decay in He-like ions. Up to now, the experimental challenge in conventional $2E1$ experiments has been the photon-photon coincidence technique, which is required to separate the true $2E1$ events from the x-ray background associated with single photon transitions. In contrast, by exploiting K-shell ionization, the spectral distribution of the two-photon decay could be obtained simply by a measurement of the photon emission, using only a single x-ray detector in coincidence with projectile ionization. One further particular advantage arises from the fact that the $1s2p\ ^3P_0$ state is not populated, and does not contribute to the continuum distribution of the two-photon emission. At high Z, this state also undergoes a two-photon $E1M1$ decay, which would be indistinguishable from the $2E1$ decay of the $1s2s\ ^1S_0$.

The first measurement of the two-photon energy distribution from the decay of $1s2s\ ^1S_0$ level in He-like tin was performed by adopting the technique developed in this thesis. In this technique, excited He-like heavy ions were formed by K-shell ionization of initially Li-like species in collisions with a low-Z gas target, and x-ray spectra following the decay of the He-like ions were measured in coincidence with the up-charged tin ions. The observed intense production of the $2E1$ transitions, and a very high level of selectivity, make this process particularly suited for the study of the two-photon continuum, and thus for a detailed investigation of the structure of high-Z He-like systems. The method allowed for a background-free measurement of the distribution of the two-photon decay ($2^1S_0 \rightarrow 1^1S_0$) in He-like tin. The measured distribution could also be discriminated from that of other He-like ions, and confirmed, for the first time, the fully relativistic calculations.

In addition, the feasibility of the method was confirmed by studying another exotic transition, namely the two-electron one-photon transition (TEOP) in Li-like high-Z ions. An experimental investigation of the radiative decay modes of the $1s2s^2$ state in Li-like heavy ions has been started. In the first dedicated beam time at the ESR, selective population of this state via K-shell ionization of initially Be-like species was achieved. The x-rays produced in this process were measured by a multitude of x-ray detectors, each placed under different observation angles with respect to the ion beam direction. The spectra associated with projectile electron loss consist (in all cases) of one single x-ray transition, which was attributed to the TEOP decay to the $1s^2\ 2p_{1/2}$ level, possibly contaminated by the $M1$ decay to the $1s^22s$. Thus it was proven that, by adopting the developed approach, one can indeed produce the desired initial state. This makes this method perfectly suited for studies of TEOP transitions in high-Z systems. An extension of this study, by the inclusion of an electron spectrometer, would also allow for measurements of the autoionization channel, which would provide complete information on the various decay modes of the $1s2s^2$ state.

Chapter 10

Outlook

The experimental approach developed in this thesis work is perfectly suited for investigations of exotic decay modes in heavy highly-charged ions. Hence, this approach opens up many new perspectives and opportunities for detailed studies of related phenomena in relativistic ion-atom collisions.

The new facility FAIR will also provide an optimal infrastructure for investigations of the exotic transitions using similar spectroscopic techniques and methods. The atomic physics program at FAIR, as planned by the Stored Particles Atomic physics Research Collaboration (SPARC), will focus on two major research themes, fundamental interactions between electrons and heavy nuclei (in particular the interactions described by Quantum Electrodynamics, QED), and collisional dynamics in strong electromagnetic fields. The experimental areas at the new facility will provide a range of novel instrumentation for atomic and applied research.

The NESR [129] will be of particular relevance for the atomic physics program. Compared to all other heavy-ion storage rings, either currently in operation or planned, the NESR will be the most flexible one, providing the most intense beams available, including bare uranium. Moreover, new instrumentation will be available, such as an internal gas jet target with two orders of magnitude higher density (up to $10^{14}\ cm^{-2}$) than the existing one. This new target will have a diameter of only 5 micrometers, which is 1000 times smaller than the existing target. Therefore, uncertainties due to Doppler broadening of the lines will be significantly reduced. Products of interactions with the internal target can be detected by an ensemble of spectrometers including x-ray crystal spectrometers (3-120 keV energy range), low-temperature microcalorimeters (bolometers), Compton polarimeters, an electron spectrometer, and an extended reaction microscope (COLTRIMS) with many of the products being detected with almost 4π acceptance. This facilitates a large range of newexperiments, as well as new tests of high field QED.

10.1 Further Applications: Two-Electron One-Photon transition in Li-like Uranium

The method developed within this thesis can be used in order to study another exotic decay mode in Li-like ions, namely the two-electron one-photon transition (TEOP). Since recent years, the decay properties of the singly excited $1s2s^2$ state in Li-like ions has been the subject of detailed experimental and theoretical investigations [137, 138, 139, 140] (and for a survey see Ref. [141]). The particular feature of this state is the occurrence of an exotic, dipole allowed, two-electron one-photon decay into the $1s^2\ 2p_{1/2}$ and the $1s^2\ 2p_{3/2}$ levels, mediated by configuration interaction. At low Z, the TEOP decay gives only a minor contribution to the total decay rate, which is dominated by the autoionization channel. However, it already contributes significantly to the total decay probability at Z around 30, and is predicted to be the dominant decay channel for the highest nuclear charges such as $Z = 92$. In the latter case, the magnetic dipole radiative decay into the $1s^2\ 2s$ ground state must be considered in addition. Fig. 10.1 shows the various decay modes of the $1s2s^2\ 2S_{1/2}$ state, plotted as a function of the atomic number Z [141]). This strong variation of the decay properties of the $1s2s^2$ state along the isoelectronic sequence is therefore an ideal testing ground for our understanding of the interplay between relativistic and correlation effects in few electron systems. However, up to now the experimental information about this topic is limited to $Z < 50$. The developed approach along with a high resolution detection system, e.g. a crystal spectrometer and/or micro-calorimeter, will be used for studies of the two-electron one-photon transition. In the future, this study will be extended by the inclusion of an electron spectrometer [144, 145].

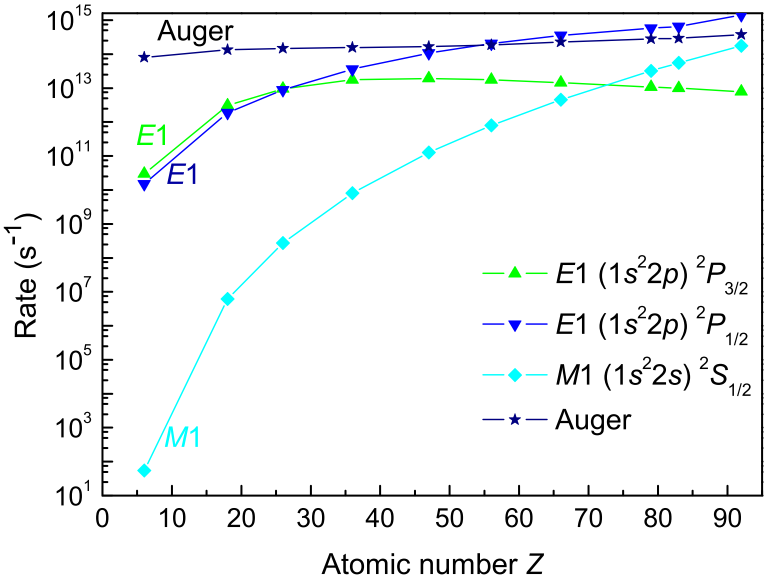

Figure 10.1: Rates for the various decay modes of the $1s2s^2\ 2S_{1/2}$ state plotted as a function of the atomic number Z [141].

This would enable one to also measure the autoionization channel (Auger), and hence provide complete information on the various decay modes for the $1s2s^2$ state.

10.2 Two-Photon Decay in High-Z ions: Further Development and New Challenges

According to the predictions (see chapter 3.1), relativistic effects in the two-photon spectral shape are most pronounced in heavy highly-charged ions. Therefore it would be of particular advantage to perform measurements of the two-photon decay in such systems. The developed approach is a very straight forward method in that respect. Further experiments will be also devoted to the angular correlation and polarization in the two-photon decay of high-Z ions. The contributions of higher order multipoles to the interaction of the ions with the radiation field are expected to cause asymmetries in the photon-photon emission [136, 41](see chapter 3.1). Thus if all multipole interactions are included, the angular distribution deviates from the $1+\cos^2\theta$ form. Thus the photon-photon angular correlation function, which is found to be symmetric with respect to the angle $\theta = 90°$ in the electric dipole approximation, becomes asymmetric because of the nondipole contributions. In particular, there are cosθ- and cos$^3\theta$-dependent terms in the angular distribution, which result from the interference of the multipole transitions. The dominant interference comes from that between the dipole and the quadrupole. Even though the nondipole effects cause slight asymmetry in the angular correlation function, these effects are usually small for most neutral, medium-Z elements and suppressed, in addition, by the screening of the nuclear charge due to electron-electron interaction. However the nondipole contributions and hence the asymmetry effects are enhanced as the nuclear charge Z increases. Hence, with improved precisions in angular distribution measurements, especially for the high-Z highly charged ions it would be interesting to look for this asymmetry.

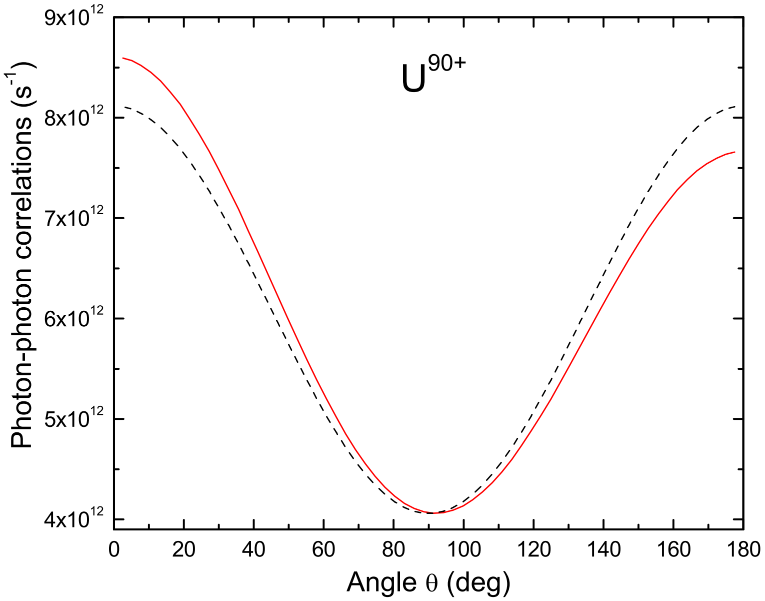

Figure 10.2: Photon-photon angular correlations in the $2^1S_0 \rightarrow 1^1S_0$ two-photon decay of the He-like uranium ion. Results are presented for the relativistic and the non-relativistic calculations for the equal share of the photon energy($f = 0.5$) [63].

Recent interest is also focused on the polarization-resolved analysis of the two-photon emission. In this connection, the polarization entanglement between two photons produced in the decay of metastable hydrogen have been explored in detail in a "back-to-back" emission geometry [132, 133]. Less information is available, however, about the (degree of) polarization entanglement if an arbitrary geometry is considered for collecting the photons. In this respect, an investigation of the effect of the decay geometry on the polarization entanglement between the two simultaneously emitted photons would be of interest [134]. A strong variation in the degree of entanglement is found for different geometries of the photon detection, as well as for different initial populations of the excited ionic states [135].

Even though the developed approach provides an outstanding opportunity to study the two-photon spectral shape by registration of only one photon, for the study of angular distribution and polarization of the photon one has to apply the x-ray-x-ray coincidences. In this respect, several segmented detectors will be used to cover a reasonably large solid angle. In this way one can measure both simultaneously emitted photons, which would allow to measure the angular correlation of the two-photon decay. Furthermore, the polarization of the photons will also be measured with newly developed position sensitive polarimeters. In this respect, the on-going FAIR project will provide optimal conditions for the above mentioned investigations.

Chapter 11

Zusammenfassung

In der vorliegenden Arbeit wurde eine neue experimentelle Methode entwickelt, um exotische, atomare Übergänge in schweren Wenig-Elektronen Systemen zu studieren. Bei dieser Methode werden durch K-Schalenionisation von Wenig-Elektronen-Ionen gezielt angeregte *s*-Zustände in der L-Schale erzeugt, um so deren Zerfallscharakteristik im Detail zu untersuchen.

In einem Experiment am Experimentierspeicherring (ESR) bei der GSI konnte die praktische Durchführbarkeit dieser Methode überprüft und bestätigt werden. Hierbei wurden durch K-Schalenionisation von Li-ähnlichem Uran einfach angeregte Zustände in He-artigem Uran erzeugt. Dabei stellte sich heraus, dass die K-Schalenionisation ein äußerst zustandsselektiver Prozess ist, durch den ausschließlich die *s*-Unterzustände - $(1s2s)\ ^1S_0$ und $(1s2s)\ ^3S_1$ - erzeugt werden. Erklären lässt sich dieser Befund unter der Annahme, dass sich die Li-ähnlichen Ionen vor dem Stoß im Grundzustand $1s^22s_{1/2}$ befinden und in den Prozess der K-Schalenionisation nur $1s$-Elektronen involviert sind. Tatsächlich ergibt sich eine Erklärung für diese These unter Annahme der Störungstheorie und des "Independent-Particle" Modells. Die Berechnungen der stoßparameterabhängigen Wahrscheinlichkeiten auf der Basis der "Semiklassischen Näherung" zeigen in der Tat höchst unterschiedliche Stoßparameterabhängigkeiten für die beiden relevanten Ein-Elektronenprozesse der K-Schalenionisation und die Innerschaleanregung der L-Schale. Hieraus kann gefolgert werden: in einem atomaren Stoß schwerer Ionen mit leichten Targetatomen, bei dem ein K-Schalenelektron ionisiert wird, bleibt das L-Schalenelektron unbeeinflusst. Insbesondere konnte im Rahmen der vorliegenden Dissertation der obige Befund direkt zur präzisen Messung der Spektralverteilung des Zwei-Photonen-Zerfalls in He-artigen Ionen angewandt werden.

Bereits seit den Anfängen der Quantenmechanik hat dieser Prozess besondere Aufmerksamkeit auf sich gezogen. Maria Göppert-Mayer formulierte schon 1931 eine nicht-relativistische Theorie für den $2E1$ Zerfall in einem Wasserstoffatom; eine verbesserte Behandlung des $(1s2s)\ {}^1S_0 \rightarrow (1s^2)\ {}^1S_0$ Zwei-Photonen-Übergangs in Helium wurde von Breit und Teller gegeben. In diesem doppelten elektrischen Dipolübergang werden zwei korrelierte Photonen mit den Energien $\hbar\omega_1$ und $\hbar\omega_2$ simultan emittiert und teilen die vollständige Übergangsenergie $\hbar\omega$ untereinander auf: $\hbar\omega_1 + \hbar\omega_2 = \hbar\omega = E_i - E_f$. E_i und E_f beschreiben die Energien des Anfangs- bzw. Endzustands des $(1s2s)\ {}^1S_0 \rightarrow (1s^2)\ {}^1S_0$ Übergangs. Die Photonenenergien beschreiben ein kontinuierliches Spektrum, welches maximale Intensität bei der Hälfte der Übergangsenergie besitzt und zu den beiden Endpunkten des Spektrums hin auf Null abfällt. Während der Ein-Photonenzerfall lediglich vom Anfangs- und Endzustand des Übergangs abhängt, wird die Form des Zwei-Photonen-Kontinuums durch die Summation über alle Zwischenzustände (gebundene und kontinuierliche) des Atoms oder Ions bestimmt. Daher ist die spektrale Verteilung sehr empfindlich auf die gesamte atomare Struktur. Deswegen ist eine detaillierte Untersuchung der Zwei-Photonen-Verteilung entlang der isoelektronischen Sequenz heliumartiger Ionen äußerst wichtig für das Verständnis der Wechselwirkung zwischen Relativität und Elektron-Elektron-Korrelationen in mittleren und schweren hoch geladenen Ionen. In den vergangenen zwei Jahrzehnten sind viele theoretische und experimentelle Anstrengungen unternommen worden, die spektralen Eigenschaften der Zwei-Photonen Verteilung genau zu bestimmen. Sowohl nicht-relativistische als auch relativistische Rechnungen wurden durchgeführt und zeigen vor allem im "Full Width at Half Maximum (FWHM)" der Verteilung starke Unterschiede auf. Dies liegt an der relativistischen Kontraktion der Wellenfunktion in der Nähe des Kerns und an Effekten der Elektron-Elektron-Wechselwirkung.

In konventionellen Zwei-Photonen-Zerfalls Studien werden die angeregten Zustände in He-artigen Ionen durch Stöße mit leichten Festkörpertargets erzeugt und die emittierten Röntgenphotonen in Photon-Photon-Koinzidenzen mit zwei

Detektoren gemessen. Auch ist diese Methode oft mit zusätzlichen Koinzidenzen auf das He-artige Projektil nach dem Stoß ergänzt worden. Der Elektroneneinfang in das Projektil wurde verwendet, um den $(1s2s)\ ^1S_0$ Zustand zu bevölkern. Diese Koinzidenztechnik war bislang von entscheidender Bedeutung, da nur sie die Unterscheidung zwischen wahren $2E1$-Ereignissen und dem möglichen Röntgenuntergrund ermöglichte.

Im Gegensatz dazu kann die Zustandsselektivität der K-Schalenionisation ausgenutzt werden, um die Spektralverteilung des Zwei-Photonen Zerfalls mit nur einem Röntgendetektor zu messen. Hierbei erfolgt der Photonennachweis in Koinzidenz mit einem Teilchendetektor, der die einfach ionisierten Projektile mit einer Nachweiswahrscheinlichkeit von 100% registriert. Diese Nachweistechnik weist gegenüber der konventionellen Photon-Photon-Koinzidenztechnik mehrere entscheidende Vorteile auf, von denen hier die drei wichtigsten betont werden sollen. Erstens: Die Nachweiseffizienz ist gegenüber der konventionellen Methode um mindestens drei Größenordnungen erhöht, und die statistische Unsicherheit bestimmt nicht länger das Meßresultat. Zweitens: Die systematischen Unsicherheiten, die sich aus der Effizienzkorrektur für den Photonennachweis ergeben, sind ebenfalls wesentlich reduziert, da nur noch ein Detektor und nicht das Produkt der Effizienzen zweier Detektoren berücksichtig werden muss. Drittens: Ein besonderer Vorteil folgt aus der Tatsache, dass keine Bevölkerung des $(1s2p)\ ^3P_0$ Zustands erfolgt, und somit das Kontinuum der $2E1$-Spektralverteilung nicht durch den $E1M1$-Zerfall des $(1s2p)\ ^3P_0$ Zustands kontaminiert wird. Dieser tritt bei hohen Kernladungszahlen auf und kann nicht vom $2E1$-Zerfall des $(1s2s)\ ^1S_0$ Zustands experimentell unterschieden werden.

Eine erste Messung der Energieverteilung des Zwei-Photonen-Zerfalls des $(1s2s)\ ^1S_0$ Niveaus in He-artigem Zinn wurde mit der vorgestellten Methode durchgeführt. Hierbei wurden angeregte He-artige Ionen durch K-Schalenionisation von Li-artigen Projektilen erzeugt. Dazu wurden Li-artige Ionen in Stößen mit einem molekularen Stickstofftarget ionisiert und die hierauf emittierte Projektilröntgenstrahlung gemessen. Die dabei beobachtete intensive Emission der $2E1$-Photonen ermöglichte eine äußerst genau Studie des Zwei-Photonen-Kontinuums und somit der Struktur schwerer He-artiger Systeme.

Das Experiment wurde am Experimentierspeicherring (ESR) der Gesellschaft für Schwerionenforschung (GSI) in Darmstadt durchgeführt. Li-artiges Zinn wurde mit einer Energie von 300 MeV/u auf ein Stickstofftarget mit einer Dichte von 10^{12} Atomen/cm^3 geschossen. Die dabei erzeugten Photonen wurden mit einem planaren, hochreinen Germaniumdetektor unter einem Winkel von 35° nachgewiesen. Detektor und Hochvakuumwechselwirkungskammer sind durch ein 100 μm dickes Beryllium Fenster voneinander getrennt. Nach der Wechselwirkung wurde das ionisierte Projektil nach der nächsten Dipolkammer mit einem Vieldrahtzähler registriert, um später Teilchen-Photon-Koinzidenzen bilden zu können. Vor und nach dem Experiment wurden Energie- und Effizienzkalibrationen mit dem Detektor durchgeführt. Dazu wurden ^{57}Co, ^{133}Ba und ^{241}Am-Quellen verwendet. Die Röntgenphotonen wurden im Event-by-Event Modus ohne Hardware-Koinzidenz weggeschrieben. Jedoch wurde bei jedem Ereignis die Zeit- und Energiesignale aller eingesetzten Detektoren weggeschrieben. Ein Gesamtröntgenspektrum besteht daher zunächst aus allen Ereignissen, die durch Anregung, Ionisation oder Elektroneneinfang emittiert wurden. Über eine Koinzidenz mit dem ionisierten Projektil lässt sich jedoch das reine Ionisationsspektrum gewinnen und somit auch das $2E1$ Spektrum. Dieses besteht aus der breiten Verteilung des $2E1$ Grundzustandsübergangs des $(1s2s)\ ^1S_0$ Niveaus und der scharfen Linie des $(1s2s)\ ^3S_1 \rightarrow (1s^2)\ ^1S_0$ $M1$ Übergangs. Andere Übergänge sind aufgrund der hohen Selektivität des Ionisationsprozesses nicht vorhanden. Neben dem scharfen $M1$-Übergang, kann das $(1s2s)\ ^3S_1$ Niveau auch über einen $2E1$ Übergang zerfallen und somit das Spektrum des $(1s2s)\ ^1S_0$ Übergangs verunreinigen. Der $M1$ Übergang ist jedoch 10^4 mal wahrscheinlicher, weshalb der $2E1$ Beitrag vernachlässigt werden kann.

Da die Zwei-Photonen-Verteilung symmetrisch um $f = \hbar\omega_1/(\hbar\omega_1 + \hbar\omega_2) = 0.50$ ist, kann die Analyse der Z-Abhängigkeit auf eine Hälfte der Verteilung beschränkt werden. Im höherenergetischen Bereich der Verteilung ist die Detektoreffizienz besser bekannt und es liegen dort keine Verunreinigungen mit weiteren Übergängen vor. Daher wurde die "obere" Hälfte der spektralen Verteilung zur Datenauswertung verwendet. Lediglich die niederenergetischen Ausläufer des $M1$-Übergangs könnten das hochenergetische Ende der Verteilung beeinträchtigen, weshalb Energien oberhalb von $f = 0.92$ nicht berücksichtigt wurden.

Die "Response Function" des Germanium-Detektors wurde mit dem EGS4

Paket, inklusive der LSCAT Erweiterung, simuliert. Diverse Photon-Atom Wechselwirkungsprozesse im Germaniumkristall und die entsprechenden geometrischen Parameter wurden berücksichtigt. Das Ergebnis der Simulation wurde mit der energieabhängigen Detektorauflösung gefaltet, welche zuvor auf die Dopplerverbreiterung aufgrund des endlichen Detektoröffnungswinkels korrigiert wurde. Die Simulationen reproduzieren die gemessene Position und Intensität der Germanium K-escape peaks der $M1$-Linie äußerst gut.

Die gemessene spektrale Verteilung der Photonen wurde mit vollständig relativistischen Rechnungen verglichen. Diese Methode findet Anwendung, um über das vollständige Dirac-Spektrum summieren zu können. In diesen Rechnungen wird die interelektronische Wechselwirkung über ein effektives Abschirmpotential berücksichtigt. Um die $2E1$ Verteilungen von Ionen mit unterschiedlicher Kernladungszahl zu vergleichen, werden sie auf ihren Mittelpunkt normiert. Für das FWHM der Verteilung sagt die Theorie eine Reduktion um 14% von Nickel ($Z = 28$) bis Uran ($Z = 92$) voraus.

Das berechnete, simulierte Spektrum wurde über einen MINUIT-Minimierungscode an das experimentell gewonnene Spektrum angepasst. Dazu wurden theoretische Vorhersagen für unterschiedliche Kernladungszahlen verwendet und geschaut, welches Modell die beste Übereinstimmung liefert. Die Datenpunkte des Zinnmodells stimmen innerhalb von $\pm 3\sigma$ mit dem Durchschnittswert überein. Das Uranmodell dagegen weicht bis zu 10σ von den Experimentdaten ab. Dies liegt an relativistischen Effekten, welche die Breite des $2E1$ Spektrums von Uran gegenüber dem von Zinn deutlich verringern.

Zudem wurde die gemessene spektrale Verteilung des $(1s2s)\ ^1S_0$ $2E1$-Übergangs mit theoretischen Vorhersagen für verschiedene Kernladungszahlen Z verglichen. Die experimentellen Ergebnisse befinden sich in hervorragender Übereinstimmung mit den vollständig relativistischen Strukturrechnungen. Hier muss hervorgehoben werden, dass das experimentelle Zweiphotonen-Kontinuum He-artiger Ionen erstmals sensitiv auf die Kernladungszahl des untersuchten Ions ist.

Die in dieser Arbeit vorgestellte Methode kann auch verwendet werden, um einen anderen exotischen Übergang zu studieren: den Zwei-Elektron Ein-Photon (two-electron one-photon = TEOP) Übergang in Li-artigen Schwerionen, dessen theoretische Beschreibung eine Herausforderung für die aktuelle Strukturtheorie darstellt. Zu diesem Thema ist eine erste Strahlzeit am ESR durchgeführt worden. Gegenstand der Untersuchung waren hier die Zerfallsmodi des $1s2s^2$ Zustands. Erzeugt wurde dieser Zustand durch K-Schalenionisation der Be-artigen Projektile. Die bei diesem Prozess emittierte Röntgenstrahlung wurde mit Halbleiter-Detektoren unter verschiedenen Beobachtungswinkeln gemessen. Spektren, die in Koinzidenz mit dem Elektronenverlust der Projektile nachgewiesen werden konnten, zeigen eine einzelne Übergangslinie, die dem TEOP-Zerfall in das $1s^22p_{1/2}$ Niveau zugeordnet werden kann. Möglicherweise enthält diese Linie aber auch einen Beitrag des $M1$ Zerfalls in den $1s^22s$ Grundzustand. Durch Erweiterung dieser Studien um ein Elektronenspektrometer und ein hochauflösendes Mikrokalorimeter kann zusätzlich der Autoionisationskanal und zudem der mögliche M1-Beitrag gemessen werden. Hierdurch wären alle Zerfallsmodi des $1s2s^2$ Zustandes vollständig erfasst.

In der Zukunft werden sich Experimente der Winkelverteilung und Polarisation des Zwei-Photonen-Zerfalls schwerer Ionen widmen, da hier die Beiträge der höheren Multipolordnungen der Wechselwirkung zwischen Ion und Strahlungsfeld Asymmetrien in der Photon-Photon Emission hervorrufen.

Bibliography

[1] M. Steck, P. Beller, K. Beckert, B. Franzke, F. Nolden**NIMa 532**, 357-365, (2004).

[2] T. W. Hänsch, D. J. Wineland, C. E. Wieman, S. J. Smith, Eds, **AIP Conference Proceedings 23**, 63, (1995).

[3] M. Inguscio, F.S. Cataliotti, P. De Natale, G. Giusfredi, F. Martin, F. S. Pavone, D. J. Wineland, C. E. Wieman, S. J. Smith, Eds, **AIP Conference Proceedings 23**, 81, (1995).

[4] G. Soff, T. Beier, M. Greiner, H. Persson, G. Plunien, **Adv. Quant Chem. 20**, 125, (1998).

[5] S. Fritzsche, **Habilitationsschrift Universität Kassel**, (1996).

[6] J. A. Gaunt, **Proc. R. Soc. A122**, 513, (1929).

[7] G. W. F. Drake, **Can. J. Phys. 66**, 586, (1988).

[8] M. H. Chen, K. T. Cheng, W. R. Johnson, **Phys. Rev. A 47**, 3692, (1993).

[9] K. T. Cheng, M. H. Chen, W. R. Johnson, J. Sapierstein, **Phys. Rev. A 50**, 247, (1994).

[10] D. R. Plante, W. R. Johnson, and J. Sapierstein, **Phys. Rev. A 49**, 3519, (1994).

[11] P. Indelicato, **Phys. Rev. A 51**, 1132, (1995).

[12] H. Persson, S. Salomonson, P. Sunnergren, and I. Lindgren, **Phys. Rev. Lett. 76**, 204, (1996).

[13] V. A. Yerokhin and V. M. Shabaev, **Phys. Lett. A 210**, 437, (1996).

[14] I. Lindgren, H. Persson, S. Salomonson and L. Labzowski, **Phys. Rev. A 51**, 1167, (1995).

[15] R. Marrus and P. J. Mohr, **Adv. At. Mol. Phys. 14**, 181, (1978).

[16] P. Mokler and Th. Stöhlker, **Adv. At. Mol. Opt. Phys. 37**, 297, (1996).

[17] W. R. Johnson, D. R. Plante, J. Sapierstein, **Adv. At. Mol. Opt. Phys. 35**, 255, (1995).

[18] M. Göppert-Mayer, **Ann. Phys. (Leipzig) 9**, 273, (1931).

[19] M. Göppert-Mayer, **Naturwissenschaften 17**, 932, (1929).

[20] S.P. Goldman, G.W.F. Drake, **Phys. Rev. A 24**, 183, (1981).

[21] M. Lipeles, R. Novick, N. Tolk, **Phys. Rev. Lett. 15**, 690, (1965).

[22] Robert S. Van Dyck, Charles E. Johnson, Howard A. Shugart, **Phys. Rev. A 4**, 1327, (1971).

[23] M. H. Prior, H. A. Shugart, **Phys. Rev. Lett. 27**, 902, (1971).

[24] Richard Marrus, Robert W. Schmieder, **Phys. Rev. A 5**, 1160, (1972).

[25] R. W. Dunford, H. G. Berry, K. O. Groeneveld, M. Hass, E. Bakke, M. L. A. Raphaelian, A. E. Livingston, L. J. Curtis, **Phys. Rev. A 38**, 5423, (1988).

[26] R. W. Dunford, M. Hass, E. Bakke, H. G. Berry, C. J. Liu, M. L. A. Raphaelian, L. J. Curtis, **Phys. Rev. Lett. 62**, 2809, (1989).

[27] R. W. Dunford, H. G. Berry, S. Cheng, E. P. Kanter, C. Kurtz, B. J. Zabransky, A. E. Livingston, L. J. Curtis, **Phys. Rev. A 48**, 1929, (1993).

[28] R. W. Dunford, D. A. Church, C. J. Liu, H. G. Berry, M. L. A. Raphaelian, M. Hass, L. J. Curtis, **Phys. Rev. A 41**, 4109, (1990).

[29] R. Marrus, V. San Vicente, P. Charles, J. P. Briand, F. Bosch, D. Liesen, I. Varga, **Phys. Rev. Lett. 56**, 1683, (1986).

[30] R. Marrus, P. Charles, P. Indelicato, L. de Billy, Ch. Tazi, J.-P. Briand, A. Simionovici, D. D. Dietrich, F. Bosch, D. Liesen, **Phys. Rev. A 39**, 3725, (1989).

[31] A. Simionovici, B. B. Birkett, J. P. Briand, P. Charles, D. D. Dietrich, K. Finlayson, P. Indelicato, D. Liesen, R. Marrus, **Phys. Rev. A 48**, 1695, (1993).

[32] S. Toleikis, B. Manil, E. Berdermann, H. F. Beyer, F. Bosch, M. Czanta, R. W. Dunford, A. Gumberidze, P. Indelicato, C. Kozhuharov, D. Liesen, X. Ma, R. Marrus, P. H. Mokler, D. Schneider, A. Simionovici, Z. Stachura, T. Stohlker, A. Warczak, and Y. Zou, **Phys. Rev. A 69**, 022507, (2004).

[33] P. H. Mokler, S. Reusch, A. Warczak, Z. Stachura, T. Kambara, A. Müller, R. Schuch, M. Schulz, **Phys. Rev. Lett. 65**, 3108, (1990).

[34] Th. Stöhlker, Ch. Kozhuharov, A. E. Livingston, P. H. Mokler, J. Ulrich, **Z. Phys. D - Atoms, Molecules and Clusters 21**, S233-234, (1991).

[35] R. Ali, I. Ahmad, R. W. Dunford, D. S. Gemmell, M. Jung, E. P. Kanter, P. H. Mokler, H. G. Berry, A. E. Livingston, S. Cheng, L. J. Curtis, **Phys. Rev. A. 55**, 994, (1997).

[36] H. W. Schäffer, R. W. Dunford, E. P. Kanter, S. Cheng, L. J. Curtis, A. E. Livingston, P. H. Mokler, **Phys. Rev. A. 59**, 245, (1999).

[37] R. W. Dunford, E. P. Kanter, H.W. Schäffer, P.H. Mokler, H.G. Berry, A.E. Livingston, S. Cheng and L.J. Curtis, **Physica Scripta. T80**, 143, (1999).

[38] H. W. Schäffer, P. H. Mokler, R. W. Dunford, C. Kozhuharov, A. Kramer, A. E. Livingston, T. Ludziejewski, H. T. Prinz, P. Rymuza, L. Sarkadi, Z. Stachura, Th. Stöhlker, P. Swiat, A. Warczak, **Phys. Lett. A. 260**, 489, (1999).

[39] P. H . Mokler, R. W. Dunford, **Physica Scripta 69**, C1, (2004).

[40] J. H. Tung, X. M. Salamo, F. T. Chan, **Phys. Rev. A. 30**, 1175, (1984).

[41] A. Surzhykov, P. Koval, S. Fritzsche, **Phys. Rev. A. 71**, 022509, (2005).

[42] H. F. Beyer and V. P. Shevelko, *Introduction to the physics of highly charged ions*, **Series in Atomic and Molecular Physics**, (2003).

[43] F. A. Parpia, W. R. Johnson, **Phys. Rev. A. 26**, 1142, (1982).

[44] G. Breit and E. Teller, **Astrophys. J. 91**, 215, (1940).

[45] J. Shapiro and G. Breit, **Phys. Rev. 113**, 179, (1959).

[46] S. Klarsfeld, **Lett. Nuovo Cimento 1**, 682, (1969).

[47] V. Florescu, **Phys. Rev. A. 30**, 2441, (1984).

[48] V. Florescu, S. Pătrascu, O. Stoican **Phys. Rev. A. 36**, 2155, (1987).

[49] W. R. Johnson, **Phys. Rev. Lett. 29**, 1123, (1972).

[50] E.J. Kelsey, J. Macek, **J. Math. Phys. 17**, 1182, (1976).

[51] S. P. Goldman, **Phys. Rev. A. 40**, 1185, (1989).

[52] A. Dalgarno, **Mon. Not. R. Astron. Soc 131**, 311, (1966).

[53] G. A. Victor, **Proc. Phys. Soc. London 91**, 825, (1967).

[54] I. Freund, **Phys. Rev. A. 7**, 1849, (1973).

[55] P. A. M. Dirac, "The Principles of Quantum Mechanics", **Oxford U. P., London, Chapter 3.2**, (1958).

[56] J. Eichler, **Phys. Rev. A. 9**, 1762, (1974).

[57] Y.-J. Wu, J.-M. Li, **J. Phys. B. 21**, 1509, (1988).

[58] D.-S. Guo, **Phys. Rev. A. 36**, 4267, (1987).

[59] X. Mu, B. Crasemann, **Phys. Rev. A. 38**, 4585, (1988).

[60] G. E. Brown, R. E. Peierls, J. B. Woodward, **Proc. R. Soc. London, Ser. A227**, 51, (1954).

[61] G. W. F. Drake, **Phys. Rev. A 34**, 2871, (1986).

[62] A. Derevianko, W. R. Johnson, **Phys. Rev. A 56**, 1288, (1997).

[63] A. Volotka, **Private communication**.

[64] R. C. Elton, L. J. Palumbo and H. R. Griem, **Phys. Rev. Lett. 20**, 783, (1968).

[65] Robert W. Schmieder and Richard Marrus, **Phys. Rev. Lett. 25**, 1692 - 1695, (1970).

[66] R.W. Dunford, H.G. Berry, D.A. Church, M. Hass, C.J. Liu, M.L.A. Raphaelian, L.J. Curtis, A.E. Livingston, **Phys. Rev. A 48**, 2729, (1993).

[67] S. Cheng, H. G. Berry, R. W. Dunford, D. S. Gemmell, E. P. Kanter, B. J. Zabransky, A. E. Livingston, L. J. Curtis, J. Bailey and J. A. Nolen, Jr., **Phys. Rev. A 47**, 903 - 910, (1993).

[68] R.W. Dunford, H.G. Berry, S. Cheng, E.P. Kanter, C. Kurtz, B.J. Zabransky, A.E. Livingston, L.J. Curtis, **Phys. Rev. A 48**, 1929, (1993).

[69] Th. Stöhlker, Ch. Kozhuharov, A. E. Livingston, P. H. Mokler, J. Ullrich and B. Fricke, **Z. Phys. D - Atoms, Molecules and Clusters 21**, S233-234, (1991).

[70] P.H. Mokler, **NATO ASI Series B 296**, 259, (1992).

[71] H.W. Schäffer, R.W. Dunford, C. Kozhuharov, A. Krämer, T. Ludziejewski, P.H. Mokler, H.-T. Prinza, P. Rymuzac, L. Sarkadi, T. Stöhlker, P. Swiat, and A. Warczak, **Hyperfine Interactions 114**, 49-53, (1998).

[72] H.W. Schäffer, P.H. Mokler, R.W. Dunford, C. Kozhuharov, A. Krämer, T. Ludziejewski, H.-Th. Prinz, P. Rymuza, L. Sarkadi, Th. Stöhlker, P. Swiat, A. Warczak, **Nucl. Instr. Meth. B 146**, 63-66, (1998).

[73] H.W. Schäffer, P.H. Mokler, R.W. Dunford, C. Kozhuharov, A. Krämer, T. Ludziejewski, H.-Th. Prinz, P. Rymuza, L. Sarkadi, Th. Stöhlker, P. Swiat, A. Warczak, **Physica Scripta T80**, 469-471, (1999).

[74] Y. Bannett and I. Freund , **Phys. Rev. Lett. 49**, 539 - 542, (1982).

[75] K. Ilakovac, J. Tudorić-Ghemo, S. Kaučić, **Phys. Rev. A 44**, 7392, (1991).

[76] K. Ilakovac, V. Horvat, Z. Krečak, G. Jerbić-Zorc, N. Ilakovac, T. Bokulić, **Phys. Rev. A 46**, 132, (1992).

[77] J. Schirmer, D. Habs, R. Kroth, N. Kwong, D. Schwalm, M. Zirnbauer, C. Broude, **Phys. Rev. Lett. 53**, 1897, (1984).

[78] J. Kramp, D. Habs, R. Kroth, M. Music, J. Schirmer, D. Schwalm, C. Broude, **Nucl. Phys. A 474**, 412, (1987).

[79] S. Klarsfeld, **Phys. Lett. 30A**, 382, (1969).

[80] R. Novick, *Physics of One and Two-Electron Atoms*, ed. F. Bopp and H. Kleinpoppen, North Holland, Amsterdam, 296, (1969).

[81] R. Ali, I. Ahmad, H.G. Berry, R.W. Dunford, D.S. Gemmell, E.P. Kanter, P.H. Mokler, A.E. Livingston, S. Cheng, L.J. Curtis, **Nucl. Instr. Meth. B 98**, 69, (1995).

[82] Y.B. Bannett, I. Freund, **Phys. Rev.A 30**, 299, (1984).

[83] K. Ilakovac, J. Tudoriæ-Ghemo, B. Bu.iæ, V. Horvat, **Phys. Rev. Lett. 56**, 2469, (1986).

[84] J. Eichler, W. E. Meyerhof, *Reletivistic Atomic Collisions* (Academic Press, San Diego, 1995).

[85] R. Anholt, **Phys. Rev. A. 19**, 1004, (1979).

[86] R. Anholt and U. Becker, **Phys. Rev. A. 36**, 4628, (1987).

[87] G. Basbas, W. Brant and R. Laubert, **Phys. Rev. A. 7**, 983, (1978).

[88] Th. Stöhlker, D. C. Ionescu, P. Rymuza, T. Ludziejewski, P. H. Mokler, C. Scheidenberger, F. Bosch, B. Franzke, H. Geissel, O. Klepper, C. Kozhuharov, R. Moshammer, F. Nickel, H. Reich, Z. Stachura, A. Warczak, **Nucl. Instr. Meth. B 124**, 160, (1997).

[89] C. Scheidenberger, Th. Stöhlker, W. E. Meyerhof, H. Geissel, P. H. Mokler, B. Blank, **Nucl. Instr. Meth. B 142**, 441-462, (1998).

[90] H. Poth, **Phys. Rep.196**, 135, (1990).

[91] F. Bosch, *The Physics of Electronic and Atomic Collisions*, AIP Conference Proc. 295, eds.: T. Andersen, B. Fastrup, F. Folkmann, H. Knudsen, N. Andersen, New York 1993, p. 3.

[92] M. Steck, **Nucl. Phys. A 626**, 473c, (1997).

[93] M. Steck, K. Beckert, H. Eickhoff, B.Franzke, O. Klepper, R. Moshammer, F. Nolden, P. Spädtke, and T. Winkler, *Proc. 4th Europ. Part. Accel. Conf. London, 1994,* eds. V. Suller and Ch. Petit-Jean-Genaz (World Scientific, Singapore, 1994) p. 1197.

[94] K. Blasche and B. Franzke, *"Status report on SIS-ESR, Proc.* 6^{th} *Europ. Part. Acc. Conf. (EPAC), London"*, World Scientific, Singapore, 133, (1994).

[95] F. Bosch, B. Schlitt, **Phys. Bl.53**, 27, (1997).

[96] B.Franzke, Information about ESR Paramteres, GSI-ESR/TN-86-01, 1986 (Internal Report).

[97] B. Franzke, Nucl. Instr. Meth. B24/25 18 87.

[98] U. Schaaf, *"Schottky-Diagnose und BTF-Messungen an gekuühlten Strahlen im Schwerionen-Speicherring ESR"*, Dissertation Universität Frankfurt, GSI 91-22, Darmstadt, 1991.

[99] O. Klepper and C. Kozhuharov, **Nucl. Instr. in Physics Research B 204**, 553-556, (2003).

[100] H. Reich, W. Bourgeois, B. Franzke, A. Kritzer and V. Varentsov, **Nuclear Physics A 626**, 417c, (1997).

[101] A. Krämer,*"PhD Universität Frankfurt"*, (2000).

[102] Th. Stöhlker, T. Ludziejewski, F. Bosch, R. W. Dunford, C. Kozhuharov, P. H. Mokler, H. F. Beyer, O. Brinzanescu, B. Franzke, J. Eichler, A. Griegal, S. Hagmann, A. Ichihara, A. Krämer, J. Lekki, D. Liesen, F. Nolden, H. Reich, P. Rymuza, Z. Stachura, M. Steck, P. Swiat, A. Warczak, **Phys. Rev. Lett. 82**, 3232, (1999).

[103] Th. Stöhlker, O. Brinzanescu, A. Krämer, T. Ludziejewski, X. Ma, A. Warczak, *X-Ray and Inner Shell Processes; 18th International Conference*, edited by D.S. Gemmel, E.P. Kanter, L. Young, AIP Conference Proc. 506, (Chicago, Illinois, 1999), p. 389, (2000).

[104] J. Rzadkiewicz, Th, Stöhlker, D. Banas, H. F. Beyer, F. Bosch, C. Brandau, C. Z. Dong, S. Fritzsche, A. Gojska, A. Gumberidze, S. Hagmann, D. C. Ionescu, C. Kozhuharov, T. Nandi, R. Reuschl, D. Sierpowski, U. Spillmann, A. Surzhykov, S. Tashenov, M. Trassinelli, S. Trotsenko, **Phys. Rev. A 74**, 012511, (2006).

[105] D. C. Ionescu, Th. Stöhlker, **Phys. Rev. A 67**, 022705, (2003).

[106] A. Kramer, A. Kritzer, H. Reich, Th. Stöhlker, **NIM B 174**, 205, (2001).

[107] J. A. Bearden, **Rev. Mod. Phys. 39**, 78, (1967).

[108] E. Browne, J. M. Dairiki, and R. E. Doebler, *Table of Isotopes*, John Wiley and Sons, INC, New York, 1450, (1978).

[109] S. I. Salem, S. L. Panossian, and R. A. Krause, **Atomic Data and Nuclear Data Tables 14**, 91, (1974).

[110] William R. Leo, *Techniques for Nuclear and Particle Physics Experiments*, Second Revised Edition, 228, (1994).

[111] S. Trotsenko, A. Kumar, D. Banas, H. Beyer, H. Bräuning, A. Bräuning-Demian, A. Gumberidze, S. Hagmann, S. Hess, P. Jagodzinski, et al., **GSI Scientific Report** (GSI Report 2007-1) Atomic Physics 04, P. 246, (2006).

[112] J. Bang and J. Hansteen, **K. Dan. Vidensk. Selsk. Mat. Fys. Medd. 31**, 13, (1959).

[113] D. Trautmann and F. Rosel, **Nucl. Instrum. Methods 169**, 259, (1980).

[114] W. R. Johnson and G. Soff, **At. Data Nucl. Data Tables 33**, 405, (1985).

[115] J. Eichler and W. Meyerhof, *Relativistic Atomic Collisions*,(Academic Press, San Diego), (1995).

[116] F. A. Parpia, C. F. Fisher and I. P. Grant, **Comput. Phys. Commun. 94**, 249, (1996).

[117] T. Åberg, **Phys. Rev. 156**, 35, (1967).

[118] A. Kupliauskiene, **J. Phys. B: At. Mol. Pot. Phys. 31**, 2885, (1998).

[119] A. N. Artemyev, V. M. Shabaev, V. A. Yerokhin, G. Plunien and G. Soff, **Phys. Rev. A 71**, 062104, (2005).

[120] C. D. Lin, W. R. Johnson, and A. Dalgarno **Phys. Rev. A 15**, 154, (1977).

[121] C. M$\oslash$ller, *"The Theory of Relativity"*, Oxford University Press, (1952).

[122] W. R. Nelson, H. Hirayama, and D. W. O. Rogers, *The EGS4 code system*, Stanford Linear Accelerator Center report SLAC-265 (1985).

[123] H. Hirayama and Y. Namito, **KEK Internal 2000-3**, (2000).

[124] Y. Namito and H. Hirayama, *LSCAT: Low-energy Photon-scattering Expansion for the EGS4 Code* (Inclusion of Electron Impact Ionization) KEK Internal 2000-4 (2000).

[125] V. M. Shabaev, I. I. Tupitsyn, V. A. Yerokhin, G. Plunien and G. Soff, **Phys. Rev. Lett. 93**, 130405, (2004).

[126] F. James and M. Roos, Computer Physics Communications 10, 343, (1975).

[127] R. Anholt, Ch. Stoller, J. D. Molitoris, D. W. Spooner, E. Morenzoni, S. A. Andriamonje, and W. E. Meyerhof, **Phys. Rev. A 33**, 2270, (1986).

[128] T. Ludziejewski, Th. Stöhlker, S. Keller, H. Beyer, F. Bosch, O. Brinzanescu, R. W. Dunford, B. Franzke, Ch. Kozhuharov, D. Liesen, A. E. Livingston, G. Menzel, J. Meier, P. H. Mokler, H. Reich, P. Rymuza, Z. Stachura, M. Steck, L. Stenner, P. Swiat and A. Warczak, **J. Phys. B: At. Mol. Opt. Phys. 31**, 2601-2609, (1998).

[129] *An International Accelerator Facility for Beams of Ions and Antiprotons*, Conceptual Design Report, GSI, November 2001.

[130] V. Florescu, **Phys. Rec. A 30**, 2441, (1984).

[131] Tong et al, **Phys. Rev. A 42**, 1442, (1990).

[132] W. Perrie, A. J. Duncan, H. J. Beyer, and H. Kleinpoppen, **Phys. Rev. Lett. 54**, 1790, (1985).

[133] H. Kleinpoppen, A. J. Duncan, H. J. Beyer, and Z. A. Sheikh, **Phys. Scr. T72**, 7, (1997).

[134] A. Surzhykov, Private Communication.

[135] T. Radtke, A. Surzhykov and S. Fritzsche, **Phys. Rev. A 77**, 022507, (2008).

[136] C. K. Au, **Phys. Rev. A 14**, 531, (1976).

[137] F. B. Rosmej et al. **Phys. Rev. A 63**, 032716, (2001).

[138] Y. Zou et al.,**Phys. Rev. A 67**, 042703, (2003).

[139] P. Beiersdorfer et al., **Phys. Rev. Lett. 95**, 233003, (2005).

[140] J. P. Marques et al., **Phys. Rev. A 47**, 929, (1993).

[141] C. Z. Dong et al., **J. Phys. B: At. Mol. Opt. Phys. 39**, 3121, (2006).

[142] D. Banas et al., **NIMB 235**, p.326-330, (2005).

[143] Th. Stöhlker et al., **X-RAY AND INNER-SHELL PROCESSES: 18th International Conference AIP 506**, 389, (2000).

[144] M. Nofal, S. Hagmann, Th. Stöhlker, D. H. Jakubassa-Amundsen, Ch. Kozhuharov, X. Wang, A. Gumberidze, U. Spillmann, R. Reuschl, S. Hess, S. Trotsenko, D. Banas, F. Bosch, D. Liesen, R. Moshammer, J. Ullrich, R. Dörner, M. Steck, F. Nolden, P. Beller, K. Beckert and B. Franczak, **J. Phys.: Conf. Ser. 58**, 307-310, (2007).

[145] M. Nofal, S. Hagmann, Th. Stöhlker, D. H. Jakubassa-Amundsen, Ch. Kozhuharov, X. Wang, A. Gumberidze, U. Spillmann, R. Reuschl, S. Hess, S. Trotsenko, D. Banas, F. Bosch, D. Liesen, R. Moshammer, J. Ullrich, R. Dörner, M. Steck, F. Nolden, P. Beller, H. Rothard, K. Beckert and B. Franczak, **Phys. Rev. Lett. 99**, 163201, (2007).

Acknowledgements

First and foremost, to my supervisor, Prof. Dr. Thomas Stöhlker, for his greatest contribution to this work and for the skilful guidance, continued encouragement and support during this project.

I am very grateful to Prof. Dr. Heinz-Jürgen Kluge and to Prof. Dr. Reinhard Dörner for my acceptance in the Atomic Physics group of GSI and in University of Frankfurt, and thus providing me the unique opportunity to do the PhD work.

My gratitude to Dr. Alexander Gumberidze, Dr. Christophor Kozhuharov, and Dr. Stanislav Tachenov for their great contribution to my understanding of physics and world view.

I am very grateful to my colleagues Dr. Heinrich F. Beyer, Dr. Carsten Brandau, Dr. Harald Bräuning, Sabrina Geyer, Prof. Siegbert Hagmann, Mayk Hegewald, Sebastian Hess, Dr. Ajay Kumar, Prof. Dieter Liesen, Dr. Natalia Lineva, Renate Märtin, Natalya Miski-Oglu, Dr. Brian O'Rourke, Dr. Regina Reuschl, Shadi Salem, Dr. Uwe Spillmann, Dr. Martino Trassinelli, Günter Weber and Dr. Danyal Winters for friendly environment and interesting discussions.

I would like to acknowledge collaborators Dr. Darek Banaś, Dr. Stephan Fritzsche, Prof. Paul Indelicato, Dr. Jacek Rzadkiewicz, Dr. Z. Stachura, Dr. Andrey Surzhykov, Dr. Andrey Volotka and Prof. A. Warczak who have closely followed the work and assisted in this research. I have learned a lot collaborating with you, many thanks for very useful discussions and your interest in my work.

For their general assistance in performing the experiments and successful beamtimes thanks go to the accelerator guys and especially to the ESR team.

For truly happy time during the years of my PhD I'm grateful to all my friends, Dr. Aleksey Adonin, Dr. Khuyagbaatar Jadambaa, Dr. Anatoliy Byelikov, Dr. Oleksandr Chorniy, Dr. Alberto Cribeiro Santalla, Oleksiy Gorda, Dr. Vitaliy Gostishchev, Dr. Yaroslav Kalmykov, Dr. Svetlana Korostiy, Dr. Maxim Miski-Oglu, Dr. Oleksandr Patalakha, Aleksey Sokolov, Dr. Gleb Vorobjev.

My very special hearty thanks to Olga Lepyoshkina for her kind support and many happy moments we spent together.

I cannot fully express my gratitude to my parents for supporting me in everything, I dedicate this work to you.

Many thanks to everyone who has helped me in carrying out this work.

CURRICULUM VITAE

PERSONAL DATA

Name: Sergiy Trotsenko
Birthday: 1980-02-15
Birthplace: Bogodukhiv, Ukraine
Citizenship: Ukraine

EDUCATION

since 2004	Johann Wolfgang Goethe-Universität, Frankfurt am Main (Department of Physics)
1997 - 2003	Kharkiv National University (Department of Physics and Technology)
1987 - 1997	Bogodukhiv Secondary School with advanced learning of Physics and Mathematics

PROFESSIONAL EXPERIENCE

since 2004	Gesellschaft für Schwerionenforschung GmbH, Darmstadt (Ph.D.-research in Atomic Physics Department)
2003 - 2005	National Science Center "Kharkov Institute of Physics and Technology" (Engineer-Physicist, Nuclear Spectroscopy Research Laboratory)
2002 - 2003	National Science Center "Kharkov Institute of Physics and Technology" (laboratory assistant, Nuclear Spectroscopy Research Laboratory)
2001 - 2002	Kharkiv National University, Department of Physics and Technology (Practice Student within the Project "Modelling of Biophysical Processes")